

THE MECHANICAL PROPERTIES OF  
PRECIPITATION HARDENED NICKEL-ALUMINUM ALLOYS

THE MECHANICAL PROPERTIES OF PRECIPITATION HARDENED  
NICKEL-ALUMINUM ALLOYS

By

LEONARD ROY CORNWELL, B.Sc.

A Thesis

Submitted to the Faculty of Graduate Studies

in Partial Fulfilment of the Requirements

for the Degree

Doctor of Philosophy

McMaster University

July, 1969

DOCTOR OF PHILOSOPHY (1969)  
(Metallurgy)

McMASTER UNIVERSITY  
Hamilton, Ontario.

TITLE: The Mechanical Properties of Precipitation Hardened Nickel-Aluminum Alloys

AUTHOR: Leonard Roy Cornwell, B.Sc. (Birmingham University)

SUPERVISOR: Dr. G. R. Purdy

NUMBER OF PAGES: vii, 110

SCOPE AND CONTENTS:

The macroscopic mechanical behaviour of alloys is intimately related to their structure at the atomic level. The influence of small ( $<0.1\mu$ ) ordered coherent particles ( $\gamma'$ ) on the mechanical properties of Ni-Al alloys has been studied. The maximum strength of polycrystals occurs at 0.45 volume fraction  $\gamma'$  and grain boundary embrittlement occurs at higher volume fractions. It was shown that long range order in the particles affects strength by increasing the anti-phase boundary energy. In monocrystals the deformation behaviour is strongly influenced by the amount of particles present.

By growing very large particles of  $\gamma'$  ( $\sim 1.0\mu$ ) dislocation-particle interactions have been studied. Stacking faults have been observed in the particles whose bounding dislocation Burgers vectors were determined. By suitable heat treatment still larger  $\gamma'$  particles ( $\sim 10\mu$ ) were formed which had incoherent interfaces. The dislocation networks at the interfaces were analysed.

### ACKNOWLEDGMENTS

I wish to acknowledge the invaluable advice and encouragement of my supervisor Dr. Purdy in many discussions, not only concerning this thesis but in the field of physical metallurgy generally. Similar thanks are also due to Dr. Embury particularly for helping to throw light on the intricate and mysterious art of electron microscopy.

I would also like to acknowledge the generous help of Mr. H. Walker and Mr. R. Jarochowicz in overcoming the many technical problems which arose, and assistance in manipulating the various pieces of equipment.

Financial support for the research by the Defence Research Board of Canada and for the author in the form of an Ontario Graduate Fellowship is gratefully acknowledged.

My thanks to Mrs. Anita Miltimore for her precise typing of this thesis and Mr. M. van Oosten for his excellent line drawings.

Finally a word of appreciation to the members of Dr. Embury's group for cheerfully sharing their air-conditioned accommodation in the Department of Metallurgy.

## TABLE OF CONTENTS

	<u>Page</u>	
CHAPTER I	INTRODUCTION	1
CHAPTER II	REVIEW OF THE LITERATURE	5
	2.1 The Precipitation of Ni <sub>3</sub> Al from Solid Solution	5
	2.2 The Particle-Matrix Interface	15
	2.3 The Mechanical Properties of Alloys Containing Coherent Ordered Particles	19
	2.4 The Deformation of Single Crystals Containing Coherent Ordered Particles	30
	2.5 Kink Bands in Deformed Metals	32
	2.6 Stacking Faults in Ni <sub>3</sub> Al	34
CHAPTER III	EXPERIMENTAL TECHNIQUES	36
	3.1 Alloy Preparation	36
	3.2 Single Crystals	37
	3.3 Polycrystalline Compression Specimens	39
	3.4 Polycrystalline Tensile Specimens	40
	3.5 Electron Microscopy	41
	3.6 Long Range Order Measurements	42
	3.7 Splat Cooling	43
CHAPTER IV	RESULTS	44
	4.1 Mechanical Properties of Single Crystals	44

	<u>Page</u>
4.1.1 Crystals with small $\gamma'$ particles ( $<0.1\mu$ dia.)	44
4.1.2 Crystals with large particles ( $>1\mu$ )	52
4.2 The Mechanical Properties of Polycry- stalline Alloys	58
4.2.1 Compression tests	58
4.2.2 Tensile tests	61
4.3 Long Range Order	63
4.4 Splat Cooling	64
CHAPTER V THE FORMATION OF $\gamma'$ PARTICLES FROM SOLUTION	65
5.1 On Splat Cooling	65
5.2 On Water Quenching from Solid Solution	66
5.3 On Ageing	67
CHAPTER VI THE DEFORMATION OF SINGLE CRYSTALS	72
6.1 Crystals Containing Small $\gamma'$ Particles ( $<0.1\mu$ )	72
6.2 Crystals Containing Large $\gamma'$ Particles ( $\sim 1\mu$ )	83
CHAPTER VII SINGLE CRYSTALS WITH LARGE INCOHERENT $\gamma'$ PARTICLES	90
CHAPTER VIII THE DEFORMATION OF POLYCRYSTALS	101
8.1 Introduction	101
8.2 The Effect of Composition	102
8.3 The Effect of Ageing Time	107
CHAPTER IX CONCLUSIONS	110
BIBLIOGRAPHY	

## DEFINITIONS

Several terms (and their abbreviations) which are used extensively in this thesis, are defined below.

**Antiphase Boundary (APB):** A planar stacking mistake in an ordered crystal, which locally brings a high proportion of like atoms into nearest-neighbour positions.

**Critical Resolved Shear Stress (C.R.S.S.), ( $\tau$ ):**

$\tau = \frac{P}{A} \cos\theta \cos\phi$ , where P is the load at yield, A the cross-sectional area of the specimen,  $\theta$  is the angle between the specimen axis and the normal to the slip plane,  $\phi$  is the angle between the specimen axis and the slip direction.

**Schmid Factor:**  $\cos\theta \cos\phi$

**Long Range Order (L.R.O.):** This may occur in alloy crystals in systems with an energetic preference for unlike nearest-neighbour pairs. When this preference becomes dominant, the different kinds of atoms tend to associate with different sublattices over distances large compared with the unit cell dimensions.

**Long Range Order Parameter (S):**

$S = \frac{p-x}{1-x}$  where p is the probability that

a given atomic species A is on the correct sub-lattice and  $x$  is the atomic fraction of A in the alloy.

In this thesis, when the composition of the ordered crystals is unknown, the calculation of  $S$  will be based on ideal stoichiometric proportions.

#### Single Crystal or Monocrystal:

In alloys, a single crystal may be defined as one in which each atom or group of atoms in the structural motif has the same average orientation and composition. The single crystals referred to in this thesis were single as grown. After heat treatment, they contained dispersed precipitated particles; the continuous matrix phase was a single crystal as defined above.

## CHAPTER I

### INTRODUCTION

The term superalloys describes a category of alloys which have been developed for service at high temperatures and high stresses. Typical applications are, for instance, in the turbine blades of jet engines. These conditions require that such alloys have high strength, corrosion resistance and adequate ductility at the operating temperatures. Their compositions reflect these requirements in that different elements enhance different properties, thus leading to the complex compositions found in commercial materials. For example, chromium must be present to ensure corrosion resistance, carbon to impart grain boundary strength through the presence of carbides and aluminium for strengthening by the precipitation of a second phase.

The structure of nickel-based superalloys consists basically of small, coherent second phase particles distributed in a solid solution of the principal element. The relation between mechanical properties of these alloys and the second phase precipitate is a subject of current interest but most of the present work appears to be confined to commercial superalloys whose composition and ageing treatments are fixed. A detailed understanding of this relationship would seem to include a variation in the amount and size of second phase, an examination of the resultant bulk behaviour and correlation with the microstructure. This thesis is concerned primarily with this correlation.

In order to eliminate side effects due to the various additions

found in superalloys it was decided to use the binary alloy Ni-Al. This alloy is the prototype of the nickel-based superalloys in that the precipitation reaction is identical i.e. small, coherent particles of the  $\gamma'$  phase are precipitated on ageing. Coherency occurs when the lattice sites at the interface are common to both matrix and particle.

The influence of the amount of second phase was studied by varying the aluminum composition of polycrystalline alloys tested in both tension and compression, and observing the effects on yield strength and fracture properties. By measuring the size of the second-phase particles by electron microscopy an overall picture of the mechanical properties in terms of yield strength, work hardening, ductility and fracture characteristics as related to composition in terms of volume fraction, size and distribution of precipitate has been built up.

A detailed knowledge of the macroscopic deformation behaviour in relation to the microstructure was obtained by testing single crystals of different compositions in compression. Crystals with low volume fractions of second phase exhibited slip over the whole crystal whereas those with intermediate amounts showed kink bands and stress-strain curves with load drops. High volume fractions caused slip to be localised into a narrow band which broadened with deformation exhibiting a Luder's band type of behaviour. No kink bands were present but the stress-strain curve exhibited serrated flow. By considering a variety of experimental evidence including study of the surface slip lines, examination of back-reflection Laue X-ray diffraction pictures for asterism and thin film electron microscopy

the above behaviour was accounted for in terms of the microstructure.

Examination of the dislocation-particle interaction in these alloys is difficult because the particles are small  $<1000\text{\AA}$ . Accordingly large particles  $\sim 1\mu$  were obtained by suitable heat treatment which enabled this interaction to be seen in the electron microscope. For deformation by single slip it was shown that the particles could be sheared by groups of dislocations which travelled in pairs. It was also shown that particles could act as barriers to dislocations resulting in pile-ups which accounted for the high rate of work hardening found in these alloys. The coherent interface became incoherent after cold rolling showing dislocation networks at the interface. Furthermore, stacking faults were observed in the particles which were analysed to be of the intrinsic type bounded by partials of the type  $\frac{a}{3} \langle 112 \rangle$ . This is an important result because it confirms current theories which call for stacking faults without anti-phase boundaries characterised by the above partial dislocations.

For high volume fractions of second phase it was shown that the equilibrium precipitate has an incoherent interface containing a hexagonal network of dislocations. These dislocations were analysed to be of the type  $\frac{a}{2} \langle 110 \rangle$  and were shown to account for the mismatch between particle and matrix. By considering the elastic energy in both particle and matrix due to the interface a theoretical calculation showed that the difference between coherent and incoherent solubilities was small. A consequence of this treatment also showed that the composition of the second phase also changed slightly. This is an important result in view of the current

interest in the thermodynamics of coherent and incoherent second-phase particles.

## CHAPTER II

### REVIEW OF THE LITERATURE

#### 2.1 The Precipitation of Ni<sub>3</sub>Al from Solid Solution

The Ni-Al phase diagram, Fig. 1, shows that by ageing a supersaturated solid solution of nickel containing between 12 and 20<sup>a</sup>/o Al a second phase can be precipitated. This precipitate, termed  $\gamma'$ , has a composition close to Ni<sub>3</sub>Al and is a superlattice of the L1<sub>2</sub> type (Fig. 2), i.e. a f.c.c. structure with aluminum atoms at the corners and nickel atoms at the centres of the faces. The lattice parameter of  $\gamma'$  is slightly greater, about 0.57%<sup>(6)</sup>, than the matrix  $\gamma$ . This misfit introduces coherency strains at the precipitate-matrix interface which may contribute to the strength of the alloy<sup>(1)</sup>.

The first reported investigation of the morphology of  $\gamma'$  precipitates in Ni-Al alloys was by Westbrook<sup>(2)</sup>. He investigated the precipitates in several ternary alloys of the type Ni-Al-X. He obtained precipitation by rapid cooling in a water cooled cooling chamber from the solution temperature to obtain particles\*. However the cooling rate must have been relatively slow to produce such large particles (about 2.5 $\mu$  in size). The composition he was most concerned with was Ni-7.5<sup>a</sup>/o Ti-7.5<sup>a</sup>/o Al which would give a fairly high volume fraction of  $\gamma'$ .

In a plane section the particles were in groups of four and Westbrook attempted to show that, in fact, the particles were in groups of eight arranged on the corners of a cube. He described the clusters as

---

\* This term will be used to describe the  $\gamma'$  precipitate.

ogdoadically diced cubes. By using a wooden model composed of eight cubes of pine interleaved with mahogany he was able to account for the different structures seen in the micrographs by taking appropriate sections through the model. The presence of a thin layer of matrix between the cubes making up the clusters was explained by postulating that diffusion is difficult down these interfacial channels and by the presence of a slight disregistry between adjacent cubes. Since all cubes are coherent with the matrix the only kind of disregistry that is possible would be due to adjacent cubes being on different sub-lattices of the  $L1_2$  structure.

The origin of these clusters was discussed in terms of either subdivision of the master cube or concerted formation of eight individual cubes. Since he did not observe any 'unsplit' cubes, Westbrook favoured the individual formation of cubes. He then discussed the question as to whether the eight cubes formed on one common centre or on eight separate nuclei but concluded that the evidence was insufficient to give a conclusion. Westbrook argued that for those instances in which the ogdoadically diced cubes are obtained, a critical value of the ratio growth rate to nucleation rate is required. Below this critical value only single cubes are seen, this condition would seem to cover most of the ageing experiments on Ni-Al alloys in the literature. Above this critical value another set of cubes begin to grow from the corners of the existing cubes, a process which repeats itself to give a line of cubes in the  $\langle 111 \rangle$  directions.

Some of the cubes Westbrook observed showed concave faces and

extended corners which he explained following Papapetrou<sup>(3)</sup>. He argues that in the early stages of growth the cube corners acquire pointed extensions due to the increased activity at such sites compared to the faces. In later stages of growth, however, the sides of such extensions disappear since they are composed of high index faces the growth rate normal to which is much greater than that for those of low index.

The electron micrographs shown by Westbrook are from replicas and thus no conclusions can be drawn as to the state of the interface between particle and matrix i.e. whether it is coherent or incoherent. No more data on this type of precipitate morphology appears in the literature until the results considered later in this thesis.

All other published work on the Ni-Al system has concerned heat treatments which consist of a water quench from solid solution followed by ageing in the temperature range 550°C to 850°C. This treatment always produces small discrete particles of  $\gamma'$  which show deviations from a random distribution only after long ageing times when the particles begin to align along  $\langle 100 \rangle$  directions.

Williams<sup>(4)</sup> appears to have been the first to conduct a systematic study of the strengthening response of Ni-Al alloys with composition and ageing treatments. He used compositions between 7.9 at% and 15.5 at% Al and followed the hardness after ageing for different times at different temperatures. His conclusions regarding the precipitation process are based on X-ray diffraction data. The latter indicates that  $\text{Ni}_3\text{Al}$  precipitates in the form of coherent plates on the  $\{100\}$  planes, the coherency resulting in two tetragonal structures with common axes where the matrix has a  $c/a$  ratio

$<1$  and the  $\text{Ni}_3\text{Al}$  a  $c/a$  ratio  $>1$ . His conclusion that  $\gamma'$  precipitates as plates on  $\{100\}$  planes is at variance with recent thin film work<sup>(5,6)</sup> which shows that  $\gamma'$  initially precipitates as spheres which quickly become cubes at about  $50\text{\AA}$  in diameter. However, these studies also showed that on coarsening the cubes appear to become platelets but it is not clear if Williams results come from overaged specimens or not. His contention that the matrix develops a tetragonal structure at the interface with a  $c/a$  ratio  $<1$  is supported by a recent calculation by Ardell<sup>(7)</sup> who estimated this ratio to be 0.99. Ardell's work was supported by Oblak and Kear<sup>(8)</sup> who studied the fringe contrast at the  $\gamma'/\gamma$  interface and showed that Ardell's model interpreted this effect correctly.

Williams postulated that precipitation occurs by a two stage process. The first was believed to be a change of atomic configuration, presumably increasing short-range order, while the second is the actual precipitation of  $\text{Ni}_3\text{Al}$ . Manenc<sup>(9-11)</sup> also envisaged several steps. He described the first stage by the term "pre-precipitation" followed by precipitation of a coherent intermediate phase on  $\{100\}$  planes which was slightly tetragonal due to coherency strains and finally a visible stable precipitate possessing the equilibrium f.c.c. structure. Manenc discussed two interpretations of this so-called pre-precipitation effect. Firstly, following Guinier<sup>(12)</sup>, a random nucleation of plate-like zones on  $\{100\}$  planes each a few atoms thick and adjoined by impoverished matrix zones which exactly balanced the parameter variation in the central zone so that the average parameter matched the supersaturated matrix. Secondly, following Daniel and Lipson<sup>(13)</sup>, a general perturbation of lattice

regularity accompanied by a change of structure factor and a regular periodic atomic displacement in  $\langle 100 \rangle$  directions.

Bagaryatskii and Tyapkin<sup>(14,15)</sup> also made extensive studies of  $\gamma'$  precipitation by X-ray diffraction. However, they concluded that only a single intermediate stage exists and that the initial precipitation structure consists of isolated Guinier zones, while more zones nucleate on further ageing giving overlap and a structure resembling the Daniel and Lipson model.

Despite these extensive investigations it was not known whether there was any relationship between the modulated structures, i.e. alignment of  $\gamma'$  particles, seen after long ageing times, and the structures detected by X-ray diffraction which developed during the initial stages of precipitation. Both Ardell and Nicholson<sup>(5)</sup> and Phillips<sup>(6)</sup> did transmission electron microscopy work on aged Ni-Al alloys and concluded that there was no connection. Because of the lack of streaking on electron diffraction patterns, Phillips also concluded that the particles did not nucleate as platelets and only a single stage precipitation process occurred. Ardell and Nicholson also conclude that precipitation occurs by growth of nuclei, at least at the ageing temperatures and composition (13.5<sup>a</sup>/o Al cf Phillips 12.7<sup>a</sup>/o Al) they investigated. Both investigations pointed to the absence of spinodal decomposition as playing any part in the alignment process. Ardell and Nicholson paid particular attention to this point by cooling from the solution treatment temperature to the ageing temperature thus keeping above the spinode. This treatment still produced alignment thus supporting their conclusion. The best explanation of the side-bands

observed in the X-ray work seems to be the Guinier model of zones with the initial small particles of  $\gamma'$  being the zones. The size of the coherent particle controls the spacing of the side bands and thus their contraction as the particles grow during ageing can be understood.

It is worth noting that precipitation in these alloys is difficult to suppress by quenching. Phillips found no evidence of superlattice reflections in his as quenched alloys (12.7 at% Al) whereas Ardell and Nicholson found weak reflections in their as quenched alloys (13.5 at% Al). Manenc<sup>(9-11)</sup> and Bagaryatskii and Tyapkin<sup>(14,15)</sup> used Al compositions which would give volume fractions of  $\gamma'$  considerably larger than the above investigators and it is most unlikely that they could have suppressed the precipitation process by quenching. Ardell and Nicholson comment on the latter's observation of "side-bands" and point out that these are characteristic of modulated structures which can form very early in the ageing process of high volume fraction  $\gamma'$  alloys.

Ardell and Nicholson<sup>(5)</sup> discuss in some detail the alignment of  $\gamma'$  particles as platelets along  $\langle 100 \rangle$  after long ageing times. In an appendix, Eshelby discusses the elastic interaction between inclusions of this type. He was able to show that for particles with a smaller shear modulus than the matrix there was a positive interaction between particles proportional to  $1/R^6$  where  $R$  is the distance between two particles. On the basis of this calculation Ardell and Nicholson postulate that alignment is caused by the elastic interaction between particles. Thus for particles favourably aligned along a  $\langle 100 \rangle$  direction compared with an unfavourably positioned particle a gradient in chemical potential is established such that the former

particles grow at the expense of the latter. They further suggest that plate-like precipitates will tend to be oriented so that the plane of the plate is perpendicular to a direction of minimum Young's modulus i.e.  $\langle 100 \rangle$ , in this alloy.

This type of behaviour is a difficult problem and a satisfactory complete analysis is not yet available. For instance, what happens when the particle has a higher shear modulus than the matrix? The above analysis indicates a repulsion between particles so that alignment should not occur. However, there is some evidence in work by Weatherly<sup>(16)</sup> on the Cu-Fe system that alignment can still occur with 'hard' particles. However, the suggestion of alignment along  $\langle 100 \rangle$  directions due to a minimum in Young's modulus is reasonable since less energy will be required in straining the lattice in this direction to take up the misfit at the interface.

Ardell and Nicholson<sup>(5)</sup> also investigated the kinetics of the coarsening process of  $\gamma'$  particles (often called Ostwald ripening). They measured the rate of coarsening at three temperatures as a function of time up to the onset of alignment. They showed that particle size is a function of time governed by the relation  $\bar{a}/2 = kt^{1/3}$  where  $\bar{a}$  is the mean particle edge length,  $t$  is the ageing time at a given temperature and  $k$  is a constant given by Wagner<sup>(17)</sup> as

$$k = \left( \frac{8\gamma D C_0 V_m^2}{9 RT} \right)^{1/3}$$

where  $\gamma$  is the particle-matrix interfacial energy,  $D$  is the coefficient of diffusion of the solute in the matrix,  $C_0$  the solubility of the solute in equilibrium with a particle of infinite radius,  $V_m$  is the molar volume

of the precipitate and  $RT$  has its usual meaning. Their results showed that the behaviour is consistent with the theories of coarsening of Wagner<sup>(17)</sup> and Lifshitz and Slyozov<sup>(18)</sup>. They also used their data to estimate the activation energy  $Q$ , for diffusion by plotting  $\log k^3$  against  $1/T$  and obtained a value of 64.4 kcal/mole. This is close to Swalin and Martin's<sup>(19)</sup> figure of 64 kcal/mole for the activation energy of diffusion of Al in Ni. However, Ardell and Nicholson point out that they have ignored the temperature dependent term  $C_0/T$  but, in a later work<sup>(21)</sup> include this dependence and obtain the same result.

Ardell and Nicholson point out that the Lifshitz-Wagner theory is strictly speaking applicable to coarsening in fluid systems only although Oriani<sup>(20)</sup> has discussed how the theory can be modified to cover the case of solid systems. The conclusion was that the Ni-Al system acts like an ideal system in that the  $\gamma'$  particles behave as though they were randomly distributed throughout the matrix. In a later paper<sup>(21)</sup> Ardell and Nicholson discussed the coarsening behaviour further and pointed out that this system is the only one examined so far which agrees well with theory. Their conclusion is that the Lifshitz-Wagner equations are accurately obeyed in systems with small elastic strains in the matrix where the particles are spherical or regular polyhedra with crystallographically equivalent faces (as in Ni-Al). It further appears that the flux to particles is unaffected by the interparticle spacing at least until alignment occurs. Their experimental results show that the distribution of particle sizes is in good agreement with the theoretical distribution formulated by Wagner. This evidence lends support to their statement that Ni-Al behaves like an

ideal system in regard to the Ostwald ripening process.

One parameter of considerable importance and ignored so far concerns the rate at which the equilibrium volume fraction is obtained at a given ageing temperature. Ardell and Nicholson<sup>(5)</sup> are confident that this occurs very quickly and believe that nucleation had ceased before they made their observations. In their later work<sup>(21)</sup> Ardell and Nicholson calculated the foil thickness from an estimate of the volume fraction obtained from the phase diagram. They considered the results consistent with the sort of foil thickness necessary to allow sufficient transparency to show up weak superlattice reflections. They further pointed out that the supersaturated solid solution decomposes very rapidly even on quenching and that the good agreement between theory and experiment admits of no mode of particle growth other than coarsening.

Recent work by Ardell<sup>(22)</sup> does cast some doubt on the above conclusion. He estimated the concentration of Al in the matrix of a Ni-Al alloy as a function of ageing time by measuring the ferromagnetic Curie temperature. His results showed that the Al concentration is linearly related to  $t^{-1/3}$  which implies that Al is continuously being precipitated. This can result in either or both of two effects; an increase in volume fraction of  $\gamma'$  or an increase in the concentration of Al in  $\gamma'$ . For a constant volume fraction the composition of the  $\gamma'$  would have to increase at a rate governed by the lever rule, a situation which seems doubtful. However, until measurements are done on the effect of ageing time on volume fraction this question will not be conclusively resolved.

In the work just cited, Ardell makes an estimate of the concentration of Al in the matrix in equilibrium with a particle of infinite size by extrapolating to  $t^{-1/3} = 0$ . The values he obtains for two temperatures are some 10% greater than the results of Williams<sup>(4)</sup> and Taylor and Floyd<sup>(23)</sup>. He concludes that his results represent the solubility of coherent particles and by inference the other results represent the solubility of incoherent particles. It is true that incoherent solubilities are always less than coherent ones, as Cahn has shown<sup>(24)</sup> but this is hardly sufficient basis for assuming that Williams and Taylor and Floyd examined specimens which contained incoherent particles. Williams in particular aged his specimens in the same way as Ardell so it is difficult to see where the distinction comes from. However, in a more recent paper<sup>(25)</sup> Ardell has reversed his position and concludes that all the data in the literature represents coherent solubilities.

In this latest paper Rastogi and Ardell<sup>(25)</sup> have attempted to calculate the magnitude of the incoherent solubility over the temperature range 600 - 750°C and find that it is about 2 % Al less than the coherent solubility. They use the equations developed by Oriani<sup>(20)</sup> with suitable approximations and assuming that the composition of the  $\gamma'$  particles remains constant. In his derivation of the equations, Oriani assumed isotropic elasticity and that the ratios of the activity coefficients in the coherent condition and in the incoherent condition can be set equal to unity.

## 2.2 The Particle-Matrix Interface

In all investigations so far in the Ni-Al system where  $\gamma'$  is precipitated from solid solution coherency is maintained between the particle and matrix. We follow the definition of coherency as given by Kelly and Nicholson<sup>(1)</sup>.

"The interface between two crystals is fully coherent when the crystals are placed in contact such that the plane of atoms constituting the interface has an atomic arrangement disregarding chemical species of the atoms, which is common to both crystal structures."

It is generally believed that the misfit at this type of interface will produce sufficient strain energy to cause the interface to become incoherent by allowing dislocations to form there. That this does not occur is because there is another condition to be fulfilled, as Weatherly and Nicholson<sup>(26)</sup> pointed out, if dislocations are to be nucleated at the interface. This is that the theoretical shear stress must be exceeded. Weatherly<sup>(27)</sup> calculated that a certain critical misfit,  $\epsilon_{crit}^T$ , is needed before this condition is satisfied.  $\epsilon^T$  is the transformation strain given by  $\epsilon^T = \sum_{i=1}^3 \epsilon_{ij}^T$  for a spherical particle in pure dilatation. For spherical particles the value for  $\epsilon_{crit}^T$  turned out to be  $>0.04$ . If this is assumed to be valid for  $\gamma'$  cube particles then since  $\epsilon^T$  for  $\gamma'$  is  $\sim 0.017$  punching of dislocations from the interface cannot occur.

In their investigation into the loss of coherency at interfaces in several systems, Weatherly and Nicholson<sup>(26)</sup> mention other ways in which breakdown of coherency can occur. These are firstly, the climb of

dislocations from a source in the matrix, the driving force for climb being the elastic interaction between the strain fields of the particle and dislocation. Secondly, the nucleation of dislocation loops inside the particle; one way this could occur is by the collapse of a vacancy cluster into a dislocation loop.

None of these mechanisms has yet been found in Ni-Al alloys but Weatherly and Nicholson<sup>(27)</sup> have shown that incoherent particles occur in a similar system. This is in Nimonic 80A with a composition of Ni-20<sup>w/o</sup> Cr-2.32<sup>w/o</sup> Ti - 1.48<sup>w/o</sup> Al which on ageing precipitates spherical  $\gamma'$  particles with a misfit of 0.0028 (cf 0.0057 in Ni-Al alloys). In view of this smaller misfit it is at first sight a surprising result. However, there are two differences which may account for the result, firstly the Nimonic alloy has a larger volume fraction of  $\gamma'$  and secondly the ageing temperature was 930°C which is somewhat higher than the ageing temperatures usually used for Ni - Al alloys. Diffusion is considerably more rapid at 930°C than say 700°C so this may account for dislocation climb at the higher temperature. This argument implies that a Ni-Al alloy with sufficient Al to give precipitation at 930°C, should give  $\gamma'$  particles with incoherent interfaces.

Some particles such as  $\theta'$  in Cu-Al alloys can nucleate dislocations within the particles which are thought to form by the collapse of vacancy aggregates<sup>(26)</sup>. Loops have so far not been seen within  $\gamma'$  particles in Ni-Al alloys. This may be due to the lack of vacancies on the aluminum lattice sites as may occur in the above  $\theta'$ <sup>(28)</sup>. In other words the defect lattice on the nickel-rich side of  $\text{Ni}_3\text{Al}$  has nickel atoms on the sites of

missing aluminum atoms.

Brown et al<sup>(29)</sup> have derived two expressions which describe the conditions under which spherical particles can support a dislocation loop. The first expression describes the critical radius,  $r_c$ , below which a particle cannot support a dislocation loop at its interface when the force due to its line tension causing the loop to shrink is just balanced by a force due to the interaction with the stress field of the precipitate. The second expression defines a critical radius,  $r^*$ , below which an incoherent particle is metastable with respect to a coherent one and above which the opposite is true. Using values of  $1/3$  for Poisson's ratio and strain  $\epsilon = 2/3\delta$  where  $\delta$  is the misfit, for the case of  $\gamma'$  in Ni-Al alloys in the expressions gives  $r_{crit} = 120\text{\AA}$  and  $r^* = 233\text{\AA}$  or in terms of cube edge length  $240\text{\AA}$  and  $446\text{\AA}$  respectively. Hence alloys with particles below about  $450\text{\AA}$  can never become incoherent and many of the alloys so far studied have been in this condition. However, alloys in the overaged condition can have particles much larger than this which still remain coherent. Thus it seems that it is very difficult to punch out dislocations and Weatherly<sup>(27)</sup> has pointed out that the theoretical shear stress as determined by Kelly<sup>(30)</sup> can be exceeded in some systems without producing dislocations. Weatherly suggests this is due to the fact that Kelly considered nucleation of a shear loop at the surface of a crystal whereas we are considering the interior of a perfect crystal where it seems nucleation is much more difficult.

The type of interface we are discussing is characterised by a 'surface energy'. This is usually defined in terms of the increase in

free energy of a crystal per unit area of interface formed. It is made up of two components (Turnbull<sup>(31)</sup>), a structural and a chemical component. The structural component reflects disorder of atomic position at the boundary, while the chemical component results from a change in the number of neighbours of a given chemical identity, both relative to the interior of either crystal forming the boundary. For  $\gamma'$  particles in Ni-Al alloys the interface lies along {100} planes and it can be shown<sup>(21)</sup> that the introduction of a  $\gamma'/\text{Ni}$  interface along this plane does not produce a change in the nearest neighbour configurations. On this simple picture then  $\gamma_{(100)} = 0$  and interactions between second (and higher order) nearest neighbours account for their value of  $30 \text{ ergs/cm}^2$ . However, this is not strictly correct because the interface is between  $\gamma'$  and  $\gamma$ , i.e. a solid solution of Ni containing Al in which at  $700^\circ\text{C}$  1 atom in 8 is Al. Using the method of Ardell and Nicholson<sup>(21)</sup> for a solid solution instead of pure Ni shows that the number of Ni-Al bonds is reduced. However, it seems clear that the percentage change of nearest neighbour bonds is small and thus  $\gamma_{(100)}$  should be small.

Recent work by Ardell<sup>(22)</sup> has given a value of  $\gamma_{(100)}$  of  $14.3 \text{ ergs/cm}^2$ . This result depended on an experimental determination of  $C_e$ , the equilibrium concentration of Al in the matrix, as discussed above. This value is about half the previous value<sup>(21)</sup> and Ardell accounted for this by pointing out that previous calculations used the diffusion coefficient for Al in Ni in dilute solutions<sup>(21)</sup> whereas the effective diffusion coefficient in a 12<sup>a</sup>/o Al solid solution is about twice as high. An expression for calculating this value is given by Li and Oriani<sup>(32)</sup>.

### 2.3 The Mechanical Properties of Alloys Containing Coherent Ordered Particles

Precipitation from solid solution can result in a marked increase in yield strength over that of the solid solution. It is certain that this increase is due to the precipitates acting as obstacles to dislocation motion and it is usually only necessary to consider this interaction to account for this increase.

Mott and Nabarro<sup>(33-35)</sup>, and Orowan<sup>(36)</sup> were the first to advance dislocation theories for the yield stress of precipitation hardened alloys. Orowan showed that if the particle spacing is large enough the dislocations could bow between particles provided the particles could withstand the stress acting on them. In this case the yield stress is determined solely by the spacing of the particles. However, in alloys with coherent particles the spacing can be quite small,  $\sim 100\text{\AA}$ , and the particles will be cut by the dislocations before the stress is large enough to cause bowing to this radius.

There can be short- and long-range interactions between the dislocations and particles<sup>(1)</sup>. The former are those occurring as the dislocation passes through the precipitate, and the latter those forces on the dislocation due to the precipitate when the dislocation is at a distance from the precipitate of the same order as the precipitate spacing. Long-range forces could be due to coherency stresses but the problem arises as to how to average over the whole dislocation line the effect of individual particles. This difficulty was considered by Mott and Nabarro<sup>(33)</sup>.

Kelly and Nicholson<sup>(1)</sup> reviewed the theories then current so they need only be summarised here. In discussing Mott and Nabarro's theory

they concluded that it does not apply when dislocations cut particles but that the flow stress is determined by the forces on the dislocation due to internal stresses when a dislocation is close to an obstacle.

They listed the effects to be considered when a particle is sheared by dislocations as follows:

- (a) The interaction between the moving dislocation and the stress field around the precipitate at small distances from the precipitate.
- (b) The particle may be ordered so that anti-phase boundary is created when a dislocation shears the particle.
- (c) The lattice parameter of matrix and precipitate may be different so that work is done in producing a misfit dislocation at the interface.
- (d) If the slip planes in the matrix and precipitate are not parallel it may be necessary to form a jog in the moving dislocation as it passes through the precipitate.

Kelly and Nicholson then considered these interactions in more detail and make some quantitative estimates of the contributions. In particular, they considered the interaction of a dislocation with an ordered particle which produces an anti-phase boundary in the particle and an area of particle-matrix interface on the slip plane. The flow stress is then governed by the values of the surface energy terms and the area of particle on the slip plane i.e. volume fraction. They go on to calculate the critical radius of spherical particles at which dislocations change from cutting to bowing and estimate that particles of diameter greater than  $200\text{\AA}$  cannot be sheared. There is now a great deal of experimental evidence to show that this is not the case so their estimate is not realistic. This

is because they equated the interparticle spacing for bowing with distance between particle centres used in the cutting treatment which are different. Furthermore, dislocations move in pairs through particles thereby lowering the stress.

Experimental work on the Ni-Al system to obtain insight into the strengthening mechanisms has been done by Phillips<sup>(37)</sup>. By studying the variation of flow stress with change in temperature from 300<sup>o</sup>K to 77<sup>o</sup>K he was able to estimate the contributions to the flow stress from various hardening mechanisms. His results were that solid solution hardening contributed 36%, dislocation hardening 11%, coherency hardening 12-15%, and order hardening and modulus mis-match hardening 38-41%. This was for a 12.7<sup>a</sup> % Al alloy aged at 700<sup>o</sup>C. to peak hardness. Since this volume fraction was about 6% at 700<sup>o</sup>C the relative contributions will change as the volume fraction is increased such that the first two contributions will decrease and the second two increase. This in fact happened when Phillips aged the alloy at 600<sup>o</sup>C giving a volume fraction of about 0.16%  $\gamma'$ . The peak flow stress had increased by 10,000 psi for this 10% increase in volume fraction suggesting a linear relation.

Brown and Ham<sup>(38)</sup> have analysed Phillips' results in a different way. They first point out that the flow stress for the solid solution alloy is larger than is expected for substitutional strengthening and suggest that this indicates the presence of short-range order. They believe that the flow stress is made up from solid solution strengthening, equated with weak obstacles, and precipitation strengthening equated with strong obstacles. The weak obstacles are strongly temperature dependent and the strong obstacles weakly temperature dependent. They maintain that each type of

obstacle has a contribution to the temperature dependence of the flow stress and are able to calculate the total temperature dependence of the flow stress of the alloy. Their calculations seem to fit Phillips' experimental data quite well. For instance, at the peak strength of 52,000 psi they estimate the solid solution component of strength to be 25,000 psi and its temperature dependence factor 1.29, and the particle strengthening to be 27,000 psi with a temperature dependence factor of 0.98. The overall temperature dependent factor, corrected for the difference in shear modulus at 77<sup>0</sup>K and 303<sup>0</sup>K, turns out to be 1.07 as compared with Phillips experimental value of 1.06. They argue that the only real contribution to strengthening come from order strengthening and a friction stress in the  $\gamma'$  particles. They do not agree with Phillips' conclusion that order-strengthening is proportional to G which in turn is a function of temperature. Based on Davies and Stoloff's<sup>(39)</sup> results they show that order strengthening increases with increasing temperature in the range 77<sup>0</sup>k to 303<sup>0</sup>K. In considering the contribution of coherency strains to hardening they argue that appreciable hardening from this source would affect the component due to the particle to the temperature dependence of the flow stress. This would make their calculations in error but since they agree well with Phillips' results they conclude that the contribution from coherency hardening is small. By a similar argument Brown and Ham maintain that the same conclusion applies to misfit dislocations.

In their analysis of order strengthening Brown and Ham derive an equation for the flow stress by considering that dislocations travel in pairs such that the first dislocation bows sufficiently between particles to make the Friedel particle spacing condition applicable, while the

second dislocation is nearly straight. The Friedel condition occurs when a dislocation in bowing between two particles meets a third particle before it has escaped from the first two.<sup>(72)</sup> The Friedel spacing is then the distance between the third particle and the one closest to it. This expression is (see Appendix A for derivation).

$$\tau = \left(\frac{\gamma}{2b}\right) \left[ \left(\frac{4 \gamma r_s f}{\pi T}\right)^{1/2} - f \right] \quad (1)$$

When the Friedel condition does not apply

$$\tau = \left(\frac{\gamma}{2b}\right) \left[ \left(\frac{4 f}{\pi T}\right)^{1/2} - f \right] \quad (2)$$

where  $\gamma$  = APB energy of  $\gamma'$

$r_s$  = particle radius

$f$  = volume fraction of  $\gamma'$

$T$  = line tension of first dislocation

They analyse Phillips' results in terms of these equations by plotting the total flow stress minus the solid solution flow stress against particle size. The plot has a linear portion between  $r_s = 40\text{\AA}$  and  $r_s = 4\text{\AA}$  and from the slope and the above equation (1) they calculate  $\gamma$  to be  $138 \text{ ergs/cm}^2$ . When  $r_s = T/\gamma = 36\text{\AA}$  the Friedel condition does not apply and equation (2) should be used. This equation applies at peak ageing and gives a value of  $\gamma = 142 \text{ ergs/cm}^2$ . These values are close to others obtained previously (e.g. Copley and Kear<sup>(40)</sup>). However, Phillips'

results show only one measured value of  $r_s$  below  $40\text{\AA}$  and they have extrapolated the particle sizes below this as  $(\text{time})^{1/3}$ . This procedure is questionable since the times involved are a few minutes and the compositions of the particles could be a long way from equilibrium in which case the APB energy would be lower than that expected. Thus the good agreement of the  $\gamma$  values obtained with previous ones may well be fortuitous.

Brown and Ham go on to calculate the stress on the leading dislocation at the peak ageing stress in Phillips' results and compare it with their calculated value for the Orowan stress. The respective values are  $17 \times 10^8$  dynes/cm<sup>2</sup> and  $54 \times 10^8$  dynes/cm<sup>2</sup> from which they conclude that the Orowan process never occurs in the 12.7% Al alloy used by Phillips. They attribute the decline in flow stress after peak ageing to an increase in  $d_2/l_2$  where  $d_2$  is the length of the second dislocation in the particles and  $l_2$  is the interparticle spacing for this dislocation. What this means is that the second dislocation begins to bow closer to the first dislocation thus increasing the repulsive force and reducing the applied stress necessary for continued cutting of the particles. The mean interparticle spacing is given by  $L = 4r_s/3f$  which at peak ageing in Phillips' results gives  $L = 1540\text{\AA}$ . If the Orowan stress is taken to be  $\tau = Gb/L$  then with the above value for  $L$ ,  $\tau = 12.2 \times 10^8$  dynes/cm<sup>2</sup> which is considerably less than Brown and Ham's value. Even if the Friedel spacing is chosen this still gives a lower Orowan stress i.e.  $27 \times 10^8$  dynes/cm<sup>2</sup>, than Brown and Ham's value. Since there is a Gaussian distribution of particles it is not inconceivable that in low

volume fraction alloys such as the one Phillips' investigated, there are particles on the slip plane which are sufficiently separated to give the Orowan condition. Thus the Orowan mechanism cannot entirely be ruled out in explaining overaging, at least in alloys with low volume fractions of  $\gamma'$ .

Equation 2 quoted above gives a simple relation between flow stress due to particle cutting and the volume fraction. This only holds when the second dislocation is straight so that  $d^2/l_2 = f_v$ . This equation predicts a maximum strength over the range  $f = .3$  to  $.35$ .

Davies and Stoloff<sup>(39)</sup> investigated the flow stress of an aged Ni-14<sup>a</sup>/o Al alloy between 77<sup>o</sup>k and 973<sup>o</sup>k and found that it was independent of temperature between 173<sup>o</sup>k and 873<sup>o</sup>k. They concluded that this was due to a balance between the softening of the matrix and a hardening of the  $\gamma'$  particles in this temperature range. This only occurred when particles were cut by dislocations. In an overaged alloys the strength decreased with increasing temperature and in this alloy the Orowan mechanism was predominant. Their conclusions were based on electron micrographs which for the cutting mechanism showed planar arrays of dislocations while for the Orowan mechanism revealed tangles of dislocations resulting from bowing. They believe that strengthening by particles is due to the creation of particle-matrix interface on the slip plane as dislocations cut through the particles although they include a contribution from the resistance to dislocation motion in the particles. It appears now that this chemical term resulting from the new interface has a very small contribution. Brown and Ham<sup>(38)</sup> discount this contribution on the

grounds that the actual interfacial area created per dislocation is very small compared with the area of APB created in the particle. However, these results do show that bowing between dislocations can occur under certain conditions although they did not observe any loops round particles. This was probably because the right operating reflection conditions were not realised in the electron microscope.

That bowing can definitely occur in alloys with coherent ordered particles has been shown by Castagne<sup>(41)</sup>. He studied a Ni-base alloy containing Cr, Co, Mo, Ti and Al which on ageing gave spherical  $\gamma'$  particles with negligible coherency strains. Depending on the size of particles produced by ageing either pile-ups or bowing of dislocations was observed. For particles of diameter greater than  $500\text{\AA}$  single loops were observed round particles while for still larger particles  $\sim 1000\text{\AA}$ , double loops were seen.

Brown and Ham<sup>(38)</sup> analyse Castagne's results as they did with the results of Phillips and calculate the APB energy,  $\gamma$ , to be  $170 \text{ ergs/cm}^2$ . They submitted the results of Gleiter and Hornbogen<sup>(42)</sup> and Hornbogen and Mukherjee<sup>(43)</sup> on Ni-Cr-Al alloys to the same treatment and obtained  $\gamma = 97 \text{ ergs/cm}^2$ . They maintain that order strengthening is the main factor in increasing strength by ageing in all these alloys and that the experimental results are consistent with their theory. They conclude that alloying elements affect the APB energy  $\gamma$ , and hence the strength of the alloy. Thus those elements which increase  $\gamma$  lead to a strengthening of the alloy and vice versa.

Gleiter and Hornbogen<sup>(44)</sup> have also developed a theory to explain

the hardening in alloys by coherent particles. Their approach is similar to that of Brown and Ham in that they calculate the effect of a second dislocation interacting with a leading one and tending to push it through a particle. Their analysis is more rigorous in that they calculate the actual shape of the dislocations under various conditions of particle size and distribution. They also consider the effect of changing long range order in the particle with ageing time and also the increase in volume fraction with ageing time. Qualitatively the parameters which influence the flow stress are divided into those which increase and those which decrease the flow stress. The former predominate in the early stages of ageing and the latter become more predominant as ageing proceeds resulting in overageing. In the initial stages of ageing both the long range order of the particles and the volume fraction increase leading to an initial rapid rise in flow stress. They soon reach their equilibrium values and their contribution to strengthening remains constant. When a pair of dislocations passes through a spherical particle the leading dislocation has a longer segment in the particle than the second dislocation. It is maintained that the excess length of the leading dislocation is the main obstacle to motion through the particle and increases with the size of particle. Thus, there is an increasing contribution from this effect as the zones grow. However, as some particles grow others dissolve so it is difficult to see how this "effective" length of antiphase boundary increases after the equilibrium volume fraction has been reached. In passing it should be noted that for cube-shaped particles with a triangular cross-section on the slip plane this effective excess length

is independent of particle size. As the flow stress increases the second dislocation moves nearer the leading one thus increasing the force on the leading dislocation resulting in a lowering of the applied stress necessary for cutting. When the latter effect begins to predominate the alloy is in the overaged condition. Gleiter and Hornbogen argue that once overageing has begun the flow stress begins to decrease rapidly with ageing time. This in fact is doubtful as Phillips<sup>(6)</sup> results show. Furthermore, on the above model the dislocations must reach some equilibrium spacing and thus no further decrease in flow stress can be expected from this interaction.

Gleiter and Hornbogen<sup>(45)</sup> calculated the long range order in  $\gamma'$  particles in an ingenious way. They observed that an aged Ni-Cr-Al alloy containing spherical  $\gamma'$  particles also contained dislocation pile-ups. They noticed that the spacing of dislocation pairs in the pile-up increased with distance from the head of the pile-up. They reasoned that this is because the APB surface area in the particles was reduced through shearing by dislocations. An expression was derived relating the APB energy of the particles with the spacing of the dislocations in the pile-up. Measurements of these spacings on electron micrographs led to an estimate of the APB energy. These results showed that the (L.R.O.\*) order was lowest at the edges of the particle and increased towards the centre. The smaller the particle the greater the difference between the LRO at the edge and at the centre. The contrast of particles in electron micrographs which was weak at the edges of particles and particularly small ones, was cited as support for the above conclusion.

---

\* Long range order

In some very recent work Beardmore et al<sup>(46)</sup> have examined the temperature dependence of the flow stress of Ni-Cr-Al alloys. They measured the flow stress at temperatures up to 950°C as a function of volume fraction of  $\gamma'$ . The results showed that the flow stress at high temperatures increases with the amount of  $\gamma'$  in the alloy up to a maximum at 100%  $\gamma'$ . At room temperature this relationship is reversed with the peak strength occurring at 25%  $\gamma'$ . This latter result was unexpected and was shown to be due to hyperfine precipitation of  $\gamma'$  during cooling from the ageing temperature and is therefore absent at high temperatures. At high temperatures, the microstructures after deformation were characterised by a uniform tangle of dislocations stored in both  $\gamma'$  particles and the  $\gamma$  matrix in high volume fraction alloys. In low volume fraction alloys, the dislocations can bow between the particles leaving pinched off loops and the dislocations in this configuration are not paired. At low temperatures (below 500°C), deformation occurs in localised, discrete slip bands associated with large offsets. The slip bands become more diffuse as the volume fraction of  $\gamma'$  is increased or the temperature is raised. Dislocations move in pairs and are stored primarily in the matrix phase.

Fracture in precipitation hardened alloys often occurs in an intercrystalline manner with little ductility. The fracture passes along the grain boundaries with the grains themselves being little deformed. This phenomenon is often assumed to result from the presence of a precipitate free zone near the grain boundaries which can occur in alloys of this kind. The argument is that copious slip occurs in these denuded zones

and little within the grain interior. The material in these regions is thus rapidly worked to fracture with consequently little elongation.

In summary it can be said that the variation of flow stress with ageing time for a fixed volume fraction of precipitate has only been partly accounted for and, present theories do not adequately cover the effect of changing the volume fraction of precipitate on the flow stress.

#### 2.4 The Deformation of Single Crystals Containing Coherent Ordered Particles

Very few results have been published of the deformation of aged single crystals containing coherent ordered particles. This may be due to the difficulty of producing single crystals of two phase alloys. Most of the work has been done on aluminium alloys and was last reviewed by Kelly and Nicholson<sup>(1)</sup>. The alloys usually show a large increase in yield stress over the pure metal solvent but the work hardening is not greatly increased. Fairly coarse slip lines are usually seen on the crystal surfaces in contradistinction to the very fine slip lines characteristic of alloys containing hard, incoherent particles. This coarse slip is explained in terms of a decrease in resistance to dislocation motion by sheared particles once a slip plane is activated. Thus slip continues on an activated plane until local work hardening stops that particular source from operating. One particular important point emphasised by Jaoul<sup>(47)</sup> concerns an instability condition which may arise if the work hardening is not sufficiently high. Since the specimen area is decreasing this results in an increase in the resolved shear stress which may be more than necessary to sustain the strain so the load drops.

This condition occurs when  $\frac{d\tau}{da} < \frac{\tau}{2}$  where  $\frac{d\tau}{da}$  is the work hardening in terms of shear stress and shear strain, and  $\tau$  is the critical resolved shear stress. This is only applicable in a tensile test.

Pearcey and VerSnyder<sup>(48)</sup> have published results on single crystals of Mar-M200, a nickel-base superalloy. They find that the deformation characteristics are strongly dependent on orientation. Thus single crystals with single slip orientations exhibit maximum ductility and minimum work hardening whereas crystals with multiple slip orientations show the reverse.

Single crystals of precipitation hardened alloys often fracture in a peculiar way. This is characterised by slip on a narrow region of the specimen which lies approximately parallel to an active set of slip planes. Extensive shear occurs on these slip planes until the two halves of the crystal on either side of this region virtually slide apart. Price and Kelly<sup>(49)</sup> have shown that this can occur in a single crystal of Al-1.6% Cu aged to produce  $\theta''$  precipitate.

The work hardening characteristics of these alloys are similar to those for pure metals. This is a notable distinction to the behaviour of alloys with hard non-coherent particles which show much higher rates of work hardening than pure metals. These results are a consequence of the dislocation-particle interactions in both types of alloys. Coherent particles, other than raising the critical resolved shear stress, do not interfere with the movement of dislocations on slip planes since they are cut. On the other hand non-coherent particles, although initially easily by-passed by dislocations, quickly build up back stresses due to the

dislocation loops round them and raise the stress to keep dislocation sources operating or to operate new ones. The microstructures are characterised by high dislocation densities and tangles resulting from multiple slip.

## 2.5 Kink Bands in Deformed Metals

An unusual feature of deformation produced in certain metals is a structure which was termed 'kinking' by Orowan<sup>(50)</sup> and believed by him to be a mechanism of deformation different from slip and twinning. An analysis by Frank and Stroh<sup>(51)</sup> and results on zinc by Hess and Barrett<sup>(52)</sup> show that this is not the case and results from a particular dislocation arrangement during deformation. Kink bands have also been reported in aluminium by Cahn<sup>(53)</sup> and Chen and Mathewson<sup>(54)</sup>. The most recent reviews are by Maddin and Chen<sup>(55)</sup>, and Hirsch<sup>(56)</sup>.

Kink bands can be observed on the surface of a crystal as a small change in direction of the slip lines. This results in the appearance of a narrow band, at right angles to the slip lines, across which there is a small change in orientation. A Laue pattern of the kink band shows asterism suggesting that lattice bending is occurring through the band. It is believed that this bending is caused by an accumulation of edge dislocations on parallel slip planes in a localized region of the crystal. The axis of the rotation lies in the slip planes at right angles to the slip vector and is known as the 'roller axis'. In f.c.c. crystals this axis would be  $\langle 112 \rangle$ .

Although kink bands have frequently been observed a detailed understanding of the way in which they form is lacking. That they

are arrays of edge dislocations perpendicular to the slip direction seems certain and they would thus seem to be similar to dislocation tilt boundaries. The situation is further complicated by the use of the term deformation band to describe lattice rotation seen in crystals. Whether or not the two terms are synonymous or kinking is a particular kind of deformation band is not clear. According to Cottrell<sup>(57)</sup> kink bands show a sharper change in orientation because the dislocations are aligned vertically without any spreading of dislocations as in deformation bands. There is a further difference in that dislocations at kink band walls come from inside the kink band and not outside as with deformation bands. Frank and Stroh<sup>(51)</sup> have shown how a kink band can grow by considering a vertical 'wedge' of edge dislocations. The stress concentration at the tip of this wedge can be severe enough to create new dislocation pairs necessary for growth of the kink band provided the applied stress is high enough. The origin of the wedge is not known. It appears that both kinds of bands occur only in crystals oriented for single slip so that very few nuclei can form. In crystals exhibiting multiple slip so many nuclei form that none is able to collect enough dislocations to make a band.

Hatherly<sup>(58)</sup> has investigated the formation of kink bands in polycrystalline  $\alpha$ -brass during compression. He concludes that their formation depends on the presence of single systems of lamellar slip bands and emphasises the importance of grain interaction. The latter conclusion was deduced from the fact that kink bands had not been detected in single crystals of  $\alpha$ -brass. In this connection Kuhlman-Wilsdorf and

Wilsdorf<sup>(59)</sup> have suggested that this results from the slip lines being too far apart for the dislocations on corresponding planes to form the necessary kink array. Hatherly observed that kink bands appeared after deformation in the temperature range  $-183^{\circ}\text{C}$  to  $300^{\circ}\text{C}$ .

Observations of kink bands in two phase alloys do not appear to have been reported in the literature.

## 2.6 Stacking Faults in $\text{Ni}_3\text{Al}$

Stacking faults can occur in face-centred cubic metals when a unit dislocation dissociates to give two partial dislocations joined by a stacking fault. The stacking fault is characterised by an energy due to the change in stacking sequence of lattice planes. It can be visualised by the removal of one plane (an intrinsic fault), or the insertion of an extra plane (an extrinsic fault). If either of these processes occurred in a structure such as  $\text{Ni}_3\text{Al}$  a violation of nearest neighbour bonds would occur resulting in a fault of high energy. Since the fault energy determines the separation of the partial dislocation by balancing their mutual repulsion, a high fault energy would result in a very narrow separation of partials. Thus it would seem unlikely that this dissociation mechanism would occur in a  $\text{Ni}_3\text{Al}$  structure.

Recent observations, however, have shown that stacking faults can occur in  $\text{Ni}_3\text{Al}$ . Calvayrac and Fayard<sup>(60)</sup> observed stacking faults in  $\text{Ni}_3\text{Al}$  recrystallised after cold working. Kear et al<sup>(61)</sup> have also observed stacking faults in a nickel based alloy containing  $\gamma'$  after creep experiments. During examination of deformed  $\text{Ni}_3\text{Al}$ , Enami and Nenno<sup>(62)</sup>

observed stacking faults which they determined to have intrinsic character but did not determine the Burgers vectors of the partials bounding the fault.

To overcome the above difficulty in regard to the formation of stacking faults in structures of the  $\text{Ni}_3\text{Al}$  type, Carnahan et al<sup>(63)</sup> showed that it is possible to form stacking faults without violating nearest neighbour bonds. This can be done by removing a (111) plane of atoms and displacing the adjacent planes to fill the gap. Although, this results in an intrinsic stacking fault no nearest neighbour bonds are violated so that the fault has a low energy. To account for their formation in deformed  $\text{Ni}_3\text{Al}$  Kear<sup>(64)</sup> has suggested that two complex partials of Burgers vectors  $2\delta\text{B}$  and  $2\text{A}\delta$  could be separated by a stacking fault which has no anti-phase boundary. Evidence will be presented in this thesis to support this contention.

## CHAPTER III

### EXPERIMENTAL PROCEDURE

#### 3.1 Alloy Preparation

The alloys were made from spectrographically pure materials; analyses are given in Table I. Alloys were prepared by melting in an arc furnace under a gettered argon atmosphere and cast into a rectangular horizontal mold machined in the hearth. The ingots produced were approximately circular in cross-section of 0.4" diameter and 2.5" long. The button was turned over three times and remelted before casting into the mold to ensure homogeneity. The loss in weight was determined for each melt and found to be on average .1% of the initial weight. If all this loss was attributed to aluminum evaporation it would represent an insignificant change in the composition of the alloys. All compositions in this work are referred to in atomic %; these were converted to weight % for alloy preparation. The compositions of the alloys made are listed in Table 2. Also given are the volume fractions of  $\gamma'$  at 700°C calculated from the equilibrium weight fractions obtained from the phase diagram in Fig. 1. The volume fractions were calculated from the relation

$$\text{Wt \% } \gamma' = \frac{x \rho_{\gamma'}}{(100-x)\rho_S + x \rho_{\gamma'}}$$

where  $x = \text{vol. \% } \gamma'$ ,  $\rho_S = \text{density of matrix}$ ,  $\rho_{\gamma'} = \text{density of } \gamma'$ .

$\rho_S = 8.15$  using  $\text{a/o Al} = 12$  at 700°C

$\rho_{\gamma'} = 7.49$  using  $\text{a/o Al} = 23.2$  at 700°C

The density  $\rho$ , was found from  $\rho = \frac{n\bar{A}}{VN}$  where  $n$  = number of atoms in unit cell<sup>(4)</sup>,  $\bar{A}$  = mean atomic weight,  $V$  = volume of unit cell,  $N$  = Avogadro's number.

### 3.2 Single Crystals

Single crystals of several alloy compositions were grown by a modified Bridgeman technique in the apparatus shown in Figs. 3 and 4, similar to that used by McDonnell et al<sup>(65)</sup>. Ingots prepared by arc melting were ground to fit a pointed bottom, recrystallised alumina crucible,  $\frac{1}{2}$ " O.D.,  $\frac{3}{8}$ " I.D., 4" long with an angle of  $120^\circ$  at the bottom. The crucibles were cleaned by scrubbing with a detergent, rinsing in a solution of water-nitric acid-hydrofluoric acid and finally rinsing in distilled water followed by drying in an oven.

After the apparatus was assembled it was evacuated to  $10^{-4}$  mm and the induction unit switched on. The temperature in the region of the molten zone was monitored by a Pt-Rh thermocouple connected to a continuous chart recorder. The temperature was kept at  $1500^\circ\text{C}$  by varying the input to the induction coil. When this temperature was reached the apparatus was back-filled with argon to atmospheric pressure and the ingot slowly lowered through the coil at 1" per hour. This procedure was adopted so that gas bubbles would not be trapped at the base of the single crystal as might occur by melting initially in an inert atmosphere. An inert atmosphere had to be used during growth of the single crystal to avoid loss of aluminum by evaporation.

A graphite susceptor was used to give uniform heating to the ingot. The graphite was enclosed in a sleeve of "Fibrafrax" (manufactured by the

Union Carbide Corp.) an insulator which prevented large heat losses and protected the vycor tube.

There was always some reaction between the ingot and alumina tube so that weight losses could not be determined. A single crystal was not produced every time probably because of the reaction with the alumina tube producing new crystals. This was particularly so if the temperature rose too high when reaction became severe. In fact, Ni-Al alloys in the molten state are particularly reactive and attacked a crucible made of pyrolytic boron nitride which is considered to have a low reactivity. Temperature control sometimes became difficult because of the failure of the Pt-Rh thermocouple and this was eventually replaced by a Pt-5% Rh/Pt-20% Rh which has a higher melting point.

The single crystals produced were surface ground and electropolished then etched in a 10% Bromine-90% ethanol solution to test their integrity. Orientations were determined by the back-reflection Laue technique. The crystals were homogenised at 1300°C for 72 hours and quenched into iced water. The crystals were about 1.5" long and .350" diameter as grown and after spark-cutting and polishing were .3" diameter and .650" long.

Three different heat-treatments were used in studying the crystals, 1) aged at 700°C for 6 hours and water quenched 2) slow cooled from 1300°C to 700°C in 3 hours and water quenched 3) slow cooled in steps of 25°C from 1300°C to 700°C, equilibrating at each temperature for a time derived from the relation  $x = \sqrt{Dt}$  where  $x = 1\mu$ , and  $D_\gamma$  the diffusion coefficient of Al in Ni estimated from  $D_\gamma = 1.87 e^{-64000/RT}$  (the values for  $D_0$  and  $Q$  are as quoted by Swalin and Martin<sup>(19)</sup>) followed by water quenching.

This process took 3 weeks.

Flats were also polished on the sides of the crystal approximately 0.1" wide to aid in the examination of slip lines. Photomicrographs of slip lines were taken on these flat sides. Compression tests were done in an Instron at a strain rate of 0.015 per minute. Sections were obtained from the crystals by spark cutting with a 0.003" diameter molybdenum wire. An X-ray microbeam unit with a 100 $\mu$  diameter beam was used to detect asterism on these sections and also on the sides of crystals. The sections were then used for thin film microscopy.

### 3.3 Long Range Order Measurements

Since the degree of long range order of the  $\gamma'$  particles can exert an important influence on the mechanical properties an attempt was made to measure this parameter as a function of ageing time. This was done by measuring the intensities of the 100 and 200 lines by a diffractometer in a section cut close to a [100] orientation. In the absence of extinction the ratio of these intensities is a measure of the L.R.O. in the crystal. Cu radiation was used for this investigation.

A section was spark cut from a single crystal of composition 16<sup>a</sup>/o Al and mounted vertically in a Phillips diffractometer equipped with a spinner so that the specimen could be rotated about a horizontal axis. Since the section was not exactly at the [100] orientation the (100) planes were brought to the best reflecting position by rotating the section and 'rocking' the crystal about the angle  $\theta$ , with  $2\theta$  set, to obtain maximum intensity. The diffracted beam was directed onto a

focussing monochromator which was tuned to diffract the  $K_{\beta}$  radiation of the copper tube into the detector. A chart recorder was used to trace the peak profiles of the 100 and 200 reflections. The areas under the peaks were measured with a planimeter and the Lorentz-Polarisation factors applied to give values of the intensities.

The section was aged at times of  $\frac{1}{4}$ ,  $\frac{1}{2}$ , 1, 3, 6, 9, 24 hours at  $700^{\circ}\text{C}$  and the line intensities measured after each time. The section was electropolished before each measurement to remove any oxide film present.

#### 3.4 Polycrystalline Compression Samples

Ingots each 50 grms. in weight were produced in the form of bars as described above and ground to give compression specimens .5" long x .25" diameter. The 'out of squareness' of the specimens was checked on a shadowgraph and found to be less than 0.001". On the basis of a study of compression samples deliberately prepared 'out of square' by Alstruther and Christian<sup>(66)</sup> it is not thought there would be any error in load reading from this source. The specimens were sealed in a quartz tube under an argon atmosphere and annealed at  $1300^{\circ}\text{C}$  for 6 hours before quenching into ice cold water. The quenched specimens were then sealed in vycor tube under vacuo and aged at  $700^{\circ}\text{C}$  for various times followed by quenching into cold water. The temperatures were monitored by an alumel-chromel thermocouple and found to be within  $\pm 2^{\circ}\text{C}$  of the desired temperature.

A flat about  $0.01$ <sup>0.1</sup>" wide was ground along the length of the specimens to facilitate slip observations and grain size determinations.

Before testing the specimens were electropolished in a solution of 10% perchloric acid, 90% ethanol at 0°C. Compression tests were done on an Instron machine at a strain rate of .02 per minute. The specimens were compressed 1-2% and the slip lines on the flat surface examined by optical microscopy.

### 3.5 Polycrystalline Tensile Specimens

Ingots produced by argon arc melting were hot rolled to 0.025", the furnace temperature was 1300°C. The strips were cleaned by grit blasting and electropolishing followed by cold rolling to 0.012". At this thickness they were sealed in a quartz tube with an argon atmosphere and annealed at 1200°C for ½ hour and quenched into iced water. The final operation was cold rolling in a 4-high mill to 0.006" followed by an annealing treatment as above. The strips were then sealed in vycor tubes under vacuum and aged at 700°C for various times and quenched into water.

Alloys with aluminum contents greater than 17<sup>a</sup>/o could not be cold rolled due to brittleness, thus the range of compositions used for strip samples was 12 to 17<sup>a</sup>/o Al.

The aged strips were machined to flat tensile specimens with a 1.0" gauge length and 0.5" width and the grain size determined by lineal analysis. They were cleaned by electropolishing and tested on an Instron at a strain rate of 0.02 per minute. Specimens for particle size determination were electropolished in a solution of 59% ethanol, 35% ethylene glycol and 6% perchloric acid at 0°C and examined in the electron microscope. Dark

field electron micrographs were taken from superlattice reflections using the gun tilt method. The particle sizes were measured with a bench microscope equipped with an ocular readout. [100] and [110] directions were used in measuring particle sizes and compensated for where necessary when the foil plane was oriented away from (100).

### 3.6 Electron Microscopy

Thin films for transmission microscopy were prepared by the window technique using an electrolyte of 59% ethanol, 35% ethylene glycol and 6% perchloric acid at 0°C and 20 volts. Thin films from strip tensile specimens were obtained by cutting sections 0.5" long from the gauge length and thinning directly. Thin films from single crystals were obtained by spark-cutting sections approximately 0.02" thick and mechanically polishing to 0.005" before electropolishing.

Replicas were obtained by the direct carbon technique. The electropolished surface was etched in an electrolyte of 10% phosphoric acid, 90% water at 10°C and 20 volts for 1 second. Carbon was deposited on the surface by arcing carbon electrodes in a vacuum coating unit, and then stripped by dipping in distilled water after electropolishing in a 10% perchloric acid, 90% ethanol solution at 20 volts.

Most of the microscopy was done on a Siemens Elmiskop I; thin films being examined at 100 Kv, replicas at 80 Kv. For tilting experiments a double-tilting stage of the Valdre type was used. Some microscopy was done on a Phillips EM300 equipped with a single tilt stage capable of rotation. The double tilt stage was used for the determination of Burgers

vectors of dislocations in networks at particle interfaces and bounding partials of stacking faults.

### 3.7 Splat Cooling

To find out if  $\gamma'$  precipitation could be prevented by extremely high quenching rates, some high volume fraction alloys were splat cooled and examined by transmission electron microscopy. Two gram samples were levitation melted in an argon atmosphere and splat cooled by the drop hammer technique between copper blocks<sup>(73)</sup>.

## CHAPTER IV

### EXPERIMENTAL RESULTS

#### 4.1 The Mechanical Properties of Single Crystals

##### 4.1.1 Crystals with small $\gamma'$ particles (<0.1 $\mu$ dia.)

The mechanical properties of six single crystals with different compositions were investigated by compression tests. The compositions were 13, 14, 15, 16, 17 and 18 <sup>a</sup>/o Al whose volume fractions of  $\gamma'$  at 700<sup>o</sup>C are given in Table III. The orientations of the crystals were determined by the Laue back reflection technique and are plotted in the standard triangle shown in Fig. 5. The Schmid factors are given in Table III. The crystals were solution treated at 1300<sup>o</sup>C, quenched into iced water and then aged at 700<sup>o</sup>C for 6 hours followed by water quenching.

The results of the compression tests are given in Table III. Listed are values of the critical resolved shear stresses obtained from the 0.2% flow stress, work hardening rates obtained from shear stress-shear strain curves, and observations of the macroscopic slip behaviour. The latter descriptions indicate 3 different modes of deformation termed A, B and C, which can be related to the form of the load-extension curves obtained during the compression tests.

Deformation mode A is characterised by slip lines appearing over the whole crystal with a region of intense slip in one region giving a broad slip band. A photograph of the 14 <sup>a</sup>/o Al crystal in Fig. 6 shows the shape of the crystal after 4.5% compressive strain. The broad slip band has the same plane as the slip plane and the surface slip lines

extend round the crystal, except where they met the ends. A microphotograph of the slip lines in Fig. 7 shows they are widely spaced with large offsets except for the region of intense slip. The corresponding load-extension curve is smooth as shown for the 13<sup>a</sup>/o Al crystal in Fig. 8, and the corresponding shear stress-shear strain curve in Fig. 9 gives a work hardening rate of G/530. This value is consistent with stage I (i.e. single slip) work hardening for alloys of this kind and is supported by the slip lines being continuous round the circumference of the crystal.

This kind of slip behaviour should not result in any lattice distortion at the crystal surface in the region of intense slip as the slip lines just indicate points at which dislocations have 'run-out' of the crystal. That this is correct is shown by the absence of any asterism in back reflection Laue photographs taken in this region. Fig. 10(a) shows a Laue taken in the region of intense slip and Fig. 10(b) a Laue outside this region. There is obviously no asterism nor any change in orientation between the two areas.

The intense slip band region is believed to be due to constraint between the ends of the crystal and the compression plate so that stress concentrations are set up at the ends which are relieved by the slip band. The evidence for this lies in the fact that in both 13 and 14<sup>a</sup>/o Al crystals one part of the slip band appears very close to the point where the end of the crystal meets the compression plate. In fact, in the 14<sup>a</sup>/o Al crystal slip bands on different slip systems appear to start at

opposite ends of the crystal. For a smaller i.e. in length, 14<sup>a</sup>/o Al crystal (S1) this behaviour did not occur. Its initial length was 0.475" as compared to crystal S2 which had a length of 0.605", and after 4% compressive strain it was sectioned and the remaining length of 0.2" compressed a further 16%. It deformed uniformly to give the shape shown in Fig. 11.

The deformation structure was studied by sectioning the 14<sup>a</sup>/o Al crystal on the (111) slip plane after the 16% compression, and examining in the electron microscope. The structure is characterised by dislocation loops around  $\gamma'$  particles and paired dislocations as shown in the bright field micrograph, Fig. 12, and offsets in the  $\gamma'$  particles as shown in the dark field micrograph, Fig. 13. It is believed that the offsets in the  $\gamma'$  particles are caused by dislocations shearing the particles either by the collapse of loops or the passage of relatively straight dislocations. It appears that the particles cannot support more than one dislocation loop and tangles of dislocations round particles are not observed. This is consistent with the rate of work hardening observed since the presence of dislocation tangles would lead to much higher rates of work hardening as found in hard particle dispersion strengthened materials containing dislocation tangles.

A back-reflection Laue photograph of the (111) section shows evidence of asterism indication lattice bending (Fig. 14). This lattice bending could be explained by an excess of edge dislocations of one sign lying on the slip plane.

Considering now the deformation mode termed B we see it is

confined to two crystals of composition 15 and 16<sup>a</sup>/o Al. The characteristics are slip lines over the whole crystal but concentrated in one region which contains bands which appear to be perpendicular to the slip planes and will be termed kink bands. The general appearance of one of these crystals is shown in Fig. 15 and the slip line structure in the kink band region is shown in Fig. 16. The slip lines outside this region are widely spaced with large offsets similarly to those observed in deformation mode A. The load-extension curve for the 15<sup>a</sup>/o Al crystal is shown in Fig. 8 and is quite different from the curve for mode A in that a series of load drops occur (of about 200 lbs. in magnitude for each drop in load). The details of the load-extension curve indicate a fairly high work hardening rate followed by a sudden load drop. That there is a correlation between the formation of kink bands and the load drops is evident by the fact that the numbers of each are the same. To test this hypothesis the crystal was retested and the number of new kink bands was found to equal the increase in the number of load drops.

The details of the slip line structure at the kink bands shown in Fig. 16 suggest a lattice rotation across the kink band as evidenced by the slight change in direction of the slip lines. The angular change projected onto the crystal surface at kink band one is  $10^{\circ}$ . The slip lines bend back to their original direction at kink band two although, the angles are not exactly the same so any misorientation remaining must be compensated for in other kink bands so that the original orientation is restored outside the kink band region.

To obtain further insight into this lattice rotation a series of

back-reflection Laue photographs were taken as shown in Fig. 17. Laue (a) was taken to the right of kink band one (Fig. 16), Laue (b) in between kink bands one and two, and Laue (c) to the left of kink band two. Close inspection of the photographs e.g. spots numbered 1,2,3 and 4 shows a change of orientation of the spots going from (a) to (b) but regaining orientation (a) on going from (b) to (c). This is easily demonstrated by constructing a stereographic projection of Laues (a) and (b) as shown in Fig. 18. The spots have been indexed as 1 = (113), 2 = (112), 3 = (111) and 4 = (101), and it is immediately obvious that the (112) spot has not changed position. This suggests that a rotation has occurred about the [112] direction and by re-orienting the projection with the (112) pole at the centre it was shown that a rotation of  $12^{\circ}$  about this pole would bring the spots into coincidence. This value is very close to the  $10^{\circ}$  change in direction of slip lines measured at the surface.

The sharpness of the spots indicates that there is no lattice rotation in between kink bands, at least at the crystal surface. But it was further demonstrated that lattice rotation occurs at the kink band by taking a Laue with the X-ray beam right on the kink band. The expected asterism of the spots is shown in Fig. 19 .

From the geometry of the kink bands, and slip planes as related to a stereographic projection of the Laue showing the crystal orientation it appeared that if the slip planes were designated to be (111) planes and the slip vector [T01] then the kink band lay in the (T01) plane i.e., it was at right angles to the slip vector. This is consistent with rotation occurring about a  $\langle 112 \rangle$  direction (termed the roller axis) since

this direction is common to both (111) and (T01) planes. Thus edge dislocations of one sign lying in a  $\langle 112 \rangle$  direction and piled up on many parallel slip planes so that the pile-ups lay in a (T01) plane would explain all the features of the kink bands observed.

To test this model sections through the kink bands were examined by electron microscopy to discover the dislocation structure. The first section was taken nearly perpendicular to the kink bands ( $9^\circ$  from (10T) and at an angle of  $28^\circ$  to the (111) slip plane. A low magnification electron micrograph (Fig. 20) shows the dislocation structure in the region of kink bands. Pile-ups of dislocations on the (111) slip planes are cut by zones clear of dislocations which are thought to represent undeformed slip planes between the active slip planes. The electron diffraction micrograph from this region shows that the direction of clear zones is  $\langle 112 \rangle$  and the dislocation  $\langle 110 \rangle$ . In Chapter VI it will be shown how this structure can be explained in terms of the model proposed above. That these clear zones are associated with an orientation change is shown by studying the Kikuchi lines on electron diffraction patterns taken on each side of the zone. Fig. 21 shows how the Kikuchi lines (arrowed) change position on moving across the zone. This orientation change was calculated to be  $0.5^\circ$  and is thought to be due to relaxation of the clear areas because of the pile-ups, after cutting from the crystal. That the dislocations are in pairs in the pile-ups is evident from the electron micrograph shown in Fig. 22.

The section used for electron microscopy was also checked for asterism by a back reflection Laue and showed streaking as would be

expected (Fig. 23).

Considering now the deformation mode termed C for which the characteristics have been listed in Table III. These are, initially slip occurred in a narrow band only and slowly spread across the crystal as deformation increased. The associated load extension curve was sharply serrated as shown in Fig. 8. The magnitude of the load drops varies but it is in the order of 50 lbs.

The appearance of the crystal (17<sup>a</sup>/o Al) for 2% compressive strain is shown in Fig. 24(a) and a photograph of the slip band in Fig. 24(b). It can be seen that no slip lines appear outside this slip band. As strain increased the width of the slip band increased until it covered most of the crystal. The final appearance of the crystal after some 28% strain is shown in Fig. 25.

The spreading of the slip band indicates that new slip planes are being activated to account for the strain implying that existing slip planes become inactive. An attempt to show that this was occurring was made by measuring the height of slip steps on the surface by interferometry at intervals of strain. However, because new slip planes seemed to be activated very close to old ones the true step height of the latter was observed and the results were inconclusive. The slip structure was similar to that seen in the other crystals as illustrated by Fig. 26.

Using the technique adopted above no lattice distortion inside the slip band or change in orientation could be detected using back reflection Laue photographs. Fig. 27(a) shows no asterism from a Laue taken after 12% strain on the slip band and Fig. 27(b) shows the same

orientation in a region outside the slip band. This result would indicate that no kink bands are present in the structure as a result of deformation.

A section taken close to the (111) slip plane after 28% compressive strain showed a large amount of asterism as is evident from the Laue photograph in Fig. 28. As suggested above this type of asterism can be explained in terms of edge dislocations of one sign accumulating on the slip plane.

In order to investigate further the details of the structure various sections were examined by transmission electron microscopy. Fig. 29 is a micrograph of a (111) section and shows a high dislocation density but little detailed structure because it is on a fine scale. A section taken at right angles to the slip planes i.e. viewing the slip planes end-on was more informative. Fig. 30 shows dislocation debris lying on parallel slip planes and it is clear that the slip planes extend right through the particles. This was confirmed by taking a dark field micrograph from a superlattice reflection and showing that offsets occur in the particles indicating cutting (Fig. 31). The general dislocation structure is shown by a low magnification electron micrograph in Fig. 32. The braids of dislocations on closely spaced active slip planes with clear regions between the braids is consistent with the slip line structure seen at the crystal surface i.e. narrow slip bands consisting of many slip planes with large offsets separated by undeformed material. In Chapter VI it will be shown how the microstructure can account for the macroscopic deformation behaviour. A replica of the surface shows a narrow slip band passing through particles (Fig. 33).

#### 4.1.2 Crystals with Large Particles ( $> 1\mu$ )

##### 4.1.2.1 Crystals with large coherent particles ( $\sim 1\mu$ )

All the crystals were slow cooled from  $1300^{\circ}\text{C}$  to  $700^{\circ}\text{C}$  over a period of 3 hours and then water quenched. They were tested in compression up to the 0.2% flow stress but not beyond except for the 17<sup>a/o</sup> and 18<sup>a/o</sup> alloys. The resultant values of the calculated critical resolved shear stresses are given in Table III. All these values are below those for the alloys aged at  $700^{\circ}\text{C}$  for 6 hours except for the 18<sup>a/o</sup> alloy which is stronger in the slow cooled condition. Since it was found that this alloy contains incoherent particles this result will be included in the next section. The remaining results in this section will deal with the 17<sup>a/o</sup> Al only since it was studied extensively whilst no further work was done on the other alloys in this condition.

By this technique large cube-shaped particles about  $1\mu$  edge length and coherent with the matrix are obtained. Fig. 34 shows an electron micrograph of a carbon replica taken from a (100) section while Fig. 35 is the same taken from a (111) section. The particles have a square shape, with concave interfaces and are often grouped in fours. Coalescence appears to have occurred in some cases. Also, present are a large number of much smaller particles which formed during the late stages of the cooling cycle i.e. around  $700^{\circ}\text{C}$ , and possibly during quenching. That the particles are coherent is shown by the presence of strain contrast at the interface and absence of interface dislocations in a transmission electron micrograph (Fig. 36). A very striking electron micrograph from a (111) section in Fig. 37 shows a condition known as

" $\delta$ -fringes" which are due to a difference in deviations from the Bragg angle for the matrix and the particle. This difference arises because there is a small difference in lattice vectors of particle and matrix. This phenomenon has recently been discussed and accounted for by Ardell<sup>(67)</sup> and Oblak and Kear<sup>(68)</sup>.

It was shown that these coherent particles can become incoherent in two different ways, firstly cold work and secondly, on prolonged ageing at 700°C. Presenting first the results of the cold working treatment. Fig. 38 is an electron micrograph of the 17<sup>a</sup>/o Al crystal after 5<sup>a</sup>/o compression sectioned on the (100) plane showing the presence of dislocations at the interface, for example at A. However, it will be seen that strain contrast still exists at the interface marked B so the interfaces are more properly termed semi-coherent. On the basis of also examining (100) and (111) sections after cold rolling it was evident that some interfaces were still fully coherent without any dislocations while others contained dislocations and, since the strain contrast was less than for fully coherent interfaces, they will be called semi-coherent.

A major feature of interest in these foils was the observation of stacking faults in the particles eq. Fig. 38. Since it is well known that stacking faults bounded by  $\frac{a}{6} \langle 112 \rangle$  partials would have a high energy because of the associated APB energy the analysis of these partials is of considerable interest. Accordingly various diffracting conditions were obtained by using the durable tilt stage and an analysis made of the Burgers vectors of the partials and of the nature of the stacking fault.

Using the criteria<sup>(69)</sup> that dislocations are visible when  $\bar{g} \cdot \bar{b} = \pm 2/3$ , 1 and invisible when  $\bar{g} \cdot \bar{b} = 0, \pm 1/3$  the partials were analysed to be of the type  $a/3 \langle 112 \rangle$ . A composite electron micrograph consisting of 3 different reflecting conditions is shown in Fig. 41 and the details of the analysis of Table IV. The stacking fault was shown to be intrinsic following a rule of Gevers, et al<sup>(70)</sup>. This is for a 200 operating reflection under dark field conditions when  $\bar{g}$  is placed at the centre of the stacking fault and points towards the bright fringes the nature of the fault is intrinsic (Fig. 42).

Details of the dislocation particle interaction were obtained from a (111) section of the 17<sup>a</sup>/o Al crystal compressed 2%. Fig. 43 is an electron micrograph of this section showing two interactions of interest. At A there is a pile-up of glide dislocations held up at the corner of a particle and at B an example of the way in which 2 unit slip dislocations in the matrix constrict to form a superdislocation as they enter the particle. The pile-up is consistent with the high rate of work hardening observed during the compression test. Another electron micrograph in Fig. 42 shows very good evidence for the shearing of particles by large numbers of dislocations. A slip band containing dislocations is shown passing through several particles, the offsets at the interfaces are obvious. The displacement at these offsets is about 500 $\text{\AA}$  representing shear by about 200 dislocations. A comparison of the number of dislocations in the areas represented by Figs. 38, 43 and 44 shows that some regions are virtually dislocation free indicating inhomogeneous deformation. These observations agree with the widely spaced slip band having large offset on the crystal surface.

Other features of interest observed in these foils were the way in which a square grid of slip dislocations could form at an interface due to the intersection of two slip systems and the presence of dislocations in the narrow channels between particles in a cluster. The former is well demonstrated in Fig. 39 at area A and the latter in Fig. 40 in the cluster at A.

Turning now to the breakdown of coherency by ageing at 700°C for 4 weeks we see first the general shape of the particles in a carbon replica shown in Fig. 45. Firstly, it is evident that the smooth, curved concave interface has become irregular, secondly, that all the small particles have disappeared and thirdly, that a "precipitate" has appeared within the  $\gamma'$  particles. Transmission electron microscopy confirms these features and shows that dislocation networks have formed at the interface. Fig. 46 is again a (100) section and clearly shows that dislocation networks, somewhat irregular, have formed at some interfaces. Strain contrast is also present so again the interfaces should be more properly termed semi-coherent. A further point of interest concerns evidence that some dislocations cross the matrix between two particles and lie in both interfaces. No analysis of the Burgers vectors of the dislocations was made in view of the results presented in the next section on much larger fully incoherent particles.

#### 4.1.2.2 Crystals containing very large incoherent $\gamma'$ particles (~10 $\mu$ )

By using a very slow cooling procedure as described in Chapter III, very large irregular particles were obtained in the 17<sup>a</sup>/o Al crystal. The

particles had a general tendency to be spherical but often with facetting. Fig. 47 is an optical micrograph of a (100) section showing the general shape and distribution of the  $\gamma'$  particles. Again using a (100) section for transmission electron microscopy, Fig. 48 shows a  $\gamma'$  particle about  $14\mu$  long and  $7\mu$  wide with facetting on {110} planes. Facetting was also observed on {100} planes. The appearance of the dislocation networks is well illustrated by Fig. 49(a) which shows a large network lying on the (100) plane. Two dislocations are visible for this operating reflection 020, but on changing the conditions to obtain a 200 reflection (Fig. 49(b)) then two other dislocations appear. However, it was easily shown by comparing the two networks that one dislocation was common to both reflections and that the network consisted of three dislocations in a distorted hexagonal array.

In order to conduct an analysis of the Burgers vectors of the network dislocations another area was chosen and subjected to the same operating reflections as above. Fig. 50(a) shows the dislocation network of a particle for a 020 reflection and Fig. 50(b) for a 200 reflection. The planes containing the networks are at an angle to the foil plane of (100) since their projected width is greater than the expected foil thickness ( $\sim 1000\text{\AA}$ ). The analysis was completed by examining a foil close to a (112) orientation in which a network lying on a (111) plane was examined. Fig. 51 shows the network under two different reflecting conditions.

From the criteria used in the last section for determining the Burgers vectors the only values of Burgers vectors consistent with both the reflecting conditions used and planes on which the networks lie in

Figs. 49, 50 and 51, are dislocations of the type  $a/2 \langle 110 \rangle$ . The analysis is summarised in Table IV along with estimates of the dislocation spacings in the networks.

The mechanical properties of crystals containing large incoherent particles show some difference to the ones containing small coherent particles. The 18<sup>a</sup>/o Al crystal in a compression test showed a smooth load-compression curve and a very high rate of work hardening. When converted to a shear stress-shear strain curve (Fig. 52) the initial work hardening rate was  $G/4$  ( $G$  is the shear modulus) reducing to  $G/60$  after 4% shear strain. Slip line markings on the crystal surface were not visible in the optical microscope. This observation and the high rate of work hardening are consistent with the behaviour typical of a hard particle dispersion strengthened metal. The microstructure of this crystal is shown by the optical micrograph of Fig. 53 taken from a (111) section. This crystal was slow cooled from 1300<sup>o</sup>C to 700<sup>o</sup>C in 3 hours and not over 3 weeks as was the case for the 17<sup>a</sup>/o Al crystal discussed above, but gave a similar structure. Electron microscopy confirmed that the particles in the 18<sup>a</sup>/o Al were also incoherent (Fig. 54).

A feature of interest observed in the electron micrographs concerns the presence of coherent particles in conjunction with the incoherent ones. These were identified by their more regular shape and the presence of strain contrast. An example of this is given in Fig. 55 where coherent particles (a) are found close to incoherent particles (B).

One final observation in this section concerns the examination of a foil cut from a crystal aged in a similar manner to the 17<sup>a</sup>/o Al crystal

discussed above. As shown in Fig. 56 the interfaces of the  $\gamma'$  particles show strain contrast and the complete absence of dislocations.

## 4.2 The Mechanical Properties of Polycrystalline Alloys

### 4.2.1 Compression tests

In order to determine the effect of the volume fraction of  $\gamma'$  on the mechanical properties, cylindrical specimens containing from 0 to 1.0 volume fraction were tested in compression after ageing at 700°C for various times. The results of these tests are shown in Fig. 57 where the 0.2% yield stress is plotted against volume fraction of  $\gamma'$  for different ageing temperatures. An estimate of the work hardening rates were obtained by measuring the slope of the load-compression curve at 1% strain at the 1 hour ageing treatment (Fig. 58). The 0.2% yield stress has also been plotted against the ageing time for each volume fraction (in %) as shown in Fig. 59. Grain sizes are given in Table II.

The important features of these results are,

- i) a peak in yield strength at 0.45 volume fraction  $\gamma'$  (17<sup>a</sup>/o Al) irrespective of ageing time.
- ii) for each volume fraction peak strength occurs after 3 hours ageing time.
- iii) the strength varies little over a range of about 0.3 to 0.7 volume fraction  $\gamma'$  then falls sharply on each side of this range.
- iv) ageing time has more effect on strength at low volume fractions than at high volume fractions.
- v) the work hardening increases continuously as the volume fraction  $\gamma'$  is increased from 0 to 1.

The surface slip line structure on the polished flats of the compression samples was examined after 1-2% strain by optical microscopy. The amount of  $\gamma'$  present in the alloys did not appear to affect the slip line structure across the grains with the exception of the pure  $\text{Ni}_3\text{Al}$  alloy. At these small strains, slip lines were generally widely spaced, had large offsets and were very long often covering the width of a grain. Deformation was inhomogeneous in that some grains were deformed more than others. Fig. 60 is an optical micrograph of the 13<sup>a</sup>/o Al alloy after 1% strain showing the slip line structure typical of these alloys at low strains. Higher strains activate slip planes between the ones shown in Fig. 60. The pure  $\text{Ni}_3\text{Al}$  alloy showed very fine slip lines which could only be detected at high magnifications (Fig. 61). This structure is typical of ordered intermetallic compounds of the  $\text{L1}_2$  type at room temperature<sup>(71)</sup>. The solid solution without  $\gamma'$  particles also showed the presence of fine slip lines (Fig. 62).

The main distinguishing feature between low volume fraction and high volume fraction alloys was the presence of grain boundary cracking in the latter but not the former. An example of this is shown in Fig. 63 from the 19<sup>a</sup>/o Al alloys. Grain boundary cracking was observed in alloys with 17<sup>a</sup>/o Al and over sometimes being so severe that whole grains fell out of the specimen. In the low volume fraction alloys there were always enough slip systems to accommodate the shape change of grains at grain boundaries whereas this did not always seem to be the case in the high volume fraction alloys. For example areas adjacent to the grain boundary

cracking in Fig. 63 have few slip lines whereas in a low volume fraction alloy (14<sup>a</sup>/o) shown in Fig. 64 there is profuse slip in such areas. There was some evidence that grains moved relative to each other along the grain boundaries in the high volume fraction alloys. Observation of the compressed specimens in the optical microscope showed that often adjacent areas at grain boundaries were not in the same focal plane and there was an offset at the boundary. The number of slip lines in these areas could not have accounted for this relative movement. Some further evidence was obtained from a bi-crystal of the 17<sup>a</sup>/o Al in which the movement of a scratch across the grain boundary was observed. Fig. 65 shows that relative movement of the scratch has occurred between the parts on each side of the boundary. Again absence of slip lines suggests that grain boundary sliding has occurred.

One final feature of grain boundary cracking concerns that seen in the pure Ni<sub>3</sub>Al. The cracking at individual boundaries is not as severe as in the two phase alloys but it is more widespread.

Some of the alloys solidified in the two phase region and contained massive  $\gamma'$  precipitate. These alloys had a very high rate of work hardening but the slip line pattern did not appear to be affected by the presence of this massive precipitate. Fig. 66 shows the 21<sup>a</sup>/o Al alloy with massive  $\gamma'$ . At a high magnification slip lines could be seen in the  $\gamma'$  phase which did not appear to continue into the matrix. However, this may well have been due to the etching necessary to outline the  $\gamma'$  phase obscuring the slip lines in the matrix.

An attempt was made to prepare thin films from compression

specimens by spark-cutting a section and electro-thinning by the window technique. However, preferential attack at the grain boundaries made this method unusable. Since sections of single crystals were thinned without difficulty no further attempts were made to thin sections from polycrystalline compression specimens. Instead carbon replicas were prepared from the polished flats on the surfaces on the specimens. Fig. 67 shows the 17<sup>a</sup>/o Al alloy, Fig. 68 the 20<sup>a</sup>/o Al alloy and Fig. 69 the 21<sup>a</sup>/o Al; the ageing time was 1 hour at 700<sup>o</sup>C in each case.

#### 4.2.2 Tensile tests

In order to determine more definitively the effect of ageing time on strength for different volume fractions of  $\gamma'$ , polycrystalline strip specimens were tested in tension over a range of ageing times from zero to 1 week. The grain size was 0.3 mm as measured from lineal analysis. The results of these tests are shown in Fig. 70 where the 0.2% yield stress is plotted against volume fraction for each ageing time. In Fig. 71 the 0.2% yield stress is plotted against ageing time as a function of volume fraction and in Fig. 72 the % elongation at fracture is plotted against the volume fraction  $\gamma'$ .

The important features of these results are summarised below.

- i) the strongest alloy in the composition range studied was the 17<sup>a</sup>/o Al alloy.
- ii) the yield strength increased rapidly as the volume fraction  $\gamma'$  increased from zero to 0.23 and then more slowly to the peak strength at 0.45 volume fraction.
- iii) peak strength at each volume fraction occurred after 6 hours

ageing at 700°C. The strength decreased slowly on overageing up to the longest time used (1 week).

iv) The strength of the quenched alloys increases with volume fraction  $\gamma'$ .

v) the ductility decreases as the volume fraction  $\gamma'$  increases.

These features are consistent with those found in the compression tests with the added information that overageing occurs after 6 hours and estimates of the ductility as a function of volume fraction  $\gamma'$ . The fact that alloys with more than 17<sup>a</sup>/o Al could not be rolled because of brittleness and even the 17<sup>a</sup>/o Al was difficult, confirms the observation of brittleness due to grain boundary cracking. The alloys failed in tension by intercrystalline fracture irrespective of volume fraction  $\gamma'$ . However considerable deformation occurred in the region of the fracture for the low volume fraction alloys (i.e. 13<sup>a</sup>/o Al) but decreased to very little at high volume fractions (i.e. 17<sup>a</sup>/o Al).

As is well documented  $\gamma'$  precipitates in these alloys as cube-shaped particles with faces parallel to {100} matrix planes (the initial precipitate appears to be spherical and becomes cube shaped at about 50Å diameter<sup>(6)</sup>). After long ageing times the particles tend to become platelets aligned in <100> directions as shown by Ardell and Nicholson<sup>(5)</sup> and Phillips<sup>(6)</sup>. These two investigations were done on low volume fraction  $\gamma'$  alloys, viz. 13.5<sup>a</sup>/o Al (0.14 $\gamma'$ ) and 12.7<sup>a</sup>/o Al (0.06 $\gamma'$ ) respectively and the coarsening behaviour of alloys with a high volume fraction  $\gamma'$  is not known. Accordingly the 16<sup>a</sup>/o Al (0.37 $\gamma'$ ) was aged at 700°C for 1 week and 3 weeks and the resulting electron micrographs

taken in dark field are shown in Fig. 73. The 1 week sample is shown in Fig. 73(a) and the 3 week sample in Fig. 73(b). Clearly alignment occurs but platelets are only evident in the sample aged for 3 weeks.

To assist in the analysis of the above data on mechanical properties particle size measurements were done on foils prepared from strip containing 16.5 at% Al ( $0.42\gamma'$ ) after different ageing times at  $700^{\circ}\text{C}$ . These results are presented in Fig. 74 along with particle sizes of the 13.5 at% Al ( $0.14\gamma'$ ) taken from the data of Ardell and Nicholson<sup>(5)</sup>.

#### 4.3 Long Range Order Measurement

It is well known that long range order in the  $\gamma'$  particles affects the APB energy which has a strong influence on mechanical strength. Hence an attempt was made to measure the long range order as a function of ageing time to help throw light on the effect of ageing time on mechanical properties.

Profiles for the 100 and 200 reflections were obtained from a (100) section of a 16 at% Al crystal mounted in a diffractometer and scanned after several different ageing times. Cu K $\beta$  radiation was used and the area under the peaks in arbitrary units is plotted against ageing time at  $700^{\circ}\text{C}$  for the intensity of the 100 peak and for the ratio 200/100 (Fig. 75). Since the intensity of the superlattice reflection 100 is a function of the long range order in the  $\gamma'$  particles the results show that this parameter increases with ageing time. The increase is rapid with ageing time up to 6 hours and thereafter increases much more slowly.

#### 4.4 Splat Cooling

In order to gain more insight into the decomposition of the alloy on quenching some of the alloys containing high volume fractions of  $\gamma'$  were subjected to splat cooling and then examined by transmission electron microscopy before and after ageing at  $700^{\circ}\text{C}$  for 3 hours. Fig. 76(a) shows the 21 at% Al alloy in the splat quenched condition and Fig. 76(b) the same after ageing at  $700^{\circ}\text{C}$  for 3 hours; both are dark field pictures. The first electron micrograph appears to show particles of  $\gamma'$  separated by a film of the  $\gamma$  phase while the second shows  $\gamma'$  particles only separated by anti-phase boundaries. The hardness of the alloy increased from 273 as splat cooled to 356 after ageing for 3 hours at  $700^{\circ}\text{C}$ , as measured on the Knoop hardness scale. This change in hardness is very likely due to an increase in the L.R.O.

In order to get some idea of the magnitude of the L.R.O. in splat cooled samples, measurements of the intensity from the 100, 110, 200 and 220 reflections were obtained for the pure  $\text{Ni}_3\text{Al}$  alloy in the as quenched condition and after ageing. The value of the ratios 200/100 and 220/110 can be calculated for the fully ordered condition i.e.  $S = 1$ , and compared to the experimental ratios. This comparison will give the values for the L.R.O. parameter,  $S$  in the two conditions. The details of the calculation and the resulting experimental values for  $S$  are given in Table VI. It can be seen that even in the splat cooled condition pure  $\gamma'$  is still strongly ordered ( $S = .73$ ) and that this order increases with the ageing treatment ( $S = .9$ ). Thus for very high volume fraction  $\gamma'$  alloys ( $\sim 0.8$ ) considerable order exists in quenched samples.

## CHAPTER V

### THE FORMATION OF $\gamma'$ PARTICLES FROM SOLUTION

#### 5.1 On Splat Cooling

That classical nucleation of a clump of  $\gamma'$  of equilibrium composition of a critical size which grows to form a  $\gamma'$  particle is not essential is shown by the results obtained on splat cooling a liquid alloy. These results indicate that regions of a second phase can form under these conditions which exhibit properties characteristic of the  $\gamma'$  particles found after ageing. For example, they show long range order as evidenced by the dark field electron micrographs taken from superlattice lines (in Fig. 76) of a Ni-21<sup>a</sup>/o Al alloy. The degree of order, at least in high volume fraction  $\gamma'$  alloys, can be high as shown by a value of 0.76 for the L.R.O. parameter in pure Ni<sub>3</sub>Al as splat cooled (Table VI).

The rate of cooling on splat cooling is very high ( $\sim 10^6$  C<sup>o</sup>/sec during solidification<sup>(73)</sup>) and thus a diffusion controlled mechanism for the formation of the  $\gamma'$  appears to be ruled out. It is more likely that  $\gamma'$  is formed by an interface-controlled process which does not involve long range diffusion and thus does not involve composition changes. Such a reaction is characterised by a chemical potential step at the interface where pairs of atoms change places to give ordering at the composition of the alloy. This reaction should occur rapidly because of the high degree of order obtained and the large decrease in free energy accompanying the ordering process. The regions of  $\gamma'$  probably

have their origin in the regions of short range order which act as 'nuclei' for  $\gamma'$  formation.

The formation of  $\gamma'$  is not complete in the Ni-21<sup>a</sup>/o Al alloy. Fig.76(a) shows the  $\gamma$  phase separating the  $\gamma'$  regions. On ageing however the  $\gamma$  phase disappears leaving a structure consisting only of  $\gamma'$  regions separated by APB's (Fig. 76(b)). This evidence would lend support to the above model. It should be emphasised that this discussion applies only to high volume fraction  $\gamma'$  alloys. For lower volume fraction alloys (~17% Al) although  $\gamma'$  regions form on splat cooling an ageing treatment would change their composition to equilibrium and they would grow as  $\gamma'$  particles in a  $\gamma$  matrix.

## 5.2 On Water Quenching From Solid Solution

$\gamma'$  particles are found on quenching solid solution alloys from high temperatures. Ardell and Nicholson<sup>(5)</sup> detected faint superlattice lines after quenching their 13.5<sup>a</sup>/o Al alloy but Phillips<sup>(6)</sup> did not in his 12.7<sup>a</sup>/o Al alloy. In this work superlattice reflections were detected in the 14<sup>a</sup>/o Al alloy and all higher compositions; the strength of superlattice spots in the electron microscope increased with increasing Al content. The maximum possible value of S (the L.R.O. parameter) is 0.49 for a fully ordered 14<sup>a</sup>/o Al alloy (calculated from the Bragg-Williams relation) and for a 16<sup>a</sup>/o Al it is 0.57 .

It is possible that with this rate of cooling sufficient diffusion can occur to form equilibrium  $\gamma'$  particles. Using the Zener<sup>(74)</sup> approximation, for diffusional growth of particles, and allowing average values

of  $D = 10^{-12}$  cm<sup>2</sup>/sec and  $t = 1$  sec gives radii of the right order for the 16% Al alloy. Fig. 77 shows a 16<sup>a</sup>/o Al alloy as quenched with particle diameters of about 150Å. However the fact that as-quenched alloys show a low degree of long range order (see Fig. 75 for the 16<sup>a</sup>/o Al alloy) indicates that a diffusionless mechanism cannot simply be ruled out. Even allowing for an increase in volume fraction of precipitate would not account for the large increase in superlattice line intensity that occurs on ageing. If particles do form diffusively with near-equilibrium composition in sufficiently concentrated alloys, they must somehow be prevented from reaching the equilibrium degree of order at small diameters.

Fig. 78 shows a schematic free energy versus composition diagram for Ni-Al alloys. Any alloys with above about 14<sup>a</sup>/o Al can lower their free energy by forming regions of  $\gamma'$  with the same composition by a diffusionless reaction. Those alloys with less than this amount cannot lower their energy in this way. Thus the observed composition-dependence of the tendency to form  $\gamma'$  on water quenching is not inconsistent with a diffusionless transformation. However, diffusional formation seems more likely as the data of the next section indicate.

### 5.3 On Ageing

As shown by Ardell and Nicholson<sup>(5)</sup>  $\gamma'$  particles in low volume fraction alloys grow on ageing following a  $t^{1/3}$  law. The 16.5<sup>a</sup>/o Al appears to behave the same way as shown by particle sizes after 3, 6 and 9 hours ageing time (Fig. 74). This suggests a ripening of the Ostwald kind and,

by implication, equilibrium composition in the particles. As noted above the L.R.O. is very small in the as-quenched alloys. It is still low in the early stages of ageing compared with the value after 24 hours (Fig. 75). This is consistent with Gleiter and Hornbogen's<sup>(45)</sup> suggestion that small particles have a low degree of order in their surface regions and a higher degree of order at the centre. Thus the overall degree of order would be small since most of the particle volume is in the near-surface layers at small sizes.

Ardell<sup>(22)</sup> has shown that during the ageing of a 13 at% Al alloy the composition of the matrix decreases by about 0.5 at% Al with ageing time. It is obvious from this that unless the  $\gamma'$  composition changes in harmony then the volume fraction must change. Ardell's results show that after ageing for  $\frac{1}{2}$  hour the aluminum concentration in the matrix is 6.17 w/o. For an alloy of 6.5 w/o Al and assuming the composition of  $\gamma'$  to be 12.1 w/o then the weight percentage of  $\gamma'$  is 5.5%. If the composition of the matrix at infinite ageing time is 6.049 w/o Al then the weight percentage of  $\gamma'$  should be 7.5%. Ardell and Nicholson<sup>(5)</sup> believe that they reach the equilibrium volume fraction very rapidly but their evidence based on a foil thickness calculation is admittedly crude. With present techniques (particularly when looking at small particles) it seems unlikely that a change in the amount of  $\gamma'$  from 5.5 w/o to 7.5 w/o could be detected.

It has been shown by Purdy<sup>(75)</sup> and Oriani<sup>(20)</sup> that the two factors which could cause the equilibrium particle composition to change are the Gibbs-Thompson effect and the strain energy effect respectively.

Both effects push the equilibrium composition nearer to stoichiometry and we believe that to a first approximation these two effects are additive.

Using Oriani's<sup>(20)</sup> equations (4) and (7) with the following values, (see Appendix B)

$$x_B^{\beta i} = .231, x_B^{\alpha i} = .123, G_\alpha = 6.4 \times 10^{11} \text{ dynes/cm}^2, K_\beta = 7.45 \times 10^{-13} \text{ cm}^2/\text{dyne}, V_m^\beta = 6.79 \text{ cm}^3/\text{mol}, V_m^\alpha = 6.65 \text{ cm}^3/\text{mol} (V_B^\beta - V_A^\beta) = (V_B^\alpha - V_A^\alpha) = 0.94 \text{ cm}^3/\text{mol}, \frac{\Delta V}{V} = 3 \frac{\Delta a}{a} = 3 \times .00529, \text{ we find that the composition}$$

change due to elastic strain caused by coherency is 0.55 at% Al in both particle and matrix. That is the coherent solubility in the matrix is increased by 0.55 at% Al and the composition of a coherent particle is moved 0.55 at% Al closer to stoichiometry. Oriani assumes that the thermodynamic factor  $e = (1 + \frac{\partial \ln \gamma}{\partial \ln x})$  is unity in both cases i.e.

$\frac{\partial \ln \gamma}{\partial \ln x} = 0$ ; however from the recent data of Hanneman and Seybolt<sup>(76)</sup> we find that  $\frac{\partial \ln \gamma_B^\alpha}{\partial \ln x_B^\alpha} = 1.95$  and  $\frac{\partial \ln x_B^\beta}{\partial \ln x_B^\beta} = 6.3$ . Thus  $e^\beta = 7.3$  and  $e^\alpha = 2.95$  and applying these corrections to Oriani's equations then the matrix composition is changed by 0.19 at% Al and that of the particle by 0.075 at% Al.

In his calculation of the Gibbs-Thompson effect on solubility, Purdy<sup>(75)</sup> has considered particles of 50 Å radius and a surface tension of 45 ergs/cm<sup>2</sup> (Ardell's<sup>(22)</sup> estimate multiplied by  $e^\alpha$ ) and finds that the composition change in the matrix is 0.3 at% Al. With the above effect of strain energy considered by Oriani the two effects combined would give a composition change in the matrix of about 0.5 at% Al and this value is very close to the results of Ardell<sup>(22)</sup>. We suggest then that Ardell has measured the result of two effects. Firstly, as the particles coarsen the Gibbs-Thompson effect becomes less and the solubility of the matrix decreases. Secondly, there is a relaxation of elastic energy which also

causes a decrease in solubility of the matrix. This relaxation of elastic energy is presumably a consequence of the elastic interaction between particles which results in particle alignment<sup>(5)</sup>.

Rastogi and Ardell<sup>(25)</sup> have also attempted to calculate the incoherent solubility using Oriani's treatment and found that it is 2<sup>a</sup>/o Al less than the coherent solubility at 700°C. This is considerably different from the above value of 0.19<sup>a</sup>/o Al and is due to their using a value of 27.92 cm<sup>3</sup>/mol for the molar volume of  $\gamma'$  (correct for the Wagner-Lifshitz analysis, but not for Oriani's) when it should be 6.79 cm<sup>3</sup>/mol, and also ignoring the thermodynamic factor.

In summarising this section we have seen that both the volume fraction of  $\gamma'$  and the L.R.O. in the particles increase with time. Whether or not the increase in volume fraction can be measured by present techniques is difficult to say, however it would certainly be a contribution to the increase in strength with ageing time. The L.R.O. increases dramatically on ageing; after ageing for 9 hours the intensity of the 100 superlattice reflection has increased 20 times over the as quenched value. It is not clear why ordering takes such a long time since, as discussed above, the ordering process is accompanied by a large decrease in free energy. As Gleiter and Hornbogen<sup>(45)</sup> have suggested it may be due to the low degree of order in the surface layers, an effect which is still appreciable at 400Å diameter according to their calculations. This increase in L.R.O. should have a large effect on strength because it determines the value of the APB energy. Since APB energy is proportional to  $S^2$  (the L.R.O. parameter) and the intensity of the 100 reflection is proportional to  $S^2$ , the APB energy increases directly as intensity.

Thus the APB energy increases by a factor of  $\sim 6$  between ageing for  $\frac{1}{2}$  hour and 6 hours. The effect of this on strength will be discussed in Chapter VIII.

## CHAPTER VI

### THE DEFORMATION OF SINGLE CRYSTALS

#### 6.1 Crystals Containing Small $\gamma'$ particles ( $<0.1\mu$ )

Single crystals containing from 13<sup>a</sup>/o Al to 18<sup>a</sup>/o Al were deformed in compression and studied for surface slip line structure, by X-ray diffraction and electron microscopy. The results of the compression tests and pertinent observations are given in Table III. A graph of C.R.S.S. against volume fraction  $\gamma'$  is given in Fig. 83 showing an almost linear relation. A discussion of this relationship will be included in Chapter VII.

The macroscopic deformation behaviour depends on the volume fraction of  $\gamma'$  present in the alloy and has been summarised in Chapter IV. In discussing the deformation mode termed A which was exhibited by the 13<sup>a</sup>/o and 14<sup>a</sup>/o Al crystals we see that it is characterised by a coarse slip line structure over the whole crystal except for a region of intense slip about 0.070" wide. The slip lines circumscribe the crystal as is characteristic of single slip. The general appearance of the crystals is shown in Fig. 6 and the slip line structure at the edge of the intense slip band in Fig. 7. Notice that the 'slip band' direction coincides with the slip lines suggesting that it is solely a region of intense slip i.e. a large number of slip planes are operating. This conclusion was confirmed by back reflection Laue photographs taken on the crystal surface at the slip band and outside it. The resulting photographs in Fig. 10 show that there is no orientation change in the

slip band nor any asterism.

It is thought that the intense slip band is caused by the constraint between the specimen ends and compression plate restricting rotation of the specimen axis. The resulting stress concentration is relieved by the formation of a region of intense slip. Notice that one end of the slip band is very close to the end of the specimen and in the 14<sup>a</sup>/o Al a second slip band is beginning to form on another slip system at the end opposite to the first one. That this is a consequence of geometry is shown by the compression of a 0.2" length of the 14<sup>a</sup>/o Al crystal without the formation of an intense slip band (Fig. 11). With this size of specimen the slip planes intersect the specimen ends and thus cannot give the large offset at the specimen end-compression plate interface that this kind of slip band demands. Thus a large number of slip planes become active over the whole crystal as shown in Fig. 11.

The load-compression curve was smooth as shown in Fig. 8. The corresponding shear stress-shear strain curve in Fig. 9 shows a linear slope with a work-hardening rate of  $G/530$  which is considerably higher than for pure metals. However, it is well known that solute additions have a marked effect on the work hardening of pure metals and to be consistent with the single slip it is believed that this represents work hardening in stage I. Furthermore, the lattice rotation as calculated from the relation  $\frac{\ell_1}{\ell_0} = \frac{\cos \lambda_1}{\cos \lambda_0}$  where  $\ell_0$  is the original length  $\ell_1$  is the final length  $\lambda_0$  and  $\lambda_1$  are the initial and final angles between compression axis and slip plane respectively, gives a rotation of about  $4^\circ$ . This rotation is insufficient for the compression axis to reach the

symmetry line and activate another slip plane.

The transmission electron micrographs from a (111) section of the 14 <sup>a</sup>/o Al crystal are shown in Figs. 12 and 13. The important features of the micrographs are dislocation loops round particles, paired dislocations and offsets in particles as revealed in dark field. As shown in Chapter IV the interparticle spacing is such that bowing of dislocations between particles sufficient to cause loops can easily occur. Double loops or tangles are not seen round particles because the particles repulsion from a second loop will cause the first one to collapse. Since the collapse of a single loop would cause anti-phase boundary to be formed it seems very likely that loops would collapse in pairs to give shear without APB, i.e. a superdislocation. However it is not likely that looping would occur by two dislocations together since Ashby<sup>(77)</sup> has shown that twice the shear stress is required. The loops seen in Fig. 12 are approximately ellipsoidal in shape and the smallest loop observed had dimensions of 405Å along the shorter axis and 520Å along the longer axis. This gives an average diameter of 462Å which is considerably larger than the figure of 240Å for the minimum diameter possible, calculated from Brown et al<sup>(29)</sup>. A correction should be applied to Brown et al's calculation because of the effect of the APB energy in ordered particles. The addition of this term means that smaller loops than those obtained by Brown et al's calculation should be stable. Their equation (2) then becomes

$$E_{int} = -4\pi G b \epsilon r_{crit}^2 - \pi r_{crit}^2 \gamma$$

where G is the shear modulus,  $\epsilon$  the strain parameter,  $\gamma$  the APB energy

and  $r_{crit}$  the required radius. Differentiating their equation (1) and the above equation with respect to  $r_1$  and equating gives an equation for  $r_1$  as

$$r_{crit} = \frac{Gb^2}{2(1-\nu)(8\pi Gb\epsilon + 2\gamma\pi)} \left[ \frac{\ln 8r_{crit}}{b} \frac{3-2\nu}{4(1-\nu)} \right]$$

Using values of  $G = 7.5 \times 10^{11}$  dynes/cm<sup>2</sup>,  $\nu = 1/3$ ,  $\epsilon = .0038$ ,  $\gamma = 150$  ergs/cm<sup>2</sup> then  $r_{crit} = 80\text{\AA}$ . This is a significant difference from the first value of  $120\text{\AA}$ . However the figure of  $80\text{\AA}$  is very uncertain because the particles may not be fully ordered so that the value of  $\gamma$  would be smaller than the one used. Nevertheless, there is a seeming discrepancy between these theoretical and experimental values for  $r_{crit}$ . Not too much reliance can be placed on the value of  $230\text{\AA}$  as a lower limit to the radius of loops, however, because of the small area examined, and the fact that the average size of particles is larger than the theoretical lower limit.

The fact that double loops are not seen can be accounted for by using Brown et al's equation for  $r_{crit}$ . In this case we ignore any contribution from the APB term and replace  $b$  by  $2b$  hence  $b^2$  becomes  $4b^2$ . Thus for double loops to be stable the particles would have to have a radius of  $4 \times 120 = 480\text{\AA}$  which is larger than the average size ( $\sim 380\text{\AA}$ ).

It is well known that dislocations tend to move in pairs in a matrix containing ordered particles, the distance between dislocations in a pair being dictated by the particle spacing and volume fraction of the particles. With this sort of dispersion and after deformation

at room temperature, dislocations are not likely to be seen passing through particles because the APB energy will cause the dislocations to be forced out the particles, when the load is removed. Thus it is difficult to estimate the spacing of dislocations in pairs because the static condition does not represent the situation under dynamic loading.

The electron micrograph in Fig. 13 shows evidence of particles being cut. Whether this is caused by the collapse of loops or the cutting by straight dislocations is uncertain since the net effect is the same; probably both are occurring at the same time. Finally, from Fig. 14 we see that lattice bending occurs on the (111) plane as shown by the asterism in the Laue photograph. Local accumulation of edge dislocations of one sign on the (111) plane would cause this effect.

Turning now to those crystals which deformed by mode B we see that the characteristics are kink bands in regions of intense slip accompanied by load drops during compression. It was shown that the load drops coincided with the formation kink bands. The shape of the crystal and the change of direction in the plane at the kink band are shown in Figs. 15 and 16. The back reflection Laue photographs taken on the crystal surface (Fig. 17) give some insight into the crystallography of the kink bands. In Chapter IV it was shown that the kink band had the plane ( $\bar{T}01$ ) i.e. at right angles to the slip vector and that the orientation change across the kink band using a roller axis of  $[112]$  was consistent with the change in slip direction seen at the crystal surface. The electron micrographs (Figs. 20) showed parallel braids of dislocations on the (111) plane with clear regions in the  $\langle 112 \rangle$

direction and the dislocations lying in the  $\langle 123 \rangle$  direction. The orientation change across these clear areas was shown from Kikuchi lines to be about  $0.5^\circ$ . It remains to correlate the Laue photographs and electron micrographs and show how the kink bands formed.

It is generally believed<sup>(51,56)</sup> that kink bands result from the accumulation of edge dislocations of one sign on parallel planes so that pile-ups occur in a plane at right angles to the slip vector. The kind of dislocation structure envisaged is shown in Fig. 79. This is obviously very similar to the structure at the surface as seen in Fig. 16. Using this model as a basis it will now be shown how the structure seen in the electron micrograph can be explained. Remembering that the foil was cut about  $28^\circ$  from the (111) planes a section at this angle is shown through a two parallel (111) plane containing edge dislocations lying in the  $\langle 112 \rangle$  direction in Fig. 80. Looking in the direction of the arrow as shown will give the microstructure shown in Fig. 20. The direction of the dislocations is  $\langle 112 \rangle$  and they are stacked vertically in {110} planes i.e. the kink planes. The section representing the foil is shown by the dotted line and the part of the dislocation lines seen in the foil by the heavy lines. The direction of the electron beam is indicated and it can be seen that the clear areas in the foil are slip planes not containing dislocations. The direction of the dislocations in the model is  $\langle 112 \rangle$  and that of the clear areas is  $\langle 110 \rangle$ . However because the foil is cut at an angle of  $28^\circ$  to the (111) plane and  $10^\circ$  to the (110) these directions are changed when projected onto the microscope screen. These directions of  $\langle 123 \rangle$  for

the dislocation lines and  $\langle 112 \rangle$  for the direction of the clear areas are consistent with the foil normal of  $\langle 541 \rangle$  (as determined by back reflection Laue photograph), tilted to a  $\langle 210 \rangle$  orientation.

The change in Kikuchi line position across the clear areas has shown that a change in orientation across this region occurs. Since there are no dislocations in these areas it is not obvious why this should occur. It is thought that on sectioning and thinning elastic relaxation occurs because of the plastic regions on each side. This elastic relaxation causes bending of the foil across this region sufficient to cause the Kikuchi lines to move.

The electron micrograph indicates that a kink band as seen at the crystal surface is composed of a large number of edge dislocation pile-ups in vertical arrays along the  $\langle 112 \rangle$  direction. The end constraint causes localised slip as in mode A but because the alloy is stronger slip is more difficult to nucleate. Since the Schmid factor on the system  $(T01)[111]$  is just as high on the normal slip mode a high stress is placed on this system. By a co-operative movement dislocation pile-ups on parallel  $(111)$  slip planes align to give a  $(T01)$  tilt wall so that strain occurs on this plane to accommodate the shape change imposed by the testing conditions. The back reflection Laue photograph in Fig. 23 taken on the  $(111)$  plane shows asterism indicating lattice bending along this plane. This would be consistent with the type of dislocation pile-up indicated above.

The model implies that a large number of small lattice rotations due to pile-ups of edge dislocations can better accommodate stress in

the lattice when they co-operate to form edge walls on a (110) plane. The predominance of edge dislocations suggests that the screw components have escaped out of the crystal. This they can do more easily than edges by cross-slip; furthermore, screw pile-ups probably don't interact as strongly as edge pile-ups, i.e. passing stress is lower.

The third mode of deformation C (Table IV) shows a serrated load-compression curve with initially one narrow slip band which spreads along the length of the specimen. Fig. 24 shows the shape of the crystal in the early stages of compression and Fig. 25 after 28% compressive strain. The structure on the surface consists of coarse slip lines i.e. large offsets and widely spaced (Fig. 26). Back reflection Laue photographs taken at the surface inside and outside the slip band show no change in orientation (Fig. 27). After 28% compressive strain there is considerable asterism on the (111) slip plane (Fig. 28).

Since slip is localised it is believed that initiation of slip is difficult because of the high volume fraction of  $\gamma'$  on the slip planes. Once it has started slip continues on a slip plane more easily because shearing of particles results in a reduction of the particle diameter on the slip plane and consequently of the back stress due to the APB energy of the particle. This occurs rapidly such that avalanches of slip are produced on those planes on which slip is occurring to give the load drops seen in the serrated load-compression curve. Work hardening must then occur on these planes to stop them operating so that the load has to rise to initiate new slip planes. Accumulations (tangles) of dislocations on work hardened slip planes help to initiate slip on adjacent planes so that the slip band slowly spreads along the

specimen length.

One mechanism that gives rise to load drops but seems unlikely is due to adiabatic softening. In this case the very rapid slip produces local heating and results in softening on the slip planes so that the stress for slip reduces. However, an increase in strain rate by a factor of ten did not change the load-extension curve other than increase the overall slope of the curve. With more rapid straining larger serrations might have been expected because of more heating. Furthermore, it is known that  $\gamma'$  particles increase the strength of the alloy as the temperature is raised as Beardmore et al<sup>(46)</sup> have shown.

The large amount of asterism on the (111) plane after 28% compressive strain reflects the fact that not only are edge dislocations piled-up on the slip plane but also a great many have been active because of the large amount of deformation.

The electron micrographs of the slip plane Fig. 29, shows a high density of dislocations. The dislocations appear to go round the  $\gamma'$  particles but the structure is too dense to show any details. A section perpendicular to the (111) slip planes reveals dense concentrations of dislocations confined to their slip lines (Fig. 30). A higher magnification electron micrograph (Fig. 32) shows that many slip planes are active in slipped regions. Careful examination of Fig. 32 also shows that the slip lines go through the particles and a dark field electron micrograph (Fig. 30) clearly shows the resulting offsets. That particles can be drastically altered in shape is shown by an electron micrograph of a replica taken from the surface (Fig. 33) and clearly shows the distortion

of particles by a slip band.

To summarise this section - it appears that the two controlling factors which decide the type of deformation are ease of nucleation of slip and the formation of pile-ups. In mode A initiation of slip is easy and occurs over the whole crystal. Pile-ups are not observed because the low volume fraction of  $\gamma'$  allows cross-slip and bowing around obstacles. The constraint on the specimen is accommodated by nucleation of slip on many slip planes. For mode B slip is a little more difficult to nucleate but occurs over the whole crystal. However, there is some concentration in the region which forms slip bands so that pile-ups of dislocations occur. How these pile-ups occur is not clear but each pile-up must be of one sign and pile-ups of one sign predominate at opposite ends of the slip plane i.e. on opposite sides of the Frank-Read sources. One way pile-ups are believed to occur is by a group of dislocations being held up by a dislocation pile-up of the same sign on an adjacent slip plane. Double cross slip of screw components could give rise to Frank-Read sources on adjacent planes. This implies that cross-slip can occur but not easily enough to overcome all barriers as in the case of mode A. Once pile-ups have been formed the co-operative movement follows since it is postulated that pile-ups of like sign predominate on opposite sides of sources. From this it follows that the orientation across each kink band is about the same.

With mode C we find that dislocation nucleation is difficult, possibly for the following reason: when a Frank-Read source operates it sweeps out an area on the slip plane while forming the dislocation loop.

With a high volume fraction alloy the dislocation of the source will encounter a particle which it must cut to continue operating. If the Frank-Read source operates with one matrix dislocation, [precipitated  $\gamma'$  particles will not normally be threaded by grown-in dislocations] APB must be formed in the particle. This fact would tend to restrict the operation of sources. Once the first dislocation loop is complete the next will spread easily because the APB aids particle cutting. Source operation will become progressively easier as particles are sheared on the slip plane and it is believed that avalanches occur on a few slip planes to give the load drops. Work hardening however is high in this alloy and quickly stops these sources from operating so that the stress rises until new sources are operated. The new sources tend to operate on adjacent planes because of the stress concentration effects of work hardened planes. We emphasise that source operation does not occur within coherent particles formed on ageing because they are perfect crystals. Hence yield criteria for intermediate volume fractions must involve cutting of the particles by single, rather than double, dislocations.

Kinking does not occur in mode C because dislocation pile-ups do not occur as shown by Fig. 29. Instead dislocation tangles develop, possibly because cross slip of screw segments in  $\gamma'$  particles causes the dislocation line to become sessile. Cross-slipping is easier in large  $\gamma'$  particles, since it is easier for a segment of a superdislocation to constrict and cross-slip similar to the way a dissociated unit dislocation cross-slips.

## 6.2 Crystals Containing Large $\gamma'$ Particles ( $\sim 1\mu$ )

Slow cooling from 1300 to 700°C in 3 hours produced large coherent particles of  $\gamma'$  (Figs. 34, 35 and 36) with concave interfaces which show strain contrast. Since the particles are thicker than the foil the latter is probably due to relaxation of the particles normal to the surface resulting in lattice bending at the vertical particle/matrix interface. The shape of the particles has been discussed by Westbrook<sup>(2)</sup> and Papapetrou<sup>(3)</sup> who argue that increased "activity" at the corner sites results in accelerated growth. However, there is no reason why the "activity" should be greater at the corners than at any other place. More likely it is a geometrical effect in that at a corner site there is a greater diffusion flux to it than to a site away from the corner, so that growth is faster at the corner.

The reason for the clustering is still not clear. It may be the result of a random distribution such that  $\gamma$  particles are favourably placed to grow in this manner. When their faces approach each other growth stops on those faces but continues on the other outward facing faces.

It was shown that the particles become semi-coherent by ageing at 700°C for 4 weeks, dislocation networks forming at the interfaces (Figs. 45 and 46). It is believed these networks are the same as those found in the crystal when it is step cooled and will be discussed in Chapter VII. The 'precipitate' in the  $\gamma'$  particles is thought to be  $\gamma$  phase forming to give the equilibrium amounts of both phases according to the lever rule. Why excess  $\gamma'$  has formed and why  $\gamma$  should then

precipitate in the  $\gamma'$  is not clear.

Compression tests on the slow cooled crystals show that the C.R.S.S. is lower than for the aged crystals containing small particles-- except for the 18<sup>a</sup>/o Al crystal which contained incoherent particles. Only the 17<sup>a</sup>/o Al alloy was tested beyond the yield point and found to have a high rate of work hardening. Sections of this crystal studied in the electron microscope showed several features of interest. Fig. 38 shows the microstructure after 5% compressive strain and the presence of dislocations at the interface (Area A) shows that coherency has broken down in some particles. The presence of strain contrast (Area B) shows that not all interfaces have broken down (as might be expected from the inhomogeneity of the deformation). Fig. 39 shows that intersecting slip planes meeting at the interface of a particle are restricted from further movement, at least at this amount of strain. The behaviour of slip dislocations on the slip plane is shown by electron micrographs from a (111) section (Figs. 43 and 44). These micrographs show three features of interest. Firstly, pile-ups of dislocations at the interface (Area A in Fig. 43), secondly constriction of two matrix dislocations to form a superdislocation on entering a  $\gamma'$  particle (Area B in Fig. 43) and thirdly the shearing of a  $\gamma'$  particle by a large number of dislocations (Fig. 44). These observations will now be discussed in relation to the mechanical properties.

The pile-ups of dislocation and the cutting of particles suggest that there is some critical stress at which particles can be cut which is higher than the yield stress. At the same time the yield stress is lower than for aged alloys because bowing can occur between the large particles

at this lower stress. If  $\tau = Gb/\lambda$  and  $\tau = 25,400$  psi  $G = 7.5 \times 10^{10}$  dynes/cm<sup>2</sup>,  $b = 2.5\text{\AA}$  then  $\lambda \sim 1000\text{\AA}$ . It is difficult to estimate the spacing between these particles on the slip plane (Fig. 35) but it appears to be of this order. The pile-ups of dislocations would account for the initial high rate of work hardening observed and as more and more particles are cut at the increasing stress it is expected that the rate of work hardening would decrease. This is exactly the kind of behaviour Jones and Kelly<sup>(78)</sup> observed in a Cu-Be alloy which contained particles of intermetallic CuBe. They accounted for their results in the same way.

The observation of superdislocations in the  $\gamma'$  particles and the fact that the two unit dislocations of the pair can be resolved leads to an estimate of the APB energy. Following Brown and Herman<sup>(79)</sup> who first estimated the ordering energy in b.c.c. structures from dislocation spacing we find that

$$\gamma = \frac{1}{r} \frac{Gb^2}{2\pi} \left[ \cos^2\theta + \frac{\sin^2\theta}{1-\nu} \right]$$

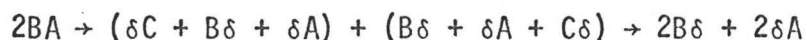
where  $\gamma$  is the APB energy,  $r$  the dislocation spacing, and  $\theta$  the angle between the Burgers vector and dislocation line (ignoring any dissociation into partials). From the micrograph (Fig. 43)  $\tau = 168\text{\AA}$ , so for a screw dislocation ( $\theta = 0^\circ$ )  $\gamma = 70$  ergs/cm<sup>2</sup> and for an edge dislocation ( $\theta = 90^\circ$ )  $\gamma = 105$  ergs/cm<sup>2</sup>. The APB energy has been given by Marcinkowski et al<sup>(80)</sup> as

$$\gamma = \frac{1.41 kT_c S^2}{a_0^2}$$

where  $T_c$  is the ordering temperature (taken as the melting point)  $S =$  L.R.O. parameter, and  $a_0$  is the lattice parameter, so that if we take  $\gamma$  as  $105 \text{ ergs/cm}^2$  then  $S = .645$ . Although because of the assumptions involved in deriving the equations the estimate for  $S$  is only approximate it does show that the particles are not fully ordered. In fact the individual dislocations in superdislocations in pure  $\text{Ni}_3\text{Al}$  are not usually resolved in the electron microscope because of the high ordering energy. Thus there is no doubt that the above observation of unit dislocations in  $\gamma'$  particles indicates a low APB energy and thus a low degree of order. Since the tendency to order in this system is very strong the reason for this low degree of order is not clear. One possibility is that the composition is away from equilibrium. This might be accounted for by removing the restriction that atomic species are added to the particle in a ratio dictated by stoichiometry i.e. 3 Ni atoms to 1 Al atom. The addition of atoms would then be controlled by the relative diffusion rates in the matrix. This would also account for the formation of  $\gamma$  within the  $\gamma'$ .

The electron micrograph in Fig. 38 shows the presence of stacking faults in the  $\gamma'$  particles; a situation which has only recently been accounted for<sup>(63,64)</sup>. As is well known the dissociation of a unit  $a/2 \langle 110 \rangle$  dislocation into two partials of the type  $a/6 \langle 112 \rangle$  leaves a stacking fault of high energy between them and similarly a superdislocation dissociated into two unit dislocations leaves a high energy boundary between. It was shown by Carnahan et al<sup>(63)</sup> that a stacking fault without APB is obtained by removing a layer of (111) plane i.e. no violation of

nearest neighbours. Kear<sup>(64)</sup> has shown that this can be achieved by superdislocation which effectively forms partials of the type  $2B\delta$  and  $2\delta A$  by the reaction



This reaction is more easily visualised by referring to Figs. 81 and 82 which show the sequence of steps in this model by using coloured balls stacked in layers representing (111) planes. Fig. 81(a) shows the normal stacking sequence on (111) planes and Fig. 81(b) the situation when a unit  $a/2$  [110] dislocation has passed across the slip plane. Violation of nearest neighbour bonding is evident i.e., red balls representing aluminum atoms are nearest neighbours. However, when we apply a  $2B\delta$  shear, that is an  $a/3$  [112] dislocation, a stacking fault without APB is produced (Fig. 82(a)). The trailing partial  $2\delta A = a/3$  [121] restores the lattice to its original stacking sequence (Fig. 82(b)).

The above model requires partial dislocations of the type  $a/3$   $\langle 112 \rangle$  which have so far not been reported in pure  $Ni_3Al$  structures. Enami and Nenno<sup>(62)</sup> have observed stacking faults in deformed  $Ni_3Al$  but were not able to identify the bounding partials. The stacking faults and the bounding partial dislocations observed in this work have been analysed. Fig. 41 is a foil from a (100) section after cold rolling and shows the contrast at the stacking fault for three different operating reflections. The analysis is detailed in Table IV and shows that the Burgers vectors of the partials are of the type  $a/3$   $\langle 112 \rangle$  and the stacking fault lies on the (111) plane. The dark field micrograph of the stacking fault with the  $\bar{g}$  vector pointing towards the bright fringe indicates that the stacking

fault is intrinsic<sup>(69)</sup> (Fig. 42). Thus there is good evidence for the correctness of the model proposed by Kear<sup>(64)</sup>.

It remains now to account for the existence of these partials since as seen earlier (Fig. 43), superdislocations in the form of two unit dislocations are found in  $\gamma'$  particles. In the examination of the electron micrographs two features became apparent regarding the dislocations inside  $\gamma'$  particles. Firstly stacking faults have not been found in fully coherent  $\gamma'$  particles and secondly superdislocations are nearly always associated with coherent particles. The implication is that a barrier at the interface, that is, interface dislocations, are necessary for the formation of stacking faults. Thus it is suggested that slip dislocations bow between the obstacles at the interface since it requires a lower stress for  $a/3 \langle 112 \rangle$  dislocations to do this than unit  $a/2 \langle 110 \rangle$  dislocations. Since  $a/2 \langle 110 \rangle = 2.5\text{\AA}$  and  $a/3 \langle 112 \rangle = 1.8\text{\AA}$  ( $a = 3.564\text{\AA}$  for  $\gamma'$ ) then the bowing stress  $\sim Gb/\lambda$ , where  $\lambda$  is the spacing of the obstacle, is about 30% smaller for an  $a/3 \langle 112 \rangle$  dislocation than for a  $a/2 \langle 110 \rangle$  dislocation.

Evidence for this  $a/3 \langle 112 \rangle$  partial dislocation and its associated stacking fault has been obtained recently during creep of a Ni-based superalloy by Kear et al<sup>(61)</sup>. Furthermore the intrinsic stacking fault of the kind found in this work is coupled to an extrinsic stacking fault giving a net Burgers vector of  $a \langle 112 \rangle$ . Kear et al believe that these intrinsic-extrinsic stacking fault pairs have their origin in the reaction of two unit dislocations on adjacent planes with their Burgers vectors at  $60^\circ$ . This was first proposed by Hirth<sup>(81)</sup> for the f.c.c. lattice. This complex pair do not however move by the ordinary glide

process but by viscous slip<sup>(61)</sup>, a type of motion ~~is~~ only possible at the temperatures employed in creep tests. Thus the existence of intrinsic-extrinsic stacking fault pairs in room temperature deformation of alloys containing  $\gamma'$  seems unlikely.

In summary it has been shown that large coherent cube-shaped particles  $\sim 1\mu$  in size, much larger than those formed by ageing at a fixed temperature, can be formed by slow cooling. The influence of these particles on deformation behaviour have been rationalised on the basis of electron microscope evidence. It was shown that the particles could become semi-coherent either by ageing or by cold working. An important dislocation-particle reaction was observed relating to the formation of stacking faults in particles. These faults were analysed and reasons for their formation suggested.

## CHAPTER VII

### SINGLE CRYSTALS WITH LARGE INCOHERENT $\gamma'$ PARTICLES

It has been shown by Cahn<sup>(24)</sup> that a coherent particle in a two-phase alloy is always more soluble than an incoherent one. The implication of this result is that an incoherent particle is the stable phase and will grow at the expense of a coherent one. Thus in the system Ni-Al one expects the  $\gamma'$  second phase particles to be incoherent subject to the energy criterion of Brown et al<sup>(29)</sup>. This is that the reduction in energy due to a dislocation loop at the interface is less than the self energy of the dislocation due to its line tension. This occurs at a particle diameter for  $\gamma'$  of  $240\text{\AA}$  in the Ni-Al system although as shown in Chapter VI this value is reduced by the APB produced by a single loop. Much bigger particles than this have been observed in Ni-Al alloys but no observations of interfacial dislocations have been reported although they have been seen in very similar systems e.g. Ni-Cr-Al-Ti<sup>(26)</sup>. However, using the heat treatment adopted in this work incoherent  $\gamma'$  particles with interfacial dislocation networks have been observed and analysed.

The basic requirement of a hexagonal network is that at the nodes  $\sum b_i = 0$ . Furthermore for the most efficient relief of misfit the dislocations should be pure edge and for particles with spherical shape there should be Burgers vectors in three orthogonal directions. It is believed that the Burgers vectors of these dislocations are all of the type  $a/2 \langle 110 \rangle$  and this conclusion has been reached after

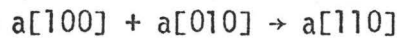
examining complete networks at three different particles. Fig. 49 shows a (001) section with a network covering a large area at A, the width of the network is about  $2.3\mu$ . We estimate the foil thickness to be  $1800\text{\AA}$  from the width of the stacking fault assumed to lie on a (111) plane. Hence the plane of the network at A is about  $4^\circ$  from the foil plane and hence must be a {001} plane. The network at B has a projected width of  $4700\text{\AA}$  and thus an angle of  $18^\circ$  to the foil surface. The trace of this area in the (001) foil plane is [100] and thus it should have indices of the type {okl}, i.e. (013).

A similar analysis for the networks shown in Fig. 50 suggests that they also lie on planes of the {okl} type. For the third network in Fig. 51 we have a foil close to (112) with a network width of  $4500\text{\AA}$ . If this network lies on a (111) plane then the calculated foil thickness is  $1600\text{\AA}$  which is a reasonable value. The trace of the network is [110] which is consistent with the analysis.

We thus have a situation in which a particle has to have a dislocation network which can fit several faces of different indices. The Burgers vector analysis presented in Table V shows that there are three dislocations in each network two of which are visible for each reflection and one invisible. The dislocations have been given Burgers vectors of  $a/2$  [10 $\bar{1}$ ],  $a/2$  [0 $\bar{1}$ 1] and  $a/2$  [ $\bar{1}$ 10] and it is seen that the requirement  $\sum b_i = 0$  is met. Thus the model comprises three mutually perpendicular dislocation loops of the above Burgers vectors which are wrapped round the particle and interact to give the observed dislocation networks. For instance the dislocations  $a/2$  [10 $\bar{1}$ ] and  $a/2$  [0 $\bar{1}$ 1] lying in the (001) plane would interact to give the third dislocation i.e

$a/2 [1\bar{1}0]$ .

There is a possibility that three  $a\langle 100 \rangle$  type dislocations could give rise to the networks seen. Thus on the (001) plane we could have the reaction,



and for  $\bar{g} = 200$ , the dislocation  $a[100]$  and  $a[110]$  would be visible and  $a[010]$  invisible. For  $\bar{g} = 020$ , the dislocations  $a[010]$  and  $a[110]$  would be visible and  $a[100]$  invisible. However difficulty arises when we try to fit the three  $a\langle 100 \rangle$  dislocations on the (111) plane with the restriction  $\sum b_i = 0$ . There does not seem any way that this can be achieved; furthermore all three dislocations of this type would be visible on the (111) plane and we have seen that this is not the case so we can rule out this possibility.

A feature of this model is that the Burgers vectors of the dislocations have mutually perpendicular components so that the displacements at the interface can be compensated for in all directions. This implies that the dislocations have mainly edge character (since it is only edge components which compensate for the displacements). The Burgers vector of each dislocation do not necessarily lie in each plane of the network. For example, the vectors  $a/2[10\bar{1}]$  and  $a/2[0\bar{1}1]$  do not lie in the (001) plane but they will have components in this plane. This feature necessarily restricts glide of the dislocations and climb must be invoked in order to build up the dislocation structure and also during growth of the particle. In view of the high temperatures used this should occur without difficulty.

The ideal way to accommodate the difference in lattice parameters at a (001) interface in the [010] direction is to have a series of parallel edge dislocations lying along the [100] direction with Burgers vector  $a[010]$ . With this model it is easy to calculate the spacing between dislocations to accommodate this misfit. If there are  $n$  unit cells of particle of lattice parameter  $3.566\text{\AA}$  there must be  $n+1$  unit cells of matrix of lattice parameter  $3.546\text{\AA}$  and

$$n \times 3.566 = (n+1) \times 3.546$$

Hence  $n = 177$  unit cells and the dislocation spacing is  $177n \times 3.566 = 632\text{\AA}$ . The spacing for  $a/2\langle 110 \rangle$  dislocations in the (111) plane would be  $177 \times 2.5\text{\AA} = 425\text{\AA}$ . Since these values are for pure edge dislocations, mixed dislocations can be expected to have smaller spacings. An estimate of the spacings observed shows that in the (111) plane the dislocation spacing in the  $\langle 110 \rangle$  is  $765\text{\AA}$  and in the (100) plane it is  $715\text{\AA}$ . These values are obviously greater than the expected value. One reason for this discrepancy lies in the possibility that the lattice parameters are not those measured by Phillips<sup>(6)</sup>. As Shewfelt<sup>(82)</sup> has shown a difference of  $0.01\text{\AA}$  in either of the lattice spacings would cause a change of 50% in the dislocation spacing.

The biggest single obstacle to a complete understanding of interfaces of this type lies in explaining the origin of the dislocations in the interfacial networks. Energetic treatments of the problem such as those of Brown et al<sup>(29)</sup> rarely seem to predict the size of particle at which interfacial dislocations appear. The best they can do is set a lower limit of particle size at which interfacial dislocations can appear.

Thus the problem would seem to be one of explaining nucleation of dislocations at the interface.

Weatherly and Nicholson<sup>(26)</sup> have made a study of the interfacial structures of semi-coherent precipitates in which one of the systems they examined was Ni-Cr-Ti-Al containing  $\gamma'$  particles. These  $\gamma'$  particles have the structure  $\text{Ni}_3(\text{Ti},\text{Al})$ , are spherical and have a misfit of 0.0028; this is about half the misfit in the Ni-Al system. After ageing at  $930^\circ\text{C}$  for 250 hours hexagonal dislocation networks were found at the interfaces of the  $\gamma'$  particles and analysed as  $a/2 \langle 110 \rangle$  dislocations which is consistent with the present results. They go on to show that the hexagonal networks can be considered to consist of segments from three dislocation loops there being a tendency for these to lie on  $\{110\}$  planes with the Burgers vector making an angle of about  $60^\circ$  to the plane of the loop. They point out that it is the edge components which provide relief of misfit but the energy of a hexagonal array of matrix dislocations is a minimum when all the dislocations are in screw orientation and the configuration adopted at an interface may be affected by this. They believe that the Burgers vectors of the dislocations are co-planar and therefore can only accommodate misfit in two directions. However there does not seem to be any reason why this should be so and in fact, three co-planar  $a/2 \langle 110 \rangle$  Burgers vectors can only lie in a  $(111)$  interface plane. It is suggested that the networks they found are similar to those described in this work. Thus the misfit at the interface in three directions can be accounted for.

Weatherly and Nicholson go on to discuss the mechanisms of loss of coherency as reviewed in Chapter II of this thesis. Because the

particles in their alloy did not have a misfit greater than the critical amount for the punching of dislocations (as calculated by Weatherly<sup>(27)</sup>) they believe that climb of matrix dislocations to the interface provided the source for dislocations. This case depends on the elastic interaction between particle and a matrix dislocation becoming attractive which is dictated by particle size (Brown et al<sup>(29)</sup>). They present electron microscope evidence to show the start of this climb process of dislocations to the particle interface.

The  $\gamma'$  particle in the Ni-Al system is like the system studied by Weatherly and Nicholson in that the misfit is less than the critical misfit for dislocation punching. The main difference in the observations in this work concerns the large number of dislocations seen at the interface which could not have been provided by the dislocation density in the matrix. There must have been a dislocation multiplication source operating to provide all the observed dislocations. It is conceivable that this could occur in two ways, firstly a source in the matrix and secondly, a source at the interface. The dislocation source in the matrix would operate only by climb while the one at the interface by both climb and glide since the Burgers vector of one segment lies in the network of the plane. The latter mechanism implies that once a dislocation is nucleated at the interface, presumably by climb, multiplication is relatively easy. Weatherly<sup>(27)</sup> has shown that the shear stress at the interface can be quite high, certainly much higher than the stress to move a dislocation so that this shear stress may aid dislocation multiplication.

At the high temperatures used in obtaining these dislocation networks the concentration of vacancies is going to be high. If there was a vacancy flow to the interface enough might collect to form the vacancy dislocation loop round the particle with the necessary missing half plane in the particle. However removing either a (100) or (110) plane would result in severe violation of the nearest neighbour bonding and is impossible. Removal of a (111) plane would leave a stacking fault (without APB) of low energy and should result in the usual stacking fault fringes. Few of these however are seen in the particles and the Burgers vector is of the wrong kind i.e.  $\frac{1}{3} a\langle 111 \rangle$ .

Another way to use the vacancies would be in the formation of loops inside the particles by the collapse of aggregates followed by growth to the loops to the interface. This was in fact the way in which Weatherly and Nicholson explained the formation of dislocations at the interface of  $\theta'$  particles in Cu-Al. There is evidence in the electron micrographs for the presence of loops in the  $\gamma'$  particles for example Fig. 48. However the model suffers from the objections raised above and the only possible dislocation loop would be one lying on the (111) plane i.e. a Frank sessile dislocation. This would be consistent with the trace of the loops in the (100) foil plane being  $[110]$  which is observed with many of the loops in the particles. Stacking fault contrast is also observed in some of the loops; this of course depends on the operating reflection. A Frank loop can move in two ways, either by climb or combination with a perfect dislocation to give a Shockley partial which can then glide (and vice versa). However the latter mechanism is unlikely

since the nucleation of a perfect dislocation would have to be accounted for, and furthermore, glide of a Shockley partial would give rise to a stacking fault. The climb of a Frank loop to the interface would leave a dislocation of Burgers vector  $1/3 \langle 111 \rangle$  which is not observed.

We thus have several alternatives to explain the nucleation of dislocations at the interface - none of which is entirely satisfactory and, some of which can be ruled out. The best alternative seems to be the climb of dislocations from sources in the matrix. In passing it is worth noting that the matrix has a fairly high dislocation density in some areas which may come from the climb sources. Alternatively, there is always the possibility of damage being introduced during preparation.

Several areas of the foil contained coherent  $\gamma'$  particles as shown by the strain contrast at the small particles in Fig. 55. This electron micrograph also shows the interaction of matrix dislocations with the particles and provides evidence in support of the climb mechanism. The presence of these coherent particles indicates that the alloy has not yet reached equilibrium i.e. incoherent solubility, and we would expect these particles to dissolve and the solute be absorbed by the large incoherent particles.

In summary we postulate the growth of  $\gamma'$  particles as cubes under equilibrium conditions or near equilibrium conditions to a size at which they become incoherent by attracting dislocations to their interfaces. Those particles which become incoherent grow at the expense of coherent ones and because of the continual supersaturation involved with

slow cooling. Growth of incoherent interfaces does not have the same restriction of accommodating elastic coherency strain which is most easily done on the {100} planes. The particle shape is controlled by the interfacial free energy which, from the evidence of faceting, shows some anisotropy. As the particles grow the dislocation network must provide new dislocations to take up the new displacement.

That there is a volume fraction effect in forming incoherent particles is seen by the fact that the 13<sup>a</sup>/o Al crystal contained only coherent particles after the step cooling heat treatment (Fig. 56). The maximum stress at the interface of an isotropic particle is a function only of the misfit and elastic moduli and not of the particle size<sup>(27)</sup>. The fact that there is a particle size dependence would seem to rule out a punching mechanism. The Brown et al<sup>(29)</sup> criterion is also met by particles in both alloys so it is not clear how this dependence operates. It may be statistical in that for the 17<sup>a</sup>/o Al alloy there is a greater volume fraction and hence more chance of a matrix dislocation being close to a particle. Weatherly and Nicholson<sup>(26)</sup> have in fact seen the beginning of coherency breakdown where some particles have dislocation at their interfaces while others of a comparable size do not. Furthermore, the precipitation of  $\gamma'$  in the 13<sup>a</sup>/o Al does not begin until about 850°C where climb is much more sluggish than at 1150°C where precipitation begins in the 17<sup>a</sup>/o Al. Any model also has to take into account the breakdown of coherency in the 17<sup>a</sup>/o Al aged at 700°C after a slow cool from 1300 to 700°C in 3 hours. What is certain is that the total strain energy of a particle increases with its volume but it is not easy to see how this affects the attraction of dislocation to the interface. Further work is

needed to see at what size of particle coherency breaks down during the cooling treatment.

The last part of this chapter will be concerned with the mechanical properties of alloys in this condition. The alloys are characterised by a high rate of work hardening and for the 18<sup>a</sup>/o Al crystal a 0.2% yield stress is greater than that obtained by solution treatment and ageing (Table III). The shear stress-shear strain curve for the 18<sup>a</sup>/o Al crystal is shown in Fig. 52. Jones and Kelly<sup>(78)</sup> have observed a similar kind of stress-strain behaviour in an overaged alloy of Cu-1.8<sup>w</sup>/o Be single crystals. Their initial rates of work hardening were very high and decreased with increasing strain. They concluded that the precipitate, intermetallic CuBe, was not being cut in the initial stages of deformation, so that the alloy was behaving like a hard particle dispersion strengthened metal. Eventually the applied stress reached the shear stress of the particles and cutting occurred giving a lower rate of work hardening. This model seems applicable to the 18<sup>a</sup>/o Al crystal which exhibited a similar stress-strain behaviour. In this case the obstacle to cutting of the particles is the dislocation network at the interface. It is expected that cutting of the particles will occur eventually as the work hardening rate decreases with increasing strain in a similar way to Jones and Kelly's result for Cu-Be. However, in this case the cutting may be a result of slip dislocations bowing between the segments of hexagonal networks either as superdislocations or more likely as the super partials described in Chapter VI. The spacing of dislocations in the network is about 700<sup>o</sup> and if  $\tau = Gb/e$  where  $G = 7.5 \times 10^{10}$  dynes/cm<sup>2</sup>, (37), then

$\tau = 37,500$  psi which is of the right order.

The C.R.S.S. for this alloy as step cooled is 39,000 psi compared to a value of 29,000 psi for the aged alloy containing small particles. This is a significant increase and must be accounted for in some way by the bowing mechanism. The size and dispersion of the particles in some way have a geometry which requires higher stresses for dislocation bowing than a uniform dispersion of much smaller particles. A 16<sup>a</sup>/o Al crystal in the same condition did not have as high a C.R.S.S. as in the aged condition. This suggests that bowing is easier than in the 18<sup>a</sup>/o Al crystal because the interparticle spacings are probably larger. Examination of the surface by optical microscopy did not reveal any slip lines. This is consistent with the behaviour of hard particle dispersion strengthened alloys. No electron microscopy was done on the 18<sup>a</sup>/o Al crystal in the step cooled condition. (Jones and Kelly in their examination of the deformed Cu-Be alloy could make no distinction between structures with high and low rates of work hardening.)

## CHAPTER VIII

### THE DEFORMATION OF POLYCRYSTALS

#### 8.1 Introduction

The object of the work discussed in this chapter was basically to find out how the mechanical properties of polycrystalline Ni-Al were affected by composition and how they were affected by ageing time. As described in Chapter III the approach was to use compression samples to investigate the composition aspect and tensile strip samples to study the ageing time effect. The results have been detailed in Chapter IV and what are considered to be the most pertinent results are discussed in the following.

#### 8.2 The Effect of Composition

Compositional effects were studied merely by changing the amount of aluminum in the alloy from 12<sup>a</sup>/o to 25<sup>a</sup>/o. By reference to Fig. 1, it is seen that this changes the equilibrium proportion of phases present (at 700<sup>o</sup>C) from 0 to 100% $\gamma'$ , the precipitating phase. Again referring to Fig. 1 it is clear that above 21<sup>a</sup>/o Al all the  $\gamma'$  cannot precipitate from solid solution; some forms directly from the liquid. Thus any conclusions drawn concerning these alloys must be done so with this fact in mind.

In this section an attempt will be made to account for the following features in the results:

- i) the shape of the compressive strength versus volume fraction  $\gamma'$  curve and the peak strength at  $0.45\gamma'$ .
- ii) the increasing rate of work hardening with increasing amount of  $\gamma'$ .
- iii) the decreasing ductility with increasing volume fraction  $\gamma'$ .

The results of compression and tensile tests are described by Figs. 57, 58, 59, 70, 71 and 72. It will be noticed that there is a difference in the actual values of the peak strengths and the ageing times at which these occur for the two tests. It is believed that the difference in peak strengths is accounted for by the difference in grain sizes; if  $k_y$  in the Petch equation is taken as  $2 \text{ kg/mm}^2$  then the grain size difference accounts for about 5,000 psi which is close to the difference in peak strengths. Since the rate of quenching in a specimen is determined by its thickness, the compression specimens will obviously have a lower quenching rate than the tensile strip specimens. From the discussion in Chapter V it follows that decomposition will be further advanced in the compression specimens thus the structure which gives peak strength will be reached sooner in these specimens.

The most important aspect of these results concerns the peak strength coinciding with a volume fraction of  $\gamma'$  of 0.45. Most theories used so far in describing the mechanism of strengthening in alloys of this kind have not been successful in predicting the volume fraction at which peak strength occurs. However, in this particular case the peak strength may not be governed by dislocation-particle interactions but by

the effect of grain boundaries. There is evidence to show that for alloys with  $0.45\gamma'$  and greater, grain boundary sliding occurs. Fig. 65 shows the relative movement of a scratch on the two sides of a grain boundary in the  $0.45\gamma'$  alloy and Fig. 63 for a 17% Al alloy shows grain boundary cracks. All the compression samples with  $0.45\gamma'$  and greater showed grain boundary cracks and it is believed that they were caused by grain boundary sliding which started at the yield point. This kind of cracking is sometimes known as triple point cracking because it is initiated at the point of intersection of three grains. A further important piece of evidence comes from the compression tests on single crystals. Over the range of compositions used the strongest crystal was the one containing most  $\gamma'$ , the 18% Al crystal with  $0.55\gamma'$ . From this evidence it is probable that the fall in strength above  $0.45\gamma'$  is caused by grain boundary sliding and not some dislocation-particle interaction on the slip plane. As pointed out in Chapter VI the yield strength of high volume fraction single crystals may depend on the bowing of single dislocation sources which are forced to cut closely spaced particles thus creating an APB. For polycrystalline alloys it is possible that grain boundaries provide superdislocations and obviate the necessity for Frank-Read type sources.

In precipitation hardened alloys grain boundary cracking is sometimes due to precipitate-free zones on each side of grain boundaries. These regions are thought to slip profusely, work harden and cause cracks. However, in this alloy there is no evidence of these zones. It is believed that because the matrix becomes stronger with the increasing amount of  $\gamma'$

the yield strength of the alloy eventually reaches the shear strength of the grain boundary so that sliding occurs at the boundary. Sliding along two boundaries which meet at a third can result in crack formation at the third boundary - the so called triple point cracking. This sliding could be accommodated by several slip systems operating close to boundary (5 are necessary to accommodate changes in grain shape) but there is no evidence for this in the high volume fraction alloys. On the other hand the low volume fraction alloys accommodate shape change easily; Fig. 64 shows profuse slip near grain boundaries in the 14<sup>a</sup>/o Al alloy.

Slip lines are seen in the high volume fraction alloys indicating that the yield stress of the grains has been exceeded. This could occur by stress concentrations resulting from grain boundary sliding. The mechanism of grain boundary sliding is not well understood but it is believed to be due to grain boundary dislocations, (at least at room temperature), which probably have different Burgers vectors than matrix dislocations. However, it is not unlikely that they could act as sources for slip in the matrix.

Although this model can show why the yield stress reaches a maximum in the polycrystals before the single crystals it does not account for the fact that the strength begins to fall off as the volume fraction is increased beyond 0.45 $\gamma$ . Thus grain boundary sliding occurs at lower stresses as the amount of  $\gamma'$  increases. It is not clear at present how the model of grain boundary sliding can account for this observation. However, it should be noted that the yield stress of alloys containing  $\gamma'$  grown from the melt will be lower than the peak

strength. The reason for this is that it is expected that  $\gamma'$  grown from the melt will contain grown-in dislocation (possibly superdislocations) whereas  $\gamma'$  particles nucleated from solid solution do not. Since it is known that the yield stress of pure  $\text{Ni}_3\text{Al}$  is low (~11,000 psi) dislocation multiplication will occur at a lower stress and hence the yield stress will be lower as the alloys are mainly  $\gamma'$ . Fig. 62 shows slip lines in an alloy containing massive  $\gamma'$  (i.e. grown from the melt), which appear to have common slip planes in matrix and particle. It is possible that the dislocations giving rise to the slip lines originate in the  $\gamma'$  particles.

The initial increase in strength with volume fraction is rapid followed by a slower rate of increase up to the peak strength. This behaviour is in distinction to that for single crystals where the increase appears to be linear over the range studied (Fig. 83). This emphasizes the need for caution in using polycrystalline data to fit theories for the strength of alloys since it is the critical resolved shear strength which is calculated. Mechanisms describing the strength increase use paired dislocations in this problem, the distance between pairs being a function of particle size and distribution. Qualitatively this can explain the strength increase with volume fraction  $\gamma'$  in the same way the strength of single phase ordered alloys as a function of order is explained. At low volume fractions paired dislocations are widely separated because the amount of APB being generated is small. As the volume fraction of  $\gamma'$  increases the increased size of the particles restricts the first dislocation so that the second one presses closer.

At the same time the amount of APB being formed as the first dislocation cuts the particle, is larger and thus the stress required for slip increases. As the second dislocation presses closer to the first one it exerts a repulsive force which adds to the applied stress and tends to decrease the yield stress. Thus there will eventually be a balance when the repulsive force increase with volume fraction equals the resistance force due to the formation of APB. It would be expected that the dislocation would be in the same particle when this occurs. Fig. 12 for the 14<sup>a</sup>/o Al crystal shows the dislocation pairs more widely spaced than for the 17<sup>a</sup>/o Al in Fig. 30 as is expected. A fall off in strength occurs when the repulsive force effect becomes greater than that due to the APB. This is effectively very similar to Gleiter and Hornbogen's<sup>(42)</sup> approach.

The work hardening increases with increasing volume fraction and becomes very high with high volume fractions (Fig. 58). Following the idea of Chapter VI regarding the effect of cross-slip in  $\gamma'$  particles, the greater the volume fraction  $\gamma'$  the greater the chance of cross-slip. Since current theories of work hardening in  $L1_2$  alloys successfully use the cross-slip mechanism it seems appropriate to invoke it here. Cross-slip tends to produce a sessile dislocation since the ends of the cross-slipping segment are effectively pinned at the  $\gamma/\gamma'$  interface. The work hardening rate will then increase with volume fraction of  $\gamma'$ . There is some evidence that cross-slip around particles is easy in low volume fraction alloys as shown by the slip lines on the surface of the 14<sup>a</sup>/o Al alloy (Fig. 60) which cross from one slip line to another in one area.

Slip markings of this kind were not observed on any of the higher volume fraction alloys.

It is possible that in the very high volume fraction alloys the particles are incoherent which the single crystal work has shown to result in a high rate of work hardening. Fig. 69 (21<sup>a</sup>/o Al) shows irregular particle shapes as seen in the single crystal incoherent alloy while Fig. 67 and 68 (17<sup>a</sup>/o and 20<sup>a</sup>/o Al respectively) show more regular shapes characteristic of coherent alloys.

The ductility of tensile samples decreased with increasing volume fraction as shown in Fig. 72. Since slip is profuse in grain boundary regions rapid work hardening will occur in these regions. As the work hardening rate is a function of volume fraction the work hardening will be greater for alloys with a higher volume fraction. The fracture stress is thus reached sooner as the volume fraction increases. This model is very similar to that for precipitate free zones as outlined by Kelly and Nicholson.<sup>(1)</sup> In this case however, there is some deformation in the grains and hence some elongation.

### 8.3 The Effect of Ageing Time

On ageing solution treated alloys there is an initial rapid rise in strength, followed by a slower rise to peak strength, then overaging. Fig. 71 shows that for tensile strip samples this occurs after 6 hours at 700°C. Theories of strengthening try to account for this behaviour in terms of particle-dislocation interaction which depend on size and dispersion of particle, it being assumed that the volume fraction remains constant.

From the discussion in Chapter V we believe that there is an increase in volume fraction of the precipitating phase but it is small and insufficient to account for the magnitude of the strength increase.

Gleiter and Hornbogen<sup>(42)</sup> have taken account of the possibility that L.R.O. in the particles increases with ageing time and believe that it can cause a strength increase. However, they did not directly measure the magnitude of the effect. Brown and Ham<sup>(29)</sup> derive an equation which shows that the increase in strength due to coherent ordered particles is directly proportional to the APB energy. Since APB energy depends on the L.R.O. in the particles this latter parameter is very important.

The results of measurements of L.R.O. shows that it increases with ageing time. Since the L.R.O. determines the intensity of superlattice lines obtained by diffracting an X-ray beam the intensity of a 100 line was measured as a function of ageing time for a 16<sup>a</sup>/o Al single crystal. The results which are given in Fig. 75 show how the intensity of the 100 line increases with ageing time (rapidly at first, and more slowly thereafter). The intensity at very long ageing times was not established. The increase in the APB energy, which is directly proportional to the intensity of the 100 line, is greater than the increase in strength. For example the strength increases by a factor of about 1/3 between 1 hour and 6 hours while the superlattice intensity increases 3 times. Thus it seems that while the major part of the increase in strength can be attributed to an increase in APB energy through the L.R.O. parameter, there is also a mechanism which contributes a decreasing part

to the strength. Following the discussion of the first section in this Chapter it is suggested that this occurs because the increasing APB energy causes the pair spacing to decrease so that the repulsion of the second dislocation on the leading dislocation aids the applied shear stress. Overageing occurs when this latter effect begins to predominate.

The results of this section show the difficulty of attempting to obtain values of the APB energy from measurements of particle size during initial stages of ageing. This Brown and Ham<sup>(29)</sup> do using published results in the literature and from the above results their method of obtaining the APB energy in this way is questionable.

To summarise this Chapter it has been shown that grain boundaries can have a pronounced effect on the mechanical properties of Ni-Al alloys. They change the relation between strength and volume fraction of  $\gamma'$  and induce embrittlement. The volume fraction of  $\gamma'$  affects the strength of the alloy, its influence being controlled by the ageing time. The most important result of the latter is the effect on L.R.O. which in turn affects strength through the APB energy. Current theories do not seem to be sufficiently well developed to predict the effect of volume fraction and ageing time.

## CHAPTER IX

### CONCLUSIONS

1. The volume fraction of  $\gamma'$  affects the C.R.S.S. of single crystals and determines their macroscopic deformation behaviour. The C.R.S.S. is almost linear from 0.1 to 0.55 volume fraction  $\gamma'$ .
2. The presence of stacking faults bounded by unusual partial dislocations ( $a/3 \langle 112 \rangle$ ) has been detected in large  $\gamma'$  particles. These large particles could affect the strength of the alloy by acting as barriers to dislocations, resulting in a high rate of work hardening. (The particles were eventually cut when a critical stress was reached.)
3. The coherent particles of  $1\mu$  in size became semi-incoherent either after prolonged ageing and on cold working.
4. Incoherent particles of  $\gamma'$  were formed by prolonged slow cooling from a high temperature. The dislocation networks at the interface were analysed to be of the type  $a/2 \langle 110 \rangle$ .
5. Both the strength and work hardening rates of alloys containing incoherent particles were high.
6. The strength of polycrystals increases with volume fraction  $\gamma'$  to a maximum at 0.45  $\gamma'$ , but not linearly as in single crystals. Grain boundaries appear to play an important role in the mechanical properties of these alloys. They cause the peak strength to occur at a lower volume fraction of  $\gamma'$  than for single crystals and cause embrittlement<sup>(15)</sup>.
7. The strength of polycrystals increases with ageing time to a maximum after 6 hours. The major source of this increase is due to an increase in the degree of order in  $\gamma'$  particles.

### Bibliography

1. A. Kelly and R. B. Nicholson, Prog. Mat. Sci. 10, No. 3 Pergamon Press 1963 .
2. J. H. Westbrook, Z. Krist. 110, 1, 1958.
3. A. Papapetrou, Z. Krist. 92, 89 1935.
4. R. O. Williams, Trans. Metall. Soc. AIME 215, 1026, 1959.
5. A J. Ardell and R. B. Nicholson, Acta Met. 14, 1295, 1966.
6. V. A. Phillips, Acta Met. 14, 1533, 1966.
7. A. J. Ardell, Phil. Mag. 16, 147, 1967.
8. J. M. Oblak and B. H. Kear, Trans. A.S.M. 61, 519, 1968.
9. J. Manenc, C. R. Acad. Sci. Paris 242, 2344, 1956.
10. J. Manenc, Revue Metall. 54, 687, 1957.
11. J. Manenc, Acta Met. 7, 124, 1959.
12. A. Guinier, Acta Met. 3, 510, 1955.
13. V. Daniel and H. Lipson, Proc. R. Soc. A181, 368, 1943.
14. Yu. A. Bagaryatskii and Yu. D. Tyapkin, Soviet Phys. Crystallogr. 2, 414, 1957.
15. Yu. A. Bagaryatskii and Yu. D. Tyapkin, ibid 5, 573, 1960-61.
16. G. C. Weatherly, private communication.
17. C. Wagner, Z. Elektrochem. 65, 581, 1961.
18. I. M. Lifshitz and V. V. Slyozov, J. Phys. Chem. Solids 19, 35, 1961.
19. R. A. Swalin and A. Martin, Trans. Am. Inst. Min. Metall. Engrs. 206, 567, 1956.
- \*20. R. A. Oriani, Acta Met. 12, 1399 (1964), and ibid 14, 84, 1966.
- \*21. A. J. Ardell and R. B. Nicholson, J. Phys. Chem. Solids, 27, 1793, 1966.
- \*22. A. R. Ardell, Acta Met. 16, 511, 1968.

23. A. Taylor and R. W. Floyd, *J. Inst. Metals* 81, 25, 1952.
24. J. W. Cahn, *Acta. Met.* 14, 83, 1966.
25. P. K. Rastogi and A. J. Ardell, *Acta Met.* 17, 595, 1969.
26. G. C. Weatherly and R. B. Nicholson, *Phil. Mag.*, 17, 801, 1968.
27. G. C. Weatherly, *Phil. Mag.*, 17, 791, 1968.
28. J. M. Silcock and T. J. Heal, *Acta Crystallogr.*, 9, 680, 1956.
29. L. M. Brown, G. R. Woolhouse and U. Valdrè, *Phil. Mag.*, 17, 781, 1968.
30. A. Kelly, *Strong Solids*, Oxford: Clarendon Press, 1966.
31. D. Turnbull, "Impurities and Imperfections", p.121, *Amer. Soc. Metals*, 1955.
32. C. Y. Li and R. A. Oriani, *Proc. Bolton Landing Conf. Oxide Dispersion Strengthening*, 1967.
33. N. F. Mott and F. R. N. Nabarro, *Proc. Phys. Soc.* 52, 86, 1940.
34. N. F. Mott and F. R. N. Nabarro, *Rep. Conf. Strength of Solids*, p1, *Physical Society*, 1940.
35. N. F. Mott, *J. Inst. Metals*, 72 367, 1946.
36. E. Orowan, *Symposium on Internal Stresses in Metals and Alloys*, p451, *Institute of Metals*, 1948.
37. V. Phillips, *Phil. Mag.*, 16, 103, 1967.
38. L. M. Brown and R. K. Ham, *Strengthening Mechanisms in Crystals*, ed. A. Kelly and R. B. Nicholson, to be published.
39. R. G. Davies and N. S. Stoloff, *Trans. Met. Soc. AIME*, 233, 714, 1965.
40. S. M. Copley and B. H. Kear, *Pratt and Whitney Aircraft*, Report 66-027.
41. J. L. Castagné, *J. de Physique (suppl)*, 27, 7-8, 233, 1966.
42. H. Gleiter and E. Hornbogen, *Phy. Stat. Solidi*, 12, 251, 1965.
43. E. Hornbogen and M. Mukherjee, *Z. Metall.*, 55, 293, 1964.
44. H. Gleiter and E. Hornbogen, *Phys. Stat. Solidi*, 12, 235, 1965.
45. H. Gleiter and E. Hornbogen, *Z. Metall.*, 58, 157, 1967.

46. P. Beardmore, R. G. Davies and T. L. Johnston, To be published.
47. B. Jaoul, J. Mech. Phys. Solids, 9, 69, 1961.
48. B. J. Piarcey and F. L. VerSnyder, Pratt and Whitney Aircraft, Rpt. 66-007.
49. R. J. Price and A. Kelly, Unpublished work, quoted in ref. 1.
50. E. Orowan, Nature, 149, 643, 1942.
51. F. C. Frank and A. N. Stroh, Proc. Phys. Soc. B65, 295, 1952.
52. J. B. Hess and C. S. Barrett, Trans. AIME, 185, 599, 1949.
53. R. W. Cahn, J. Inst. of Metals, 79 (3), 129, 1951.
54. N. K. Chen and C. H. Mattewson, Trans. AIME, 191, 653, 1951.
55. R. Maddin and N. K. Chen, Prog. Met. Phys. 5, 53, 1954.
56. P. B. Hirsch, Prog. Met. Phys. 6, 236, 1956.
57. A. H. Cottrell, Dislocations and Plastic Flow in Crystal, Clarendon Press, 1953.
58. M. Hatherly, J. Inst. Metals, 85, 437, 1956-57.
59. D. Kuhlmann-Wilsdorf and H. Wilsdorf, Acta Met. 1, 394, 1953.
60. Y. Calvayrac and M. Fayard, Acta Met., 14, 783, 1966.
61. B. H. Kear, G. R. Leverant and J. M. Oblak, To be published.
62. K. Enami and S. Nenno, J. Phys. Soc. Japan, 25, 1517, 1968.
63. T. Carnahan et al, Trans. Met. Soc. AIME, 239, 2014, 1967.
64. B. H. Kear, Proc. Intern. Conf. on the Strength of Metals and Alloys, Tokyo, 1967 (in press).
65. B. R. McDonnell et al, J. of Mat. Sci., 2, 365, 1967.
66. T. L. Alstruther and J. W. Christian, Phil. Trans. Roy. Soc. London, A261, 253, 1967.
67. A. J. Ardell, Phil. Mag., 16, 147, 1967.
68. J. M. Oblak and B. H. Kear, A.S.M. Trans., 61, 519, 1968.

69. P. B. Hirsch et al, *Electron Microscopy of Thin Crystals*, Butterworths, 1965.
70. R. Gevers, A. Art and S. Amelinckx, *Phys. Stat. Solidi*, 3, 1563, 1963.
71. T. Taoka, K. Yasukochi, and R. Honda, *Mech. Props. Inter. Compd.*, Wiley, 1960.
72. J. Friedel, *Les Dislocations*, Paris, 1956.
73. D. Gomersall, Ph.D. Thesis, McMaster University, 1967.
74. C. Zener, *J. App. Phys*, 20, 950, 1944.
75. G. R. Purdy, Private communication.
76. R. E. Hanneman and A. V. Seybolt, *Trans. Met. Soc. AIME*, 245, 434, 1969.
77. M. F. Ashby, Office of Naval Research, U.S.A., Tech. Report No. 515, 1966.
78. R. L. Jones and A. Kelly, *Acta. Met.*, 15, 656, 1967.
79. N. Brown and M. Herman, *Trans. AIME*, 206, 1353, 1956.
80. M. J. Marinkowski, N. Brown and R. M. Fisher, *Acta. Met.*, 9, 129, 1961.
81. J. P. Hirth, *J. Appl. Phys.*, 32, 700, 1961.
82. R. Shewfelt, M.Sc. Thesis, McMaster Univ., 1969.

TABLE I

Spectrographically pure nickel - Johnson Matthey

<u>Element</u>	<u>ppm</u>
Iron	7
Silicon	4
Aluminum	1
Magnesium	1
Calcium	<1
Copper	<1
Silver	<1

Spectrographically pure nickel - Materials Research Corporation

<u>Element</u>	<u>ppm</u>
Carbon	17
Oxygen	18
Nitrogen	3
Iron	12
Tin	<4
Chromium	1.5
Tungsten	1.5

Spectrographically pure aluminum - Johnson Matthey

<u>Element</u>	<u>ppm</u>
Magnesium	10
Iron	2
Copper	<1

TABLE II

Compositions of Alloys

<sup>a</sup> /o Al	W/o Al	W/o $\gamma'$ (700°C)	V/o $\gamma'$ (700°C)	Grain Size Compression Specimen, mm
12	5.9	0	0	0.51
12.5	6.16	4.2	4.55	0.57
13	6.43	8.55	9.25	0.65
13.5	6.69	12.74	13.7	0.7
14	6.96	17.1	18.4	0.67
14.5	7.23	21.4	22.85	0.85
15	7.5	25.8	27.5	0.59
15.5	7.77	30.1	31.9	1.0
16	8.05	34.7	36.7	0.74
16.5	8.31	38.8	40.8	0.74
17	8.6	43.5	45.5	0.59
17.5	8.88	48	50	0.78
18	9.16	52.5	54.6	0.59
19	9.73	62	64	0.61
20	10.3	71	72.5	0.74
21	10.88	80	81.4	0.41
22	11.47	90	90.8	0.44
25	13.29	100	100	0.23

TABLE IV

Analysis of Partial Dislocations Bounding Stacking Faults

Values of g.b and g.R

$\bar{g}$	Partial Dislocation 1 $b = \frac{a}{3} [2\bar{1}\bar{1}]$	Partial Dislocation 2 $b = \frac{a}{3} [1\bar{2}\bar{1}]$	Stacking Fault $R = \frac{a}{3} [111]$
020	-2/3 visible	-4/3 invisible	$\frac{2\pi}{3}$ visible
$\bar{1}\bar{3}1$	0 invisible	2 visible	$2\pi$ invisible
220	2 visible	2 visible	0 invisible

Criteria

For dislocations if  $g.b = 0, 1/3, 4/3$ , invisible

$g.b = 2/3, 1, 2$  visible

For stacking faults if  $g.R = 0, 1, 2$  invisible

all other values visible

TABLE II

Compositions of Alloys

<sup>a</sup> /o Al	W/o Al	W/o $\gamma'$ (700°C)	V/o $\gamma'$ (700°C)	Grain Size Compression Specimen, mm
12	5.9	0	0	0.51
12.5	6.16	4.2	4.55	0.57
13	6.43	8.55	9.25	0.65
13.5	6.69	12.74	13.7	0.7
14	6.96	17.1	18.4	0.67
14.5	7.23	21.4	22.85	0.85
15	7.5	25.8	27.5	0.59
15.5	7.77	30.1	31.9	1.0
16	8.05	34.7	36.7	0.74
16.5	8.31	38.8	40.8	0.74
17	8.6	43.5	45.5	0.59
17.5	8.88	48	50	0.78
18	9.16	52.5	54.6	0.59
19	9.73	62	64	0.61
20	10.3	71	72.5	0.74
21	10.88	80	81.4	0.41
22	11.47	90	90.8	0.44
25	13.29	100	100	0.23

TABLE VI

L.R.O. in Splat Cooled Ni<sub>3</sub>Al

hkl	Sinθ	$\frac{\text{Sin}\theta}{\lambda}$	f <sub>Ni</sub>	f <sub>Al</sub>	F  <sup>2</sup>	ρ	Lorentz Polarisation	Calculated Intensity
100	.217	.14	25.16	10.21	215	6	39.82	51.2 x 10 <sup>3</sup>
110	.306	.198	21.37	9.21	148	12	18.55	32.9 x 10 <sup>3</sup>
200	.434	.277	18.8	8.2	4180	6	8.184	206 x 10 <sup>3</sup>
220	.613	.398	15.34	6.8	2800	12	3.577	77.2 x 10 <sup>3</sup>

Calculated:  $\frac{I_{200}}{I_{100}} = 4$        $\frac{I_{220}}{I_{110}} = 2.35$

Splat cooled:  $\frac{I_{200}}{I_{100}} = 7.35$       S = .74

$\frac{I_{220}}{I_{110}} = 4.45$       S = .73

After 700°C  
3 hours :  $\frac{I_{200}}{I_{100}} = 5.75$       S = .84

$\frac{I_{220}}{I_{110}} = 2.53$       S = .96

TABLE V

Analysis of Burgers Vectors of Dislocations at Interfaces  
Of Incoherent Particles

	$\bar{g}$	<u>Visible</u>		<u>Invisible</u>	<u>Direction</u>	<u>Dislocation Spacing</u>
Fig. 47(a)	020	$a/2[0T1]$	$a/2[T10]$	$a/2[10T]$	[110]	715Å
Fig. 47(b)	200	$a/2[10T]$	$a/2[T10]$	$a/2[0T1]$		
Fig. 48(a)	020	$a/2[0T1]$	$a/2[T10]$	$a/2[10T]$		
Fig. 48(b)	200	$a/2[10T]$	$a/2[T10]$	$a/2[0T1]$		
Fig. 49(a)	T11	$a/2[0T1]$	$a/2[10T]$	$a/2[T10]$	[110]	765Å
Fig. 49(b)	T11	$a/2[T10]$	$a/2[10T]$	$a/2[0T1]$		

## Appendix B

Oriani's<sup>(20)</sup> equations (4) and (7) are as follows,

$$\begin{aligned}
 x_B^\beta \ln \frac{x_B^\beta x_B^{\alpha,i}}{x_B^{\beta,i} x_B^\alpha} + (1 - x_B^\beta) \ln \frac{(1 - x_B^\beta)(1 - x_B^{\alpha,i})}{(1 - x_B^{\beta,i})(1 - x_B^\alpha)} \\
 = - \frac{2 G_\alpha V_m^\beta (\Delta V/V_m^\alpha)^2}{RT (3 + 4 K_\beta G_\alpha)} \quad (4)
 \end{aligned}$$

$$\begin{aligned}
 \ln \frac{x_B^\beta (1 - x_B^{\beta,i}) x_B^{\alpha,i} (1 - x_B^\alpha)}{x_B^{\beta,i} (1 - x_B^\beta) x_B^\alpha (1 - x_B^{\alpha,i})} = - \frac{2 G_\alpha V_m^\beta (\Delta V/V_m^\alpha)^2}{(3 + 4 K_\beta G_\alpha) RT} \\
 \left\{ \frac{2[V_m^\alpha (\bar{V}_B^\beta - \bar{V}_A^\beta) - V_m^\beta (\bar{V}_B^\alpha - \bar{V}_A^\alpha)] + \frac{V_B^\beta - \bar{V}_A^\beta}{V_m^\beta}}{[V_m^\alpha]^2 (\Delta V/V_m^\alpha)} \right\} \quad (7)
 \end{aligned}$$

where  $\beta$  represents a coherent particle in matrix  $\alpha$  and

$V_m^\beta$  relaxed molal volume of phase  $\beta$

$V_m^\alpha$  relaxed molal volume of phase  $\alpha$

$\Delta V = V_m^\beta - V_m^\alpha$

$\bar{V}_A^\alpha, \bar{V}_A^\beta$  partial molar volume of atom A (Ni) in  $\alpha$  and  $\beta$  phases respectively.

$\bar{V}_B^\alpha, \bar{V}_B^\beta$  partial molar volume of atom B (H) in  $\alpha$  and  $\beta$  phases respectively.

$x$ 's are mole fractions and the superscript  $i$  refers to the incoherent equilibrium.

$G_{\infty}$  shear modulus of matrix

$K_{\beta}$  compressibility of particle

RT usual meaning

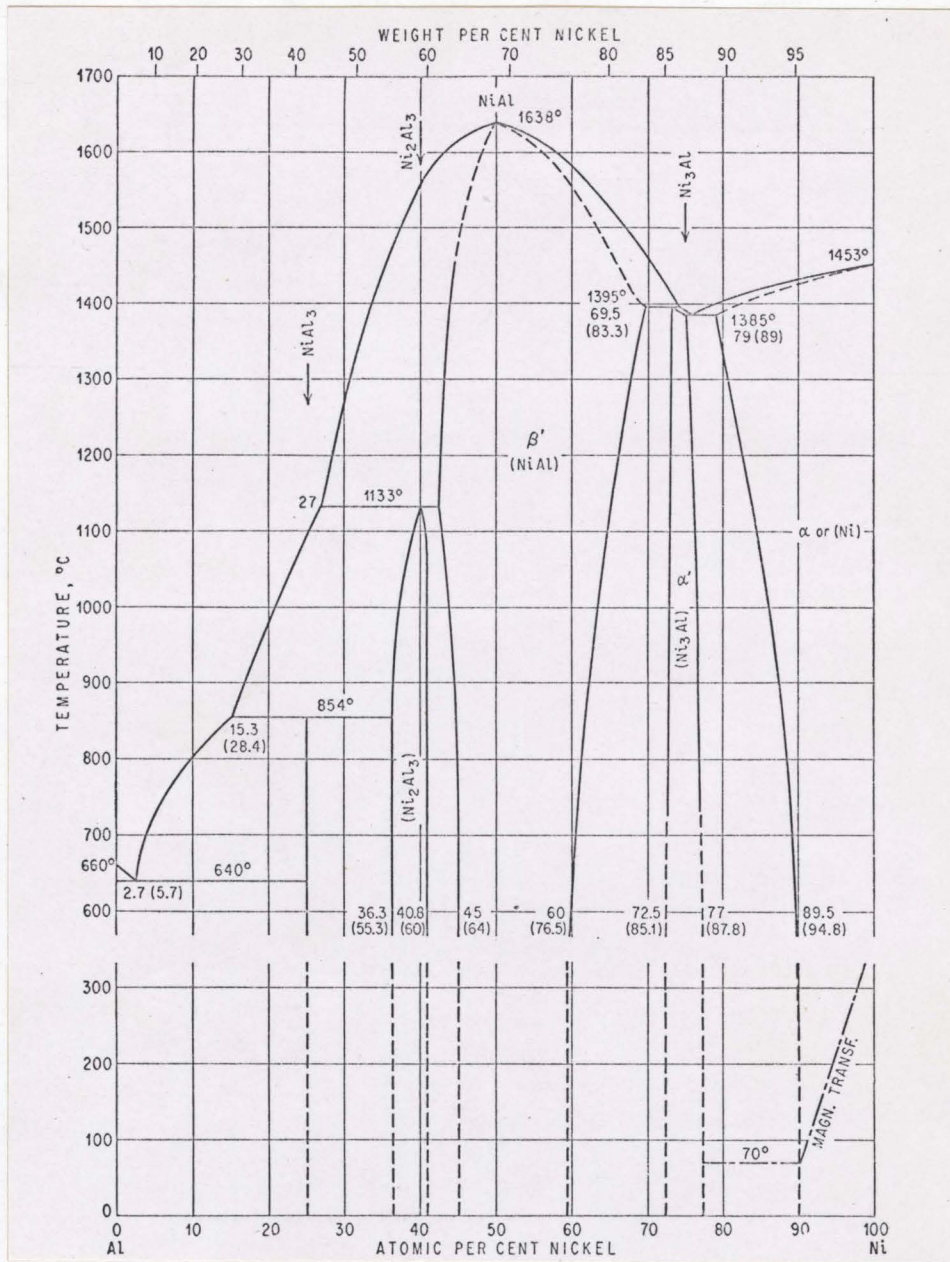


Fig. 1: Nickel-aluminum phase diagram (Hansen).

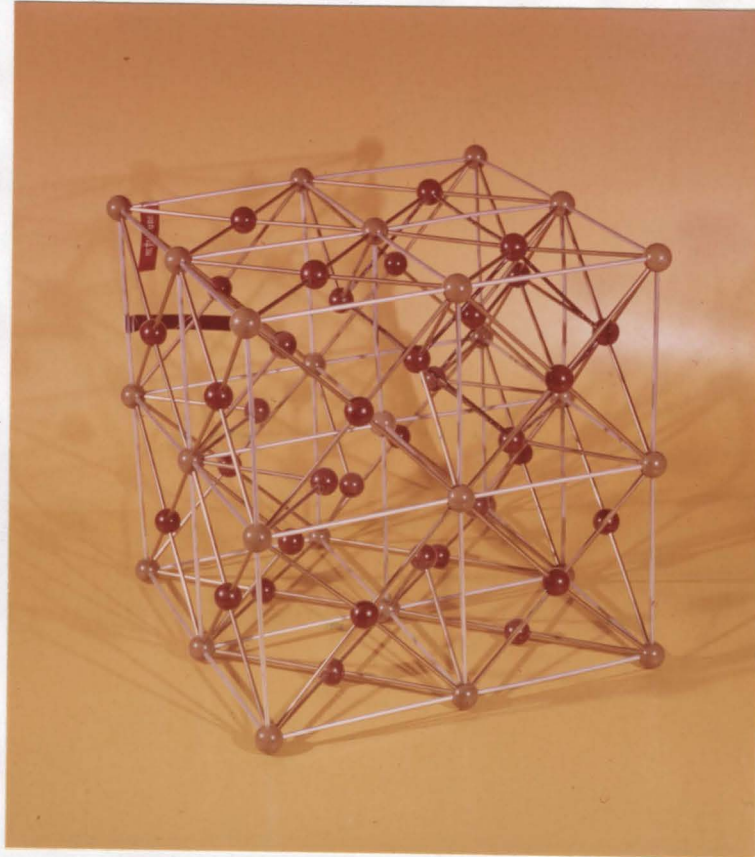


Fig. 2:  $L1_2$  lattice for  $Ni_3Al(\gamma')$ . Brown balls at faces nickel atoms, green balls at corners aluminum atoms.

Fig. 3: Crystal growing apparatus.

Fig. 2:  $L_2$  lattice for  $Al_3Ni(Y')$ . Brown balls at faces nickel atoms, green balls at corners aluminum atoms.

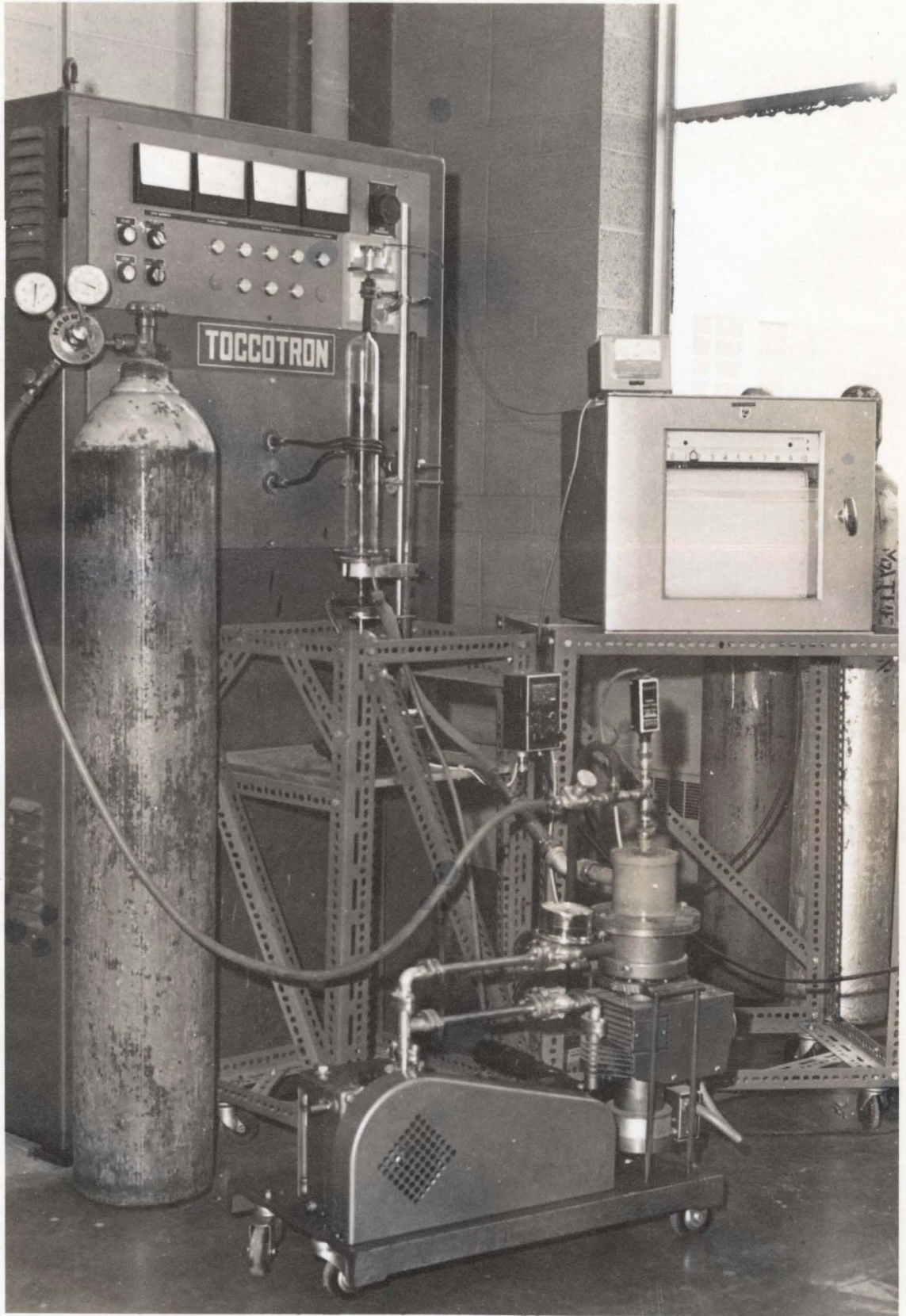
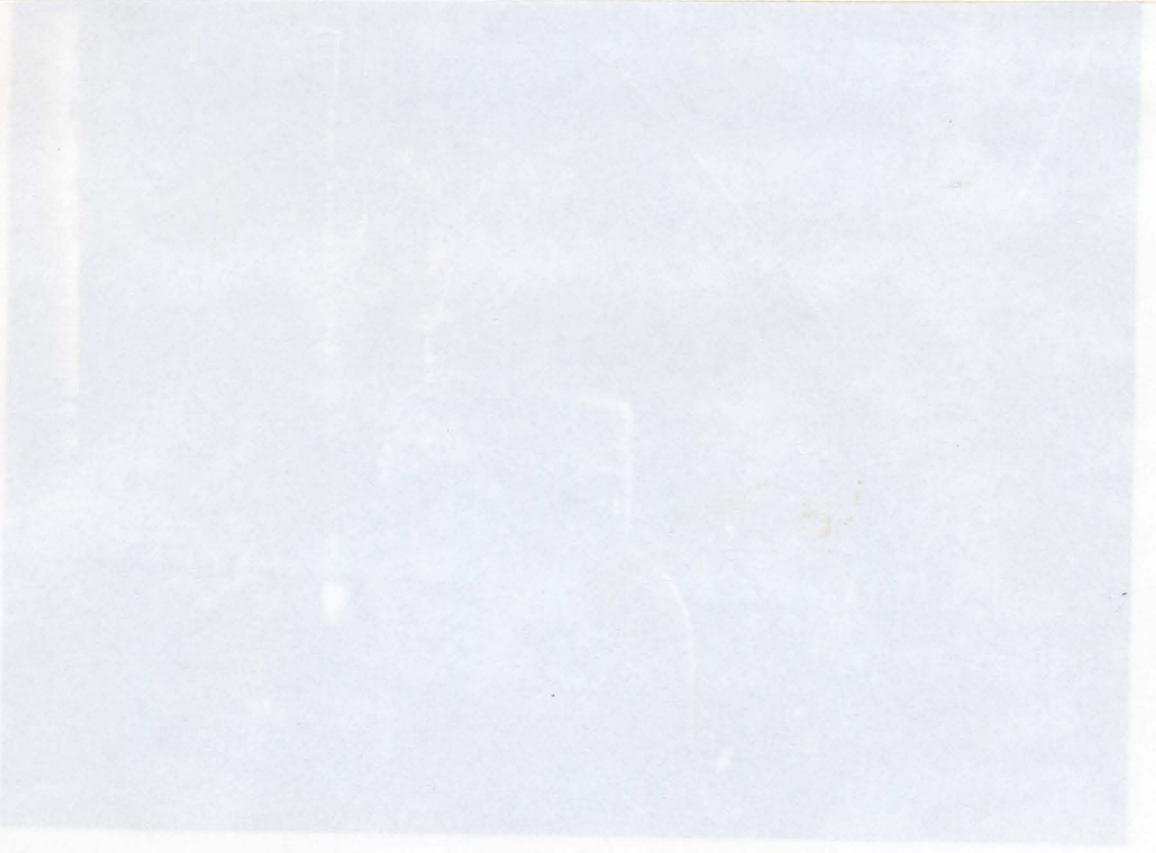
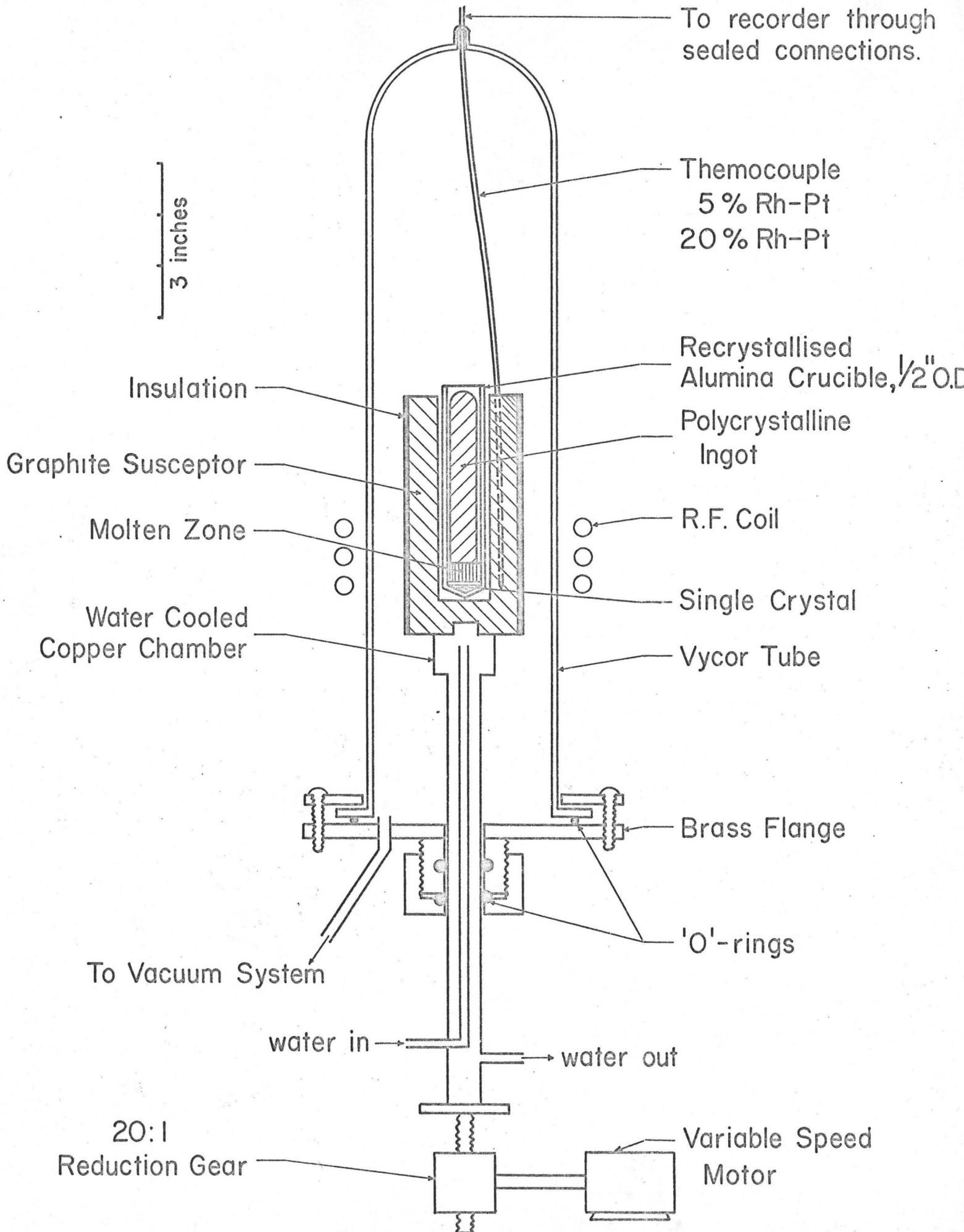




Fig. 4: Detailed schematic of crystal growing apparatus.





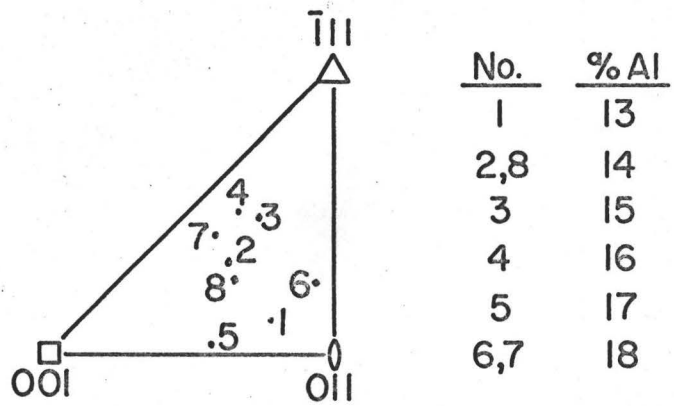


FIG. 5 : Orientation of single crystals, longitudinal axis.

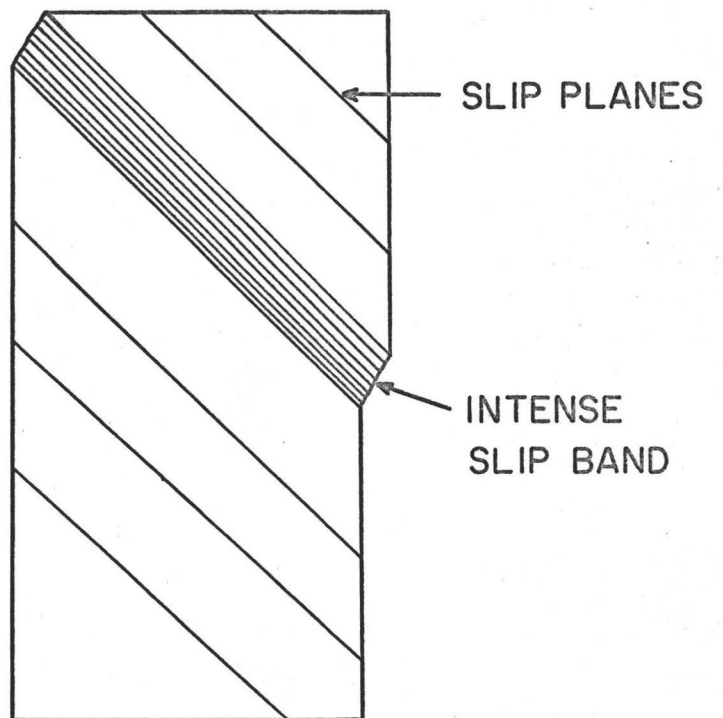


FIG. 6: Sketch of 14 % Al after 4.5 % strain.



Intense slip band  
Approx. 0.07" wide

Structure over most of  
crystal

Fig. 7: Micrograph of surface of 13<sup>a</sup>/o Al single crystal, aged 700<sup>o</sup>C, 6 hours after 3.5% compressive strain

X80

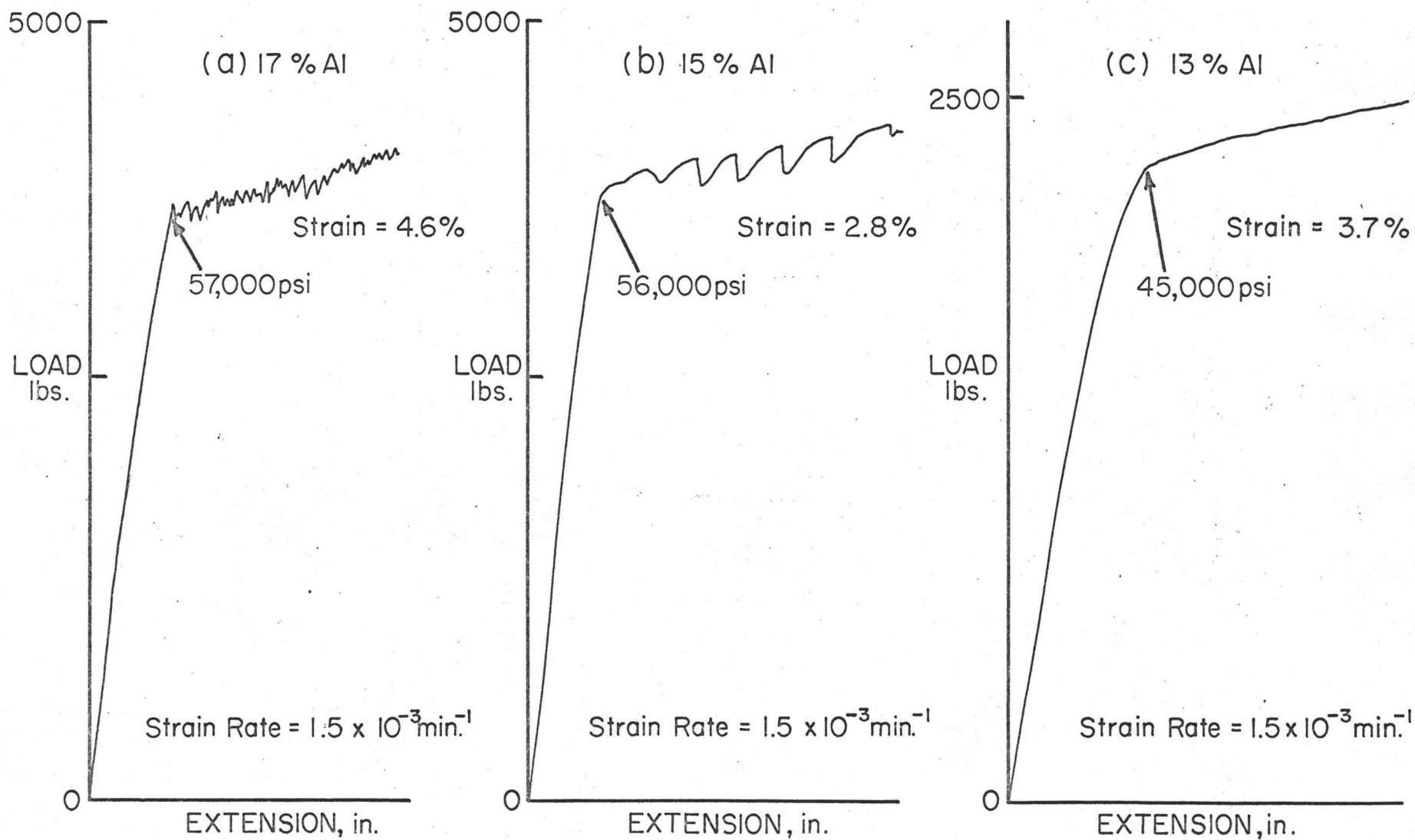


FIG. 8: Compression: load-extension curves for single crystals, aged at 700°C. for 6 hours.

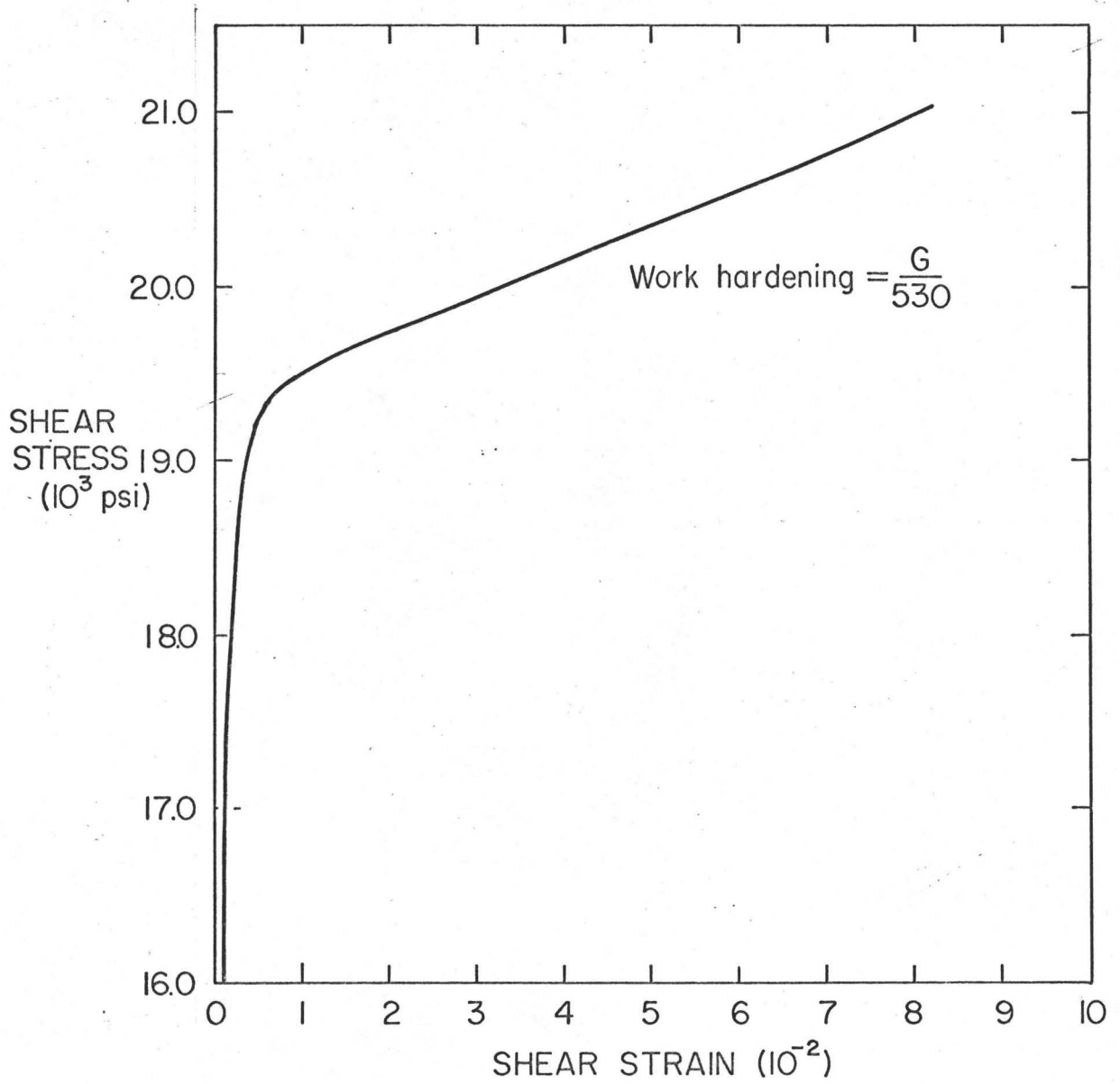
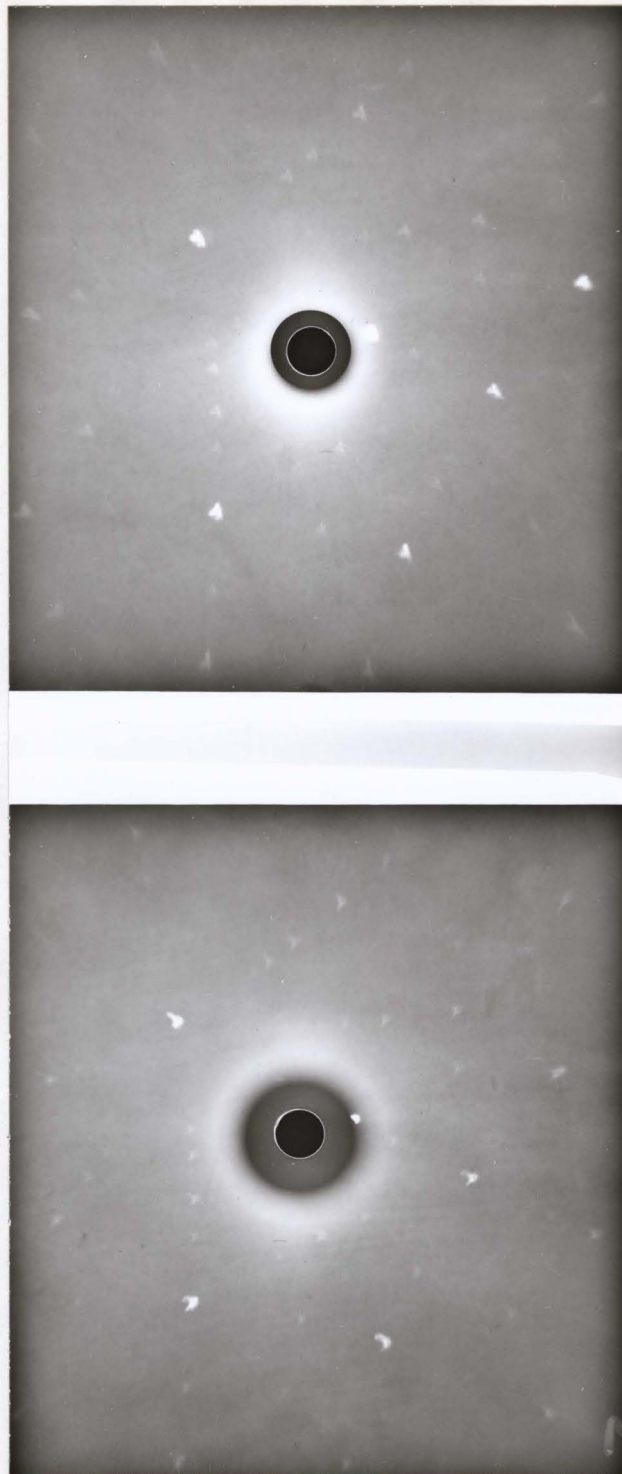


FIG. 9: Shear stress-shear strain curve for 14% Al single crystal. Aged at 700°C. for 3 hours.



(a)

(b)

Fig. 10: Back reflection Laue of 13<sup>a</sup>/o Al single crystal aged 700<sup>o</sup>C for 6 hours, after 3.5 % compressive strain. (a) at intense slip band (b) away from intense slip band.

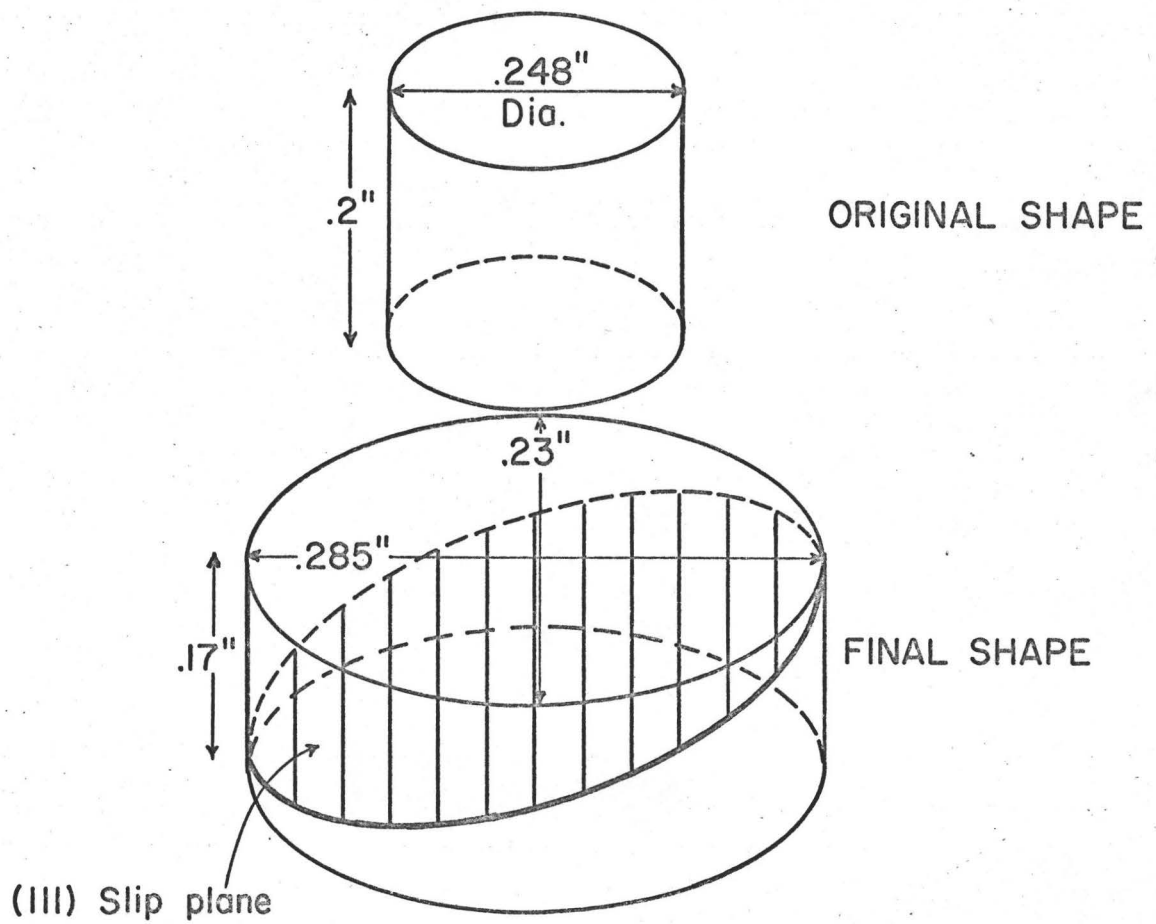


FIG. II: Shape of 14% Al single crystal (No.2) after 15 % compressive strain. (Not to scale).

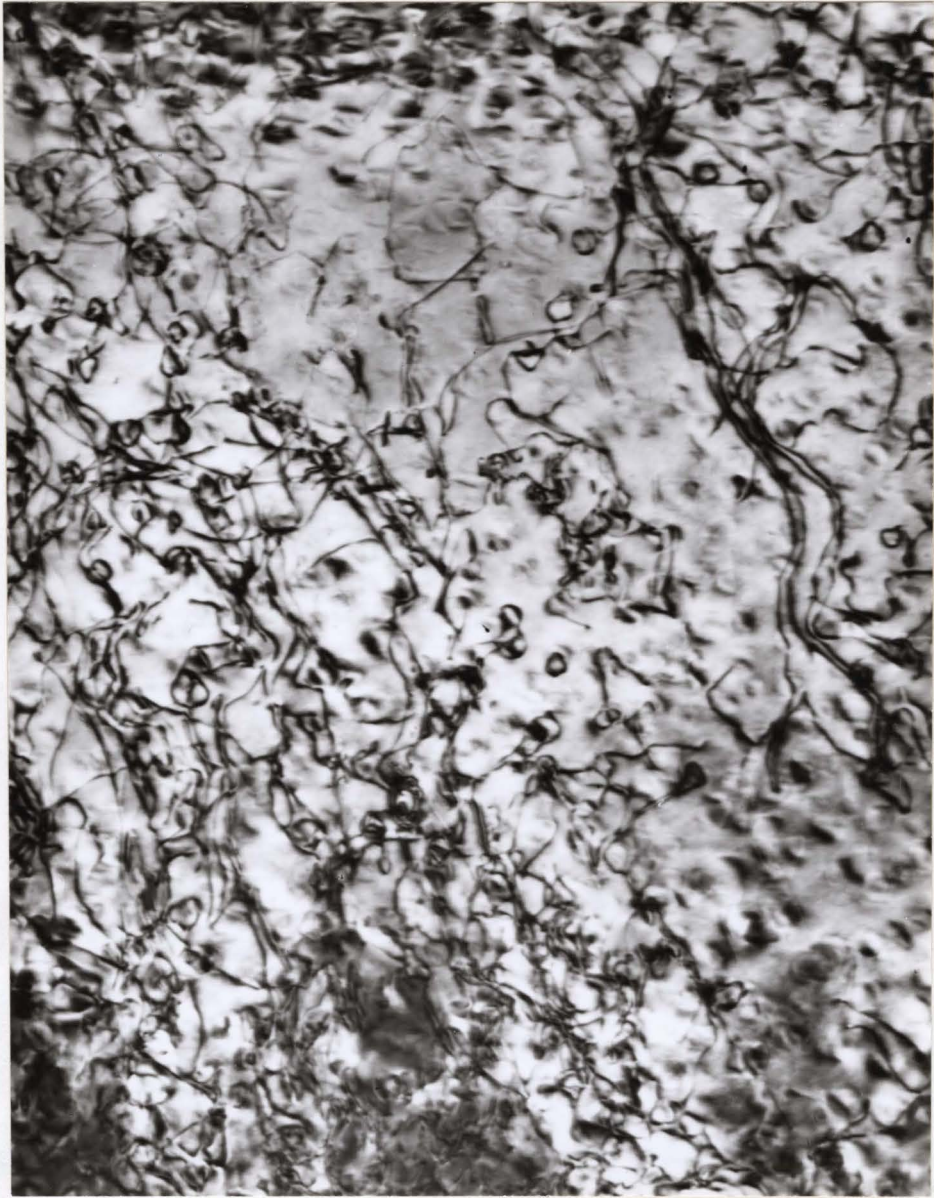


Fig. 12: Bright field electron micrograph of 14 <sup>a</sup>/o single crystal (No. 2) aged 700<sup>0</sup>C for 3 hours, after total compressive strain of 20%. (111) section X60,000

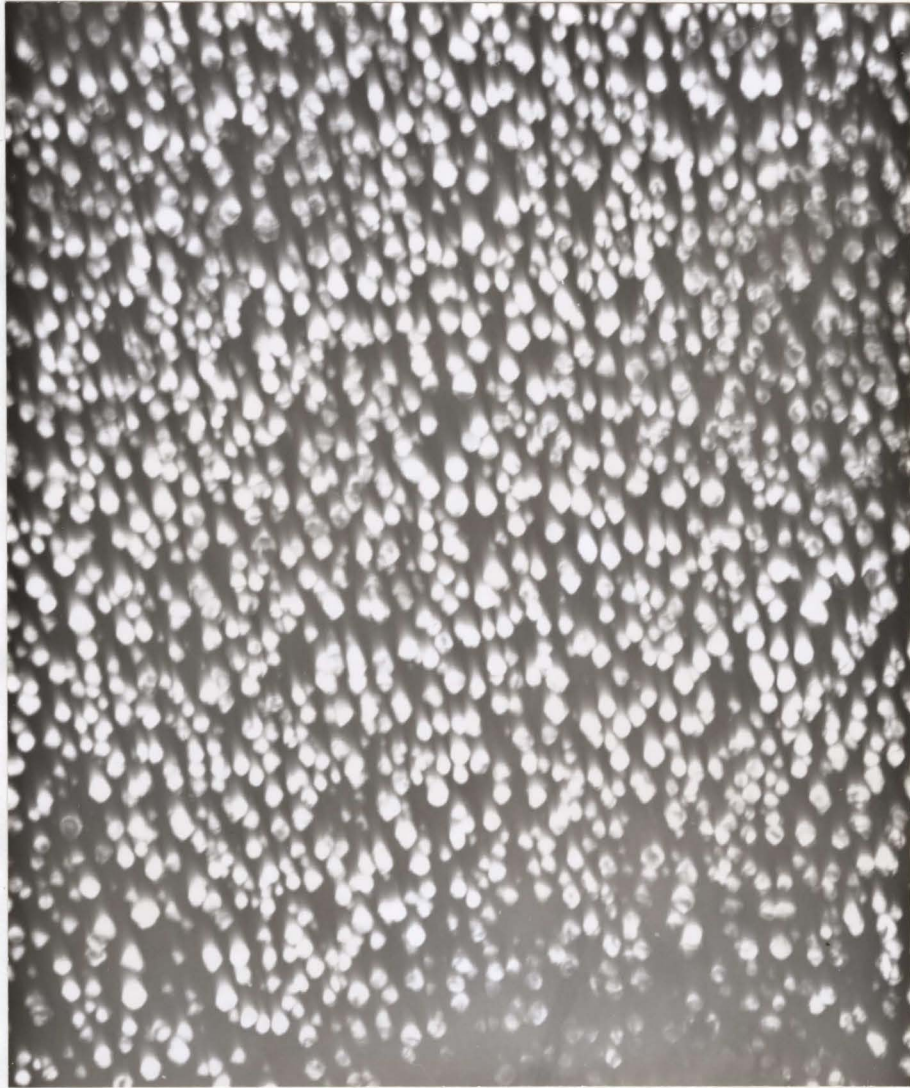


Fig. 13: Dark field electron micrograph from superlattice reflection of foil in Fig. 12.

X35,000

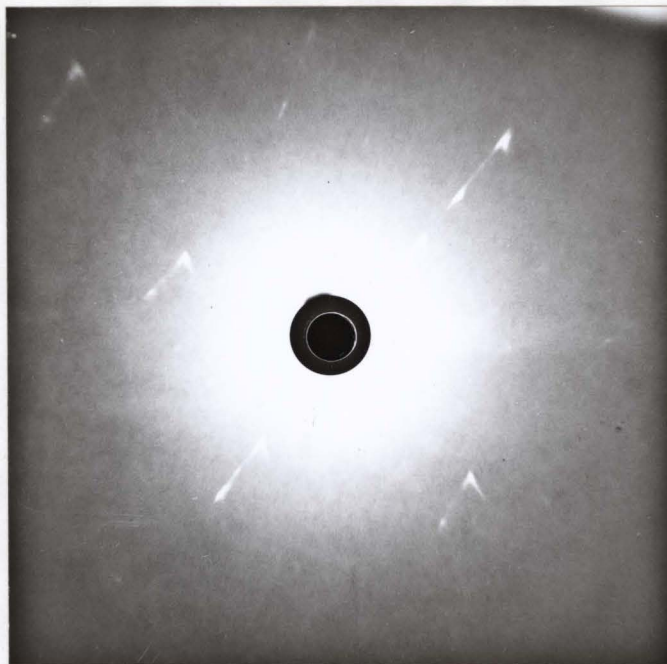


Fig. 14: Back reflection Laue from (111) section of 14<sup>a</sup>/o Al single crystal (No. 2) aged 700°C, 3 hours after total compressive strain of 20%.

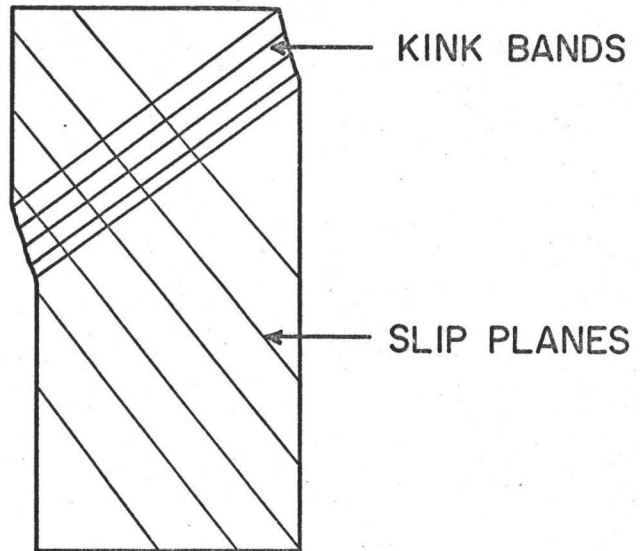
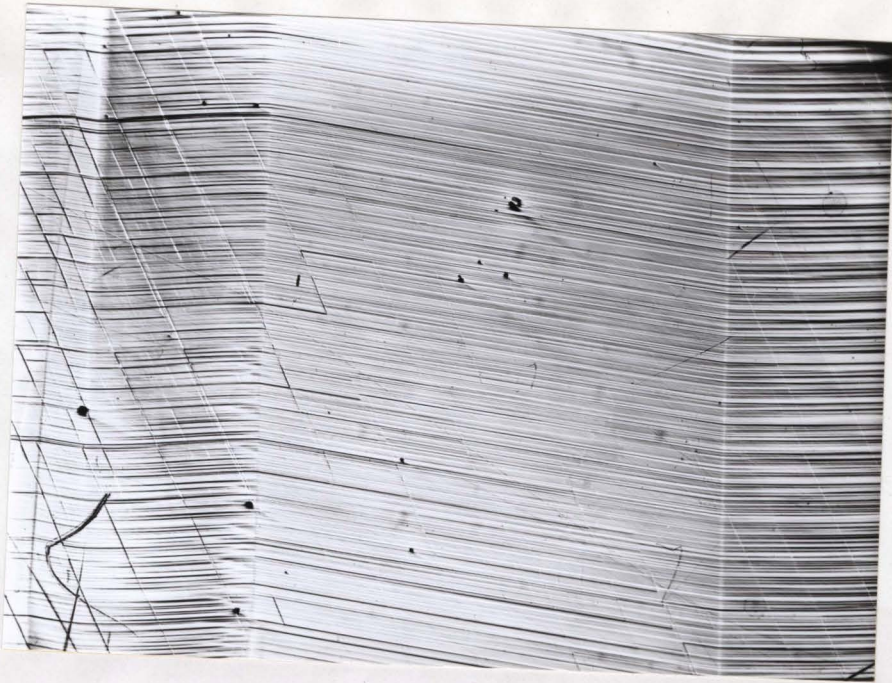


FIG: 15: Sketch of 16 % Al crystal show Kink bands.



Kink band 2

Kink band 1

Fig. 16: Micrograph of surface of 15<sup>a</sup>/o Al single crystal aged 700<sup>o</sup>C for 6 hours, showing kink bands.

X80



Fig. 17: Back reflection Laues from surface shown in Fig. 16.  
(a) to the right of kink band 1  
(b) inbetween kink bands 1 and 2  
(c) to the left of kink band 2  
Orientations (a) and (c) are identical.

Kink band 1

Kink band 2

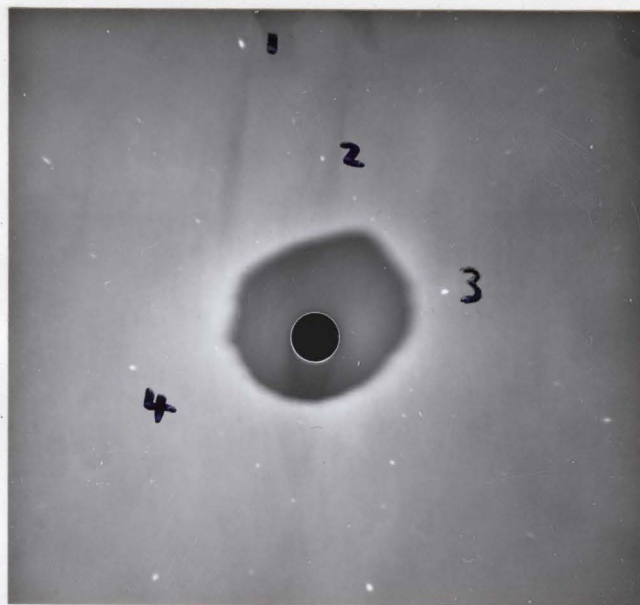
Fig. 16: Micrograph of surface of 15 Å (011) single crystal aged 700°C

88X

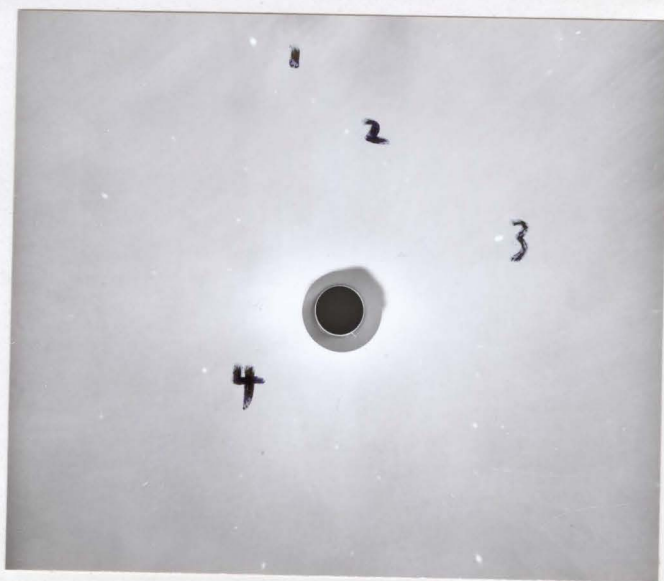
for 6 hours, showing kink bands.



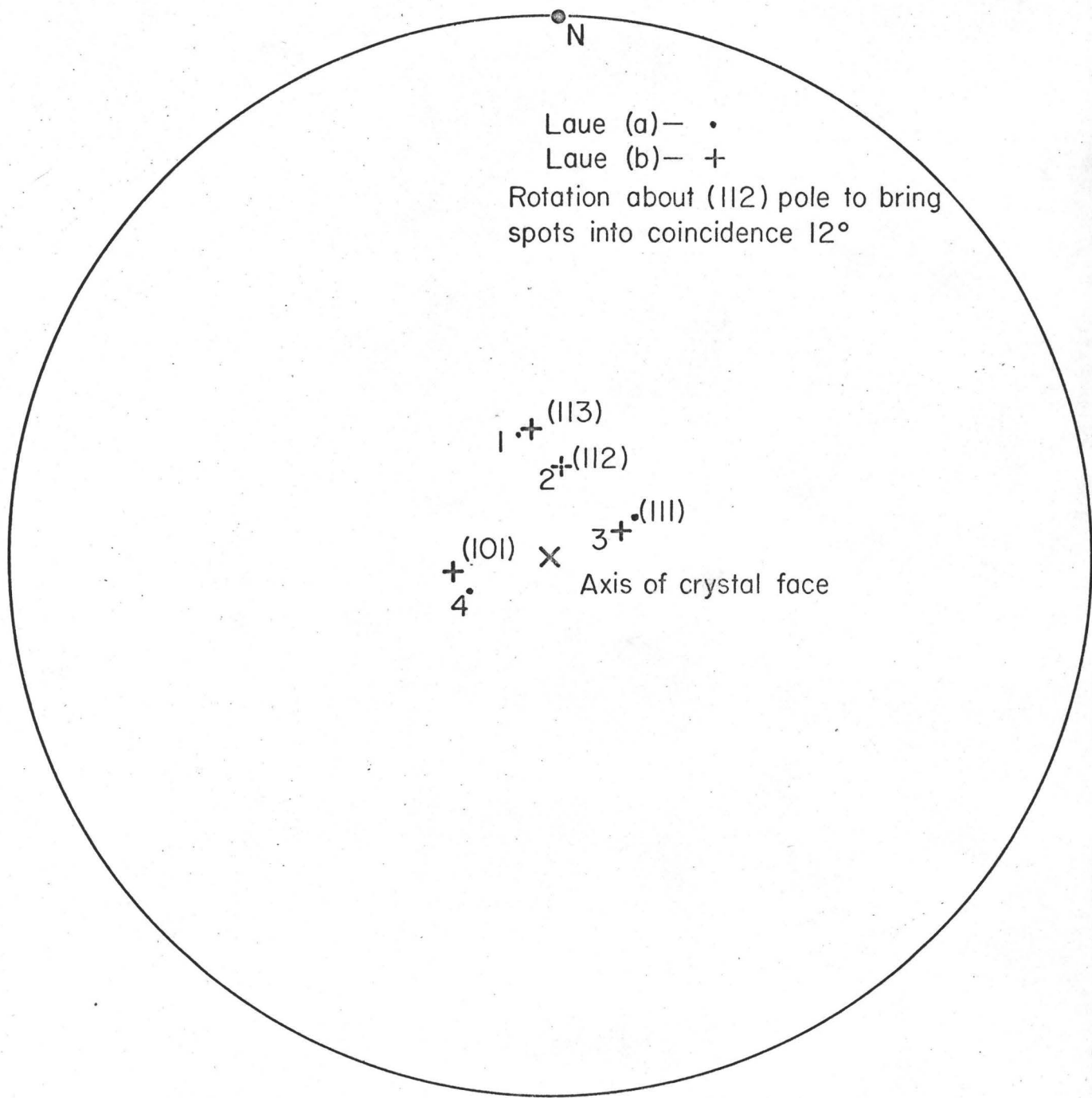
(a)



(b)



(c)



STEREOGRAPHIC PROJECTION

FIG. 18 Stereographic projection: Showing rotation across a kink band with axis of rotation  $[112]$  direction. 15% Al single crystal.

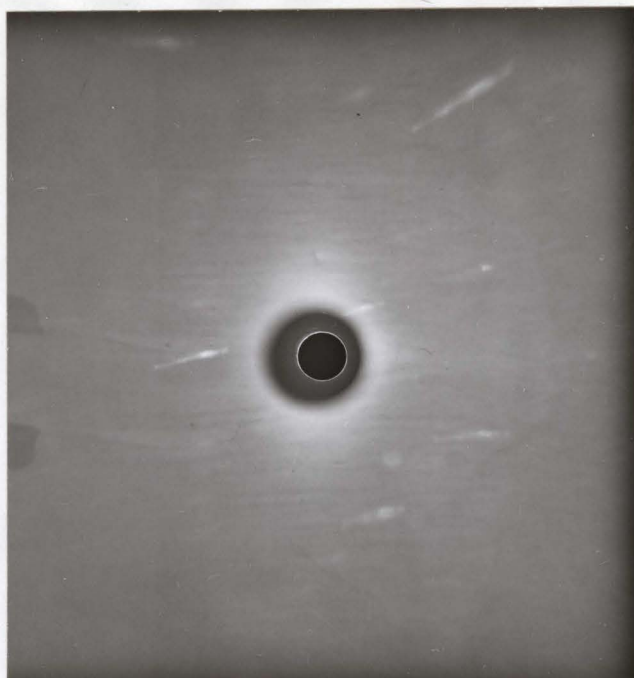


Fig. 19: Back reflection Laue taken directly on kink band at surface  
(cf. Fig. 17).

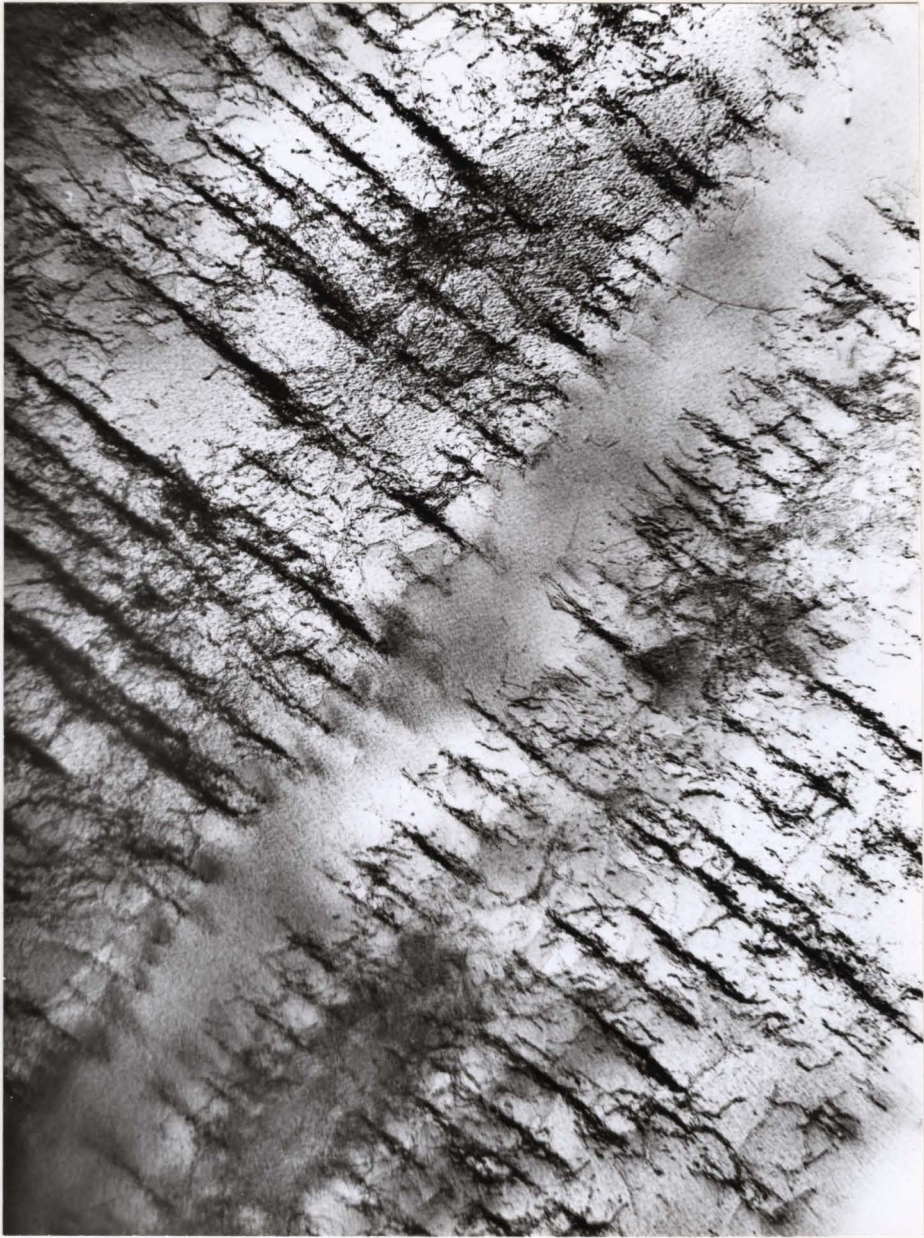


Fig. 20: Transmission electron micrograph of section from 15<sup>a</sup>/o Al single crystal aged 700<sup>o</sup>C 6 hours. Section nearly perpendicular to kink band. X8,000

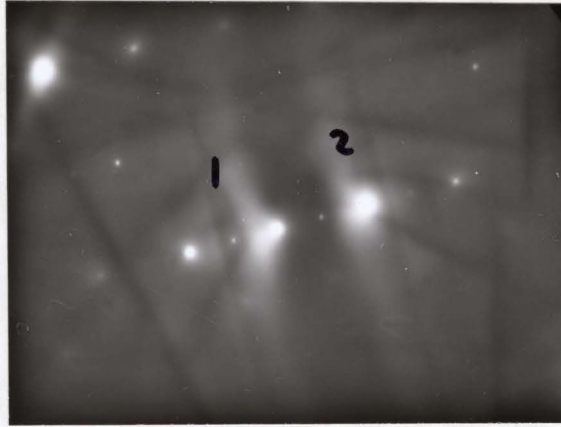


Fig. 21: Electron diffraction patterns showing shift in Kikuchi lines denoting change in orientation on crossing clear zones (see Fig. 20).



Fig. 22: Transmission electron micrograph from (111) section of 15<sup>a</sup>/o Al single crystal aged 700<sup>o</sup>C for 6 hours showing dislocation pairs in pile-ups associated with kink bands. X8,000

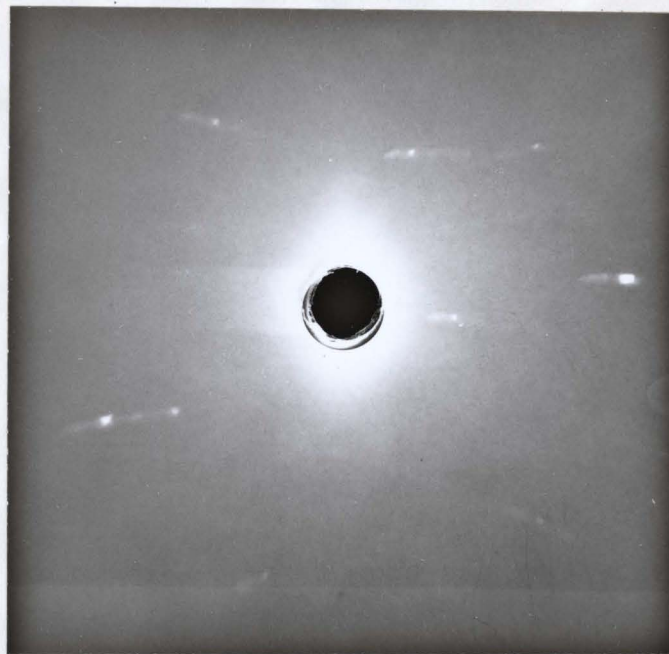
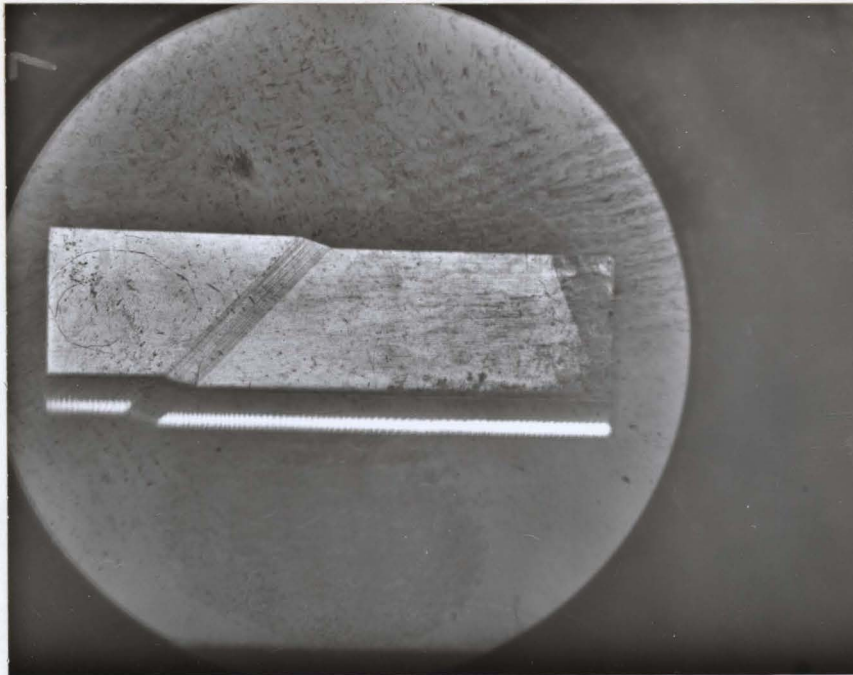
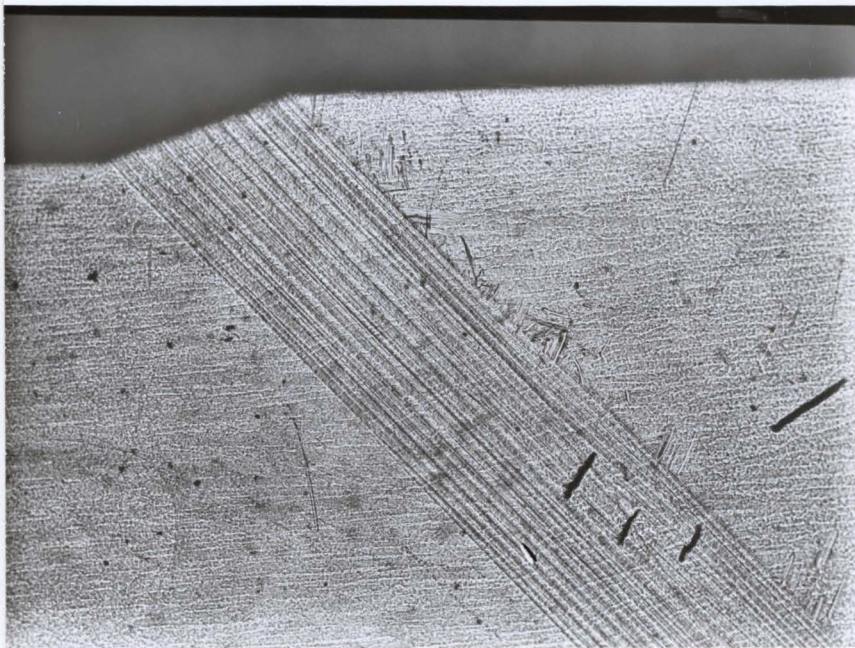


Fig. 23: Back reflection Laue of section used in electron microscopy of kink bands (see Fig. 20).



(a)



(b)

Fig. 24: Optical micrographs of 17<sup>a</sup>/o single crystal aged 700<sup>o</sup>C for 6 hours after 2% compressive strain. (a) X7 (b) X20

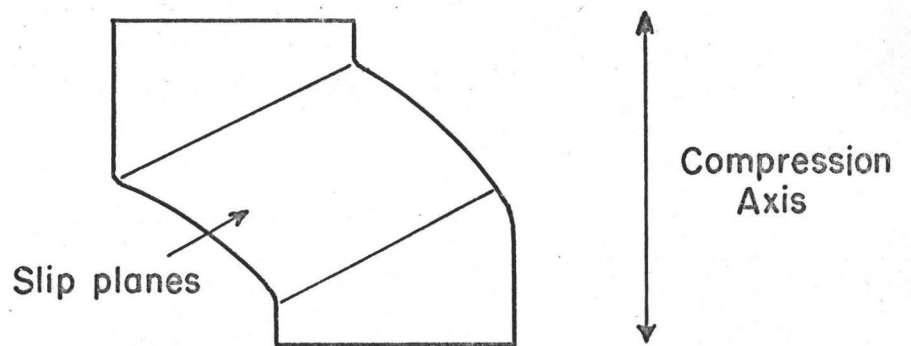
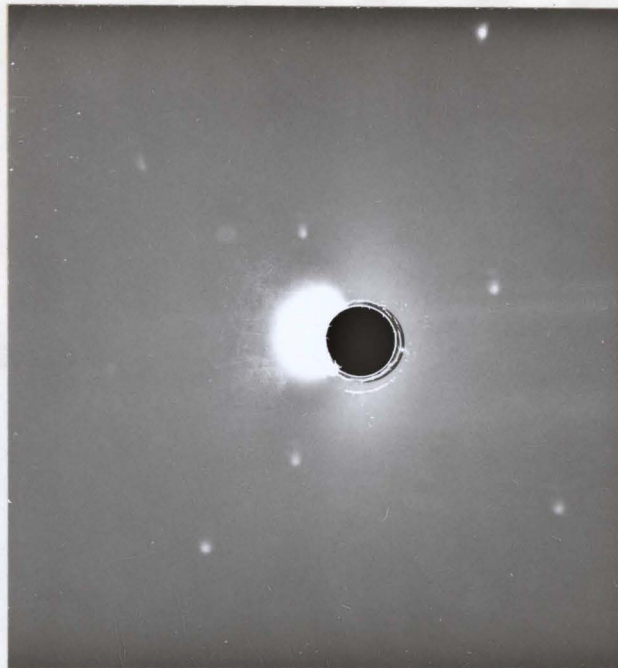


FIG.25: Shape of 17 % Al single crystal after 28 % compressive strain. (Not to scale).



Fig. 26: Surface slip line structure of 17<sup>a</sup>/o Al single crystal aged 700<sup>o</sup>C for 6 hours and compressed 4%.

X80



(a)



(b)

Fig. 27: Back reflection Laues on surface of 17<sup>a</sup>/o Al single crystal aged 700<sup>o</sup>C for 6 hours after 12% compressive strain. (a) on slip band (b) outside slip band.

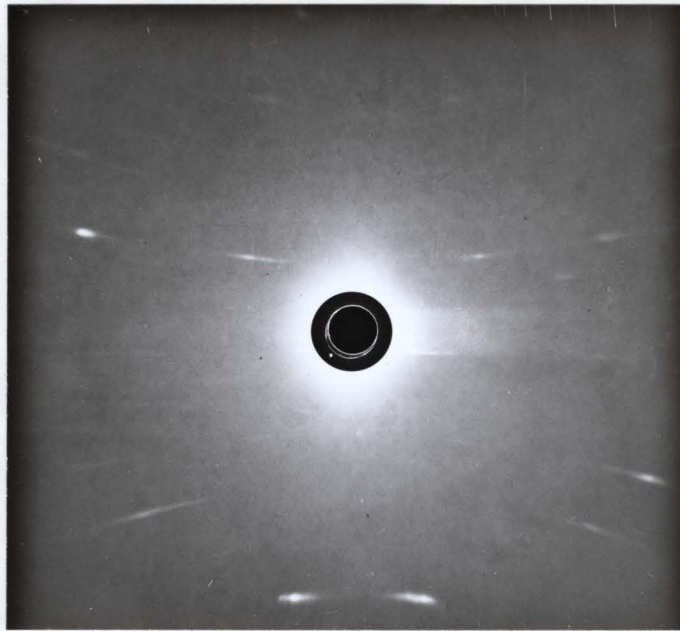


Fig. 28: Back reflection Laue on (111) section of 17<sup>a</sup>/o Al single crystal aged 700<sup>o</sup>C for 6 hours after 28% compressive strain.

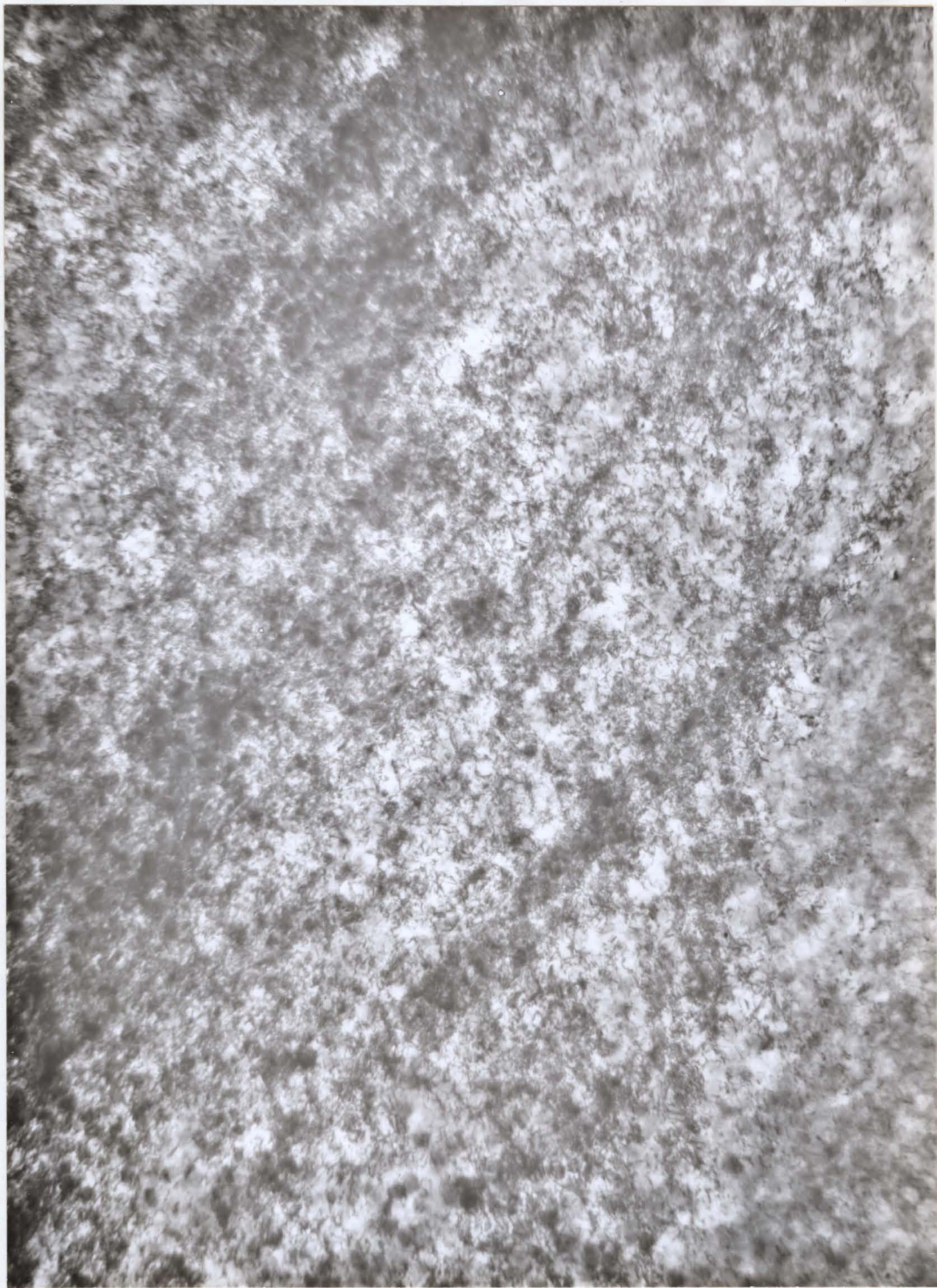


Fig. 29: Transmission electron micrograph of (111) section from 17 <sup>a</sup>/o single crystal aged 700°C for 6 hours after compressive strain of 28%. X25,000

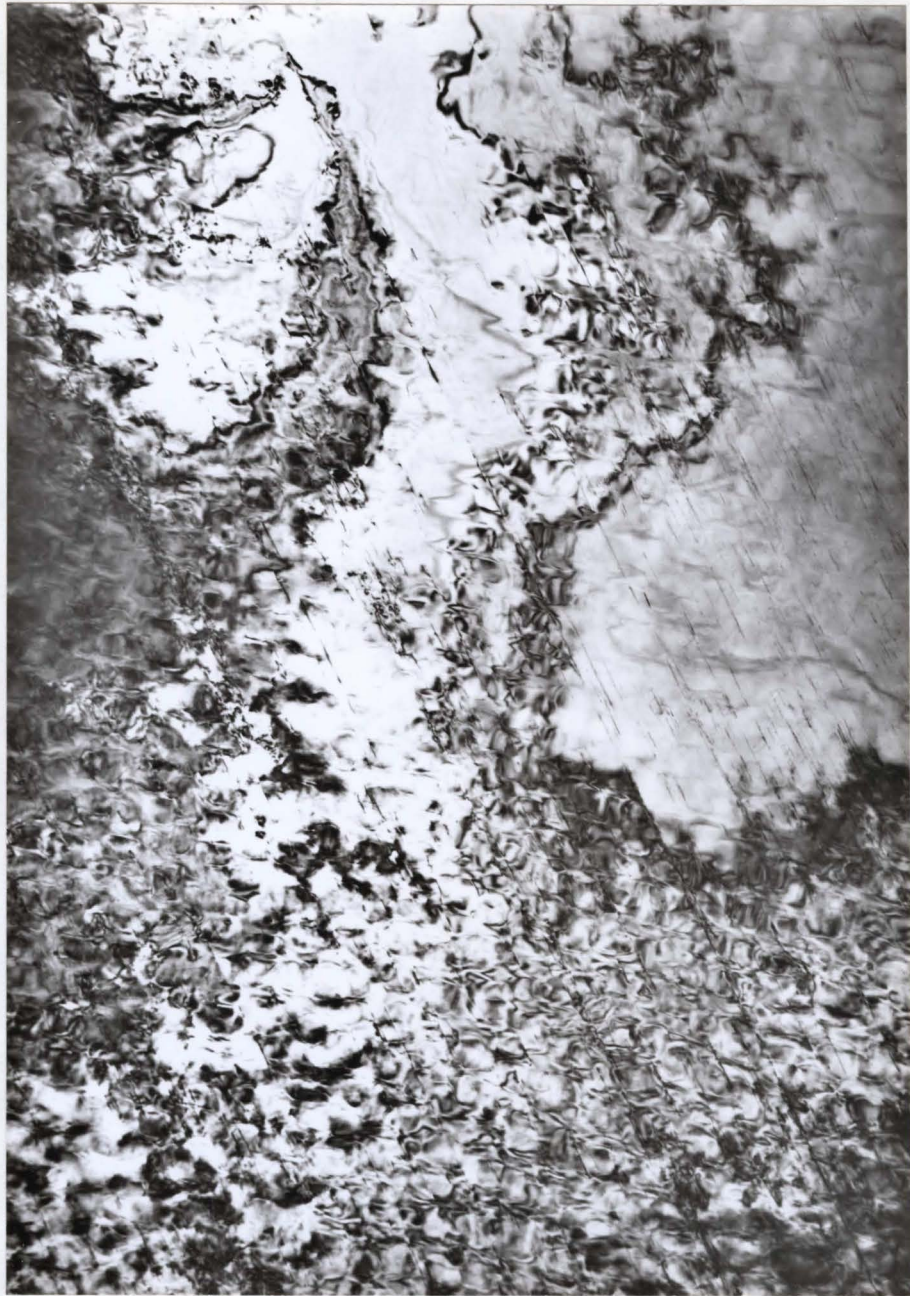


Fig. 30: Transmission electron micrograph of section perpendicular to (111) slip planes of 17 % Al single crystal aged 700°C for 6 hours after 28% compressive strain. X35,000

Fig. 31: Dark field electron micrograph using superlattice reflection from foil in Fig. 30. Showing shearing of particles by dislocations. X35,000

Fig. 30: Transmission electron micrograph of section perpendicular to (111) slip planes of 1% Al single crystal aged 100°C for 6 hours after 50% compressive strain. X35,000





Fig. 32: Transmission electron micrograph of section perpendicular to (111) slip planes of 17<sup>a</sup>/o Al single crystal aged 700<sup>o</sup>C for 6 hours after 28% compressive strain. X10,000



Fig. 33: Carbon replica of surface of 17<sup>a</sup>% Al single crystal, aged 700<sup>o</sup>C 6 hours, after 12% compressive strain. X60,000



Fig. 34: Carbon replica of (100) section from 17<sup>a</sup>/o Al single crystal  
slow cooled from 1300 to 700<sup>0</sup>C in 3 hours. X20,000

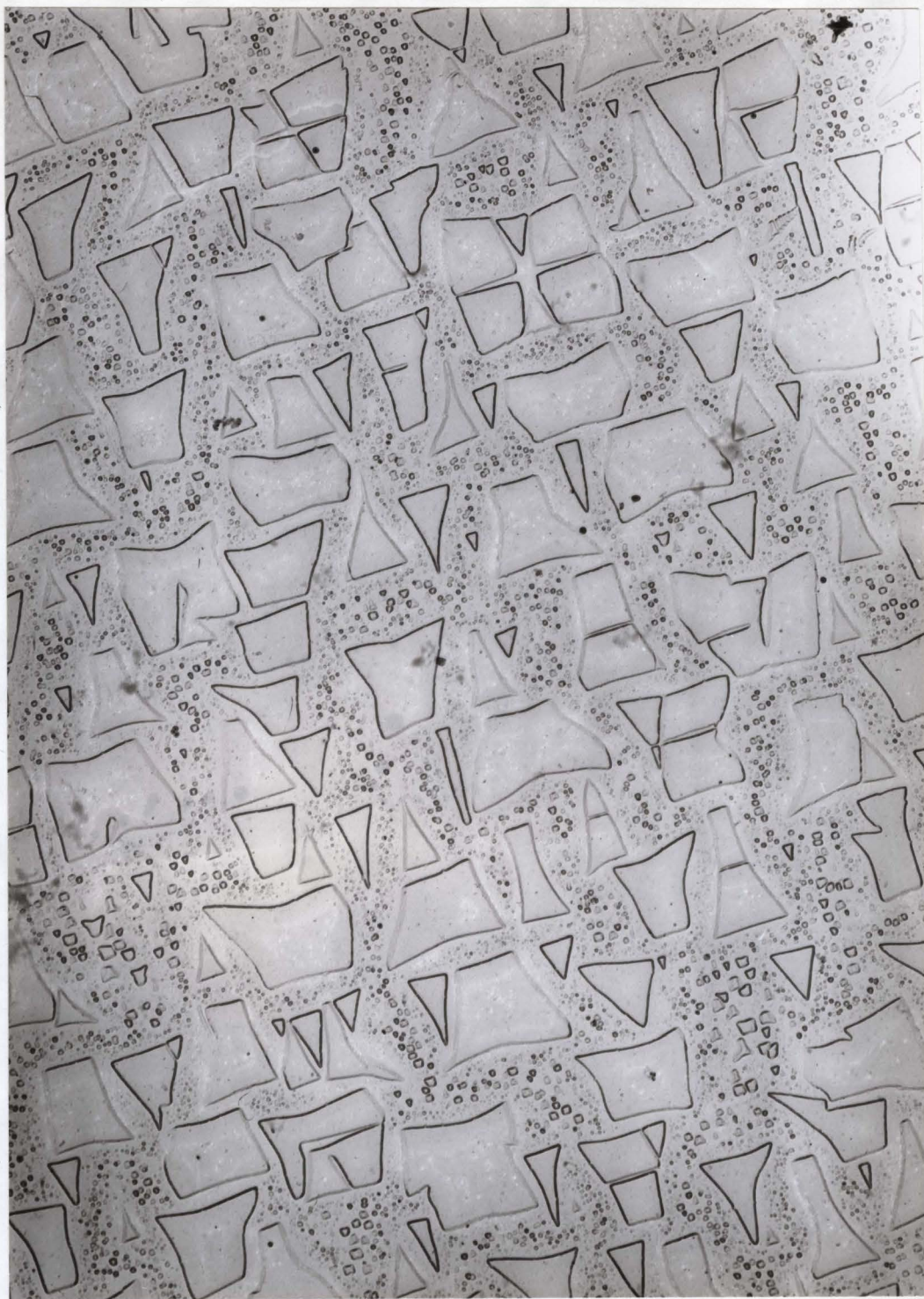


Fig. 35: Carbon replica of (111) section from 17<sup>a</sup>/o Al single crystal  
slow cooled 1300<sup>o</sup>C to 700<sup>o</sup>C in 3 hours. X16,000



Fig. 36: Transmission electron micrograph of (100) section from 17<sup>a</sup>/o  
Al single crystal slow cooled from 1300<sup>o</sup>C to 700<sup>o</sup>C in 3 hours.  
X35,000



Fig. 37: Transmission electron micrograph of (111) section from 17<sup>a</sup>/o Al single crystal slow cooled 1300-700<sup>o</sup>C in 3 hours and compressed 2% strain. Showing overlapping  $\delta$ -fringes. X24,000



Fig. 38: Transmission electron micrograph of (100) section from 17<sup>a</sup>/o Al single crystal, slow cooled 1300 to 700°C in 3 hours and compressed 5%.

X35,000

A - dislocations at interface

B - strain contrast



Fig. 39: Transmission electron micrograph of (100) section of 17<sup>a</sup>/o Al single crystal, slow cooled 1300 to 700°C in 3 hours, cold rolled 3%. X35,000  
A - slip dislocations on 2 systems meeting at particle interface

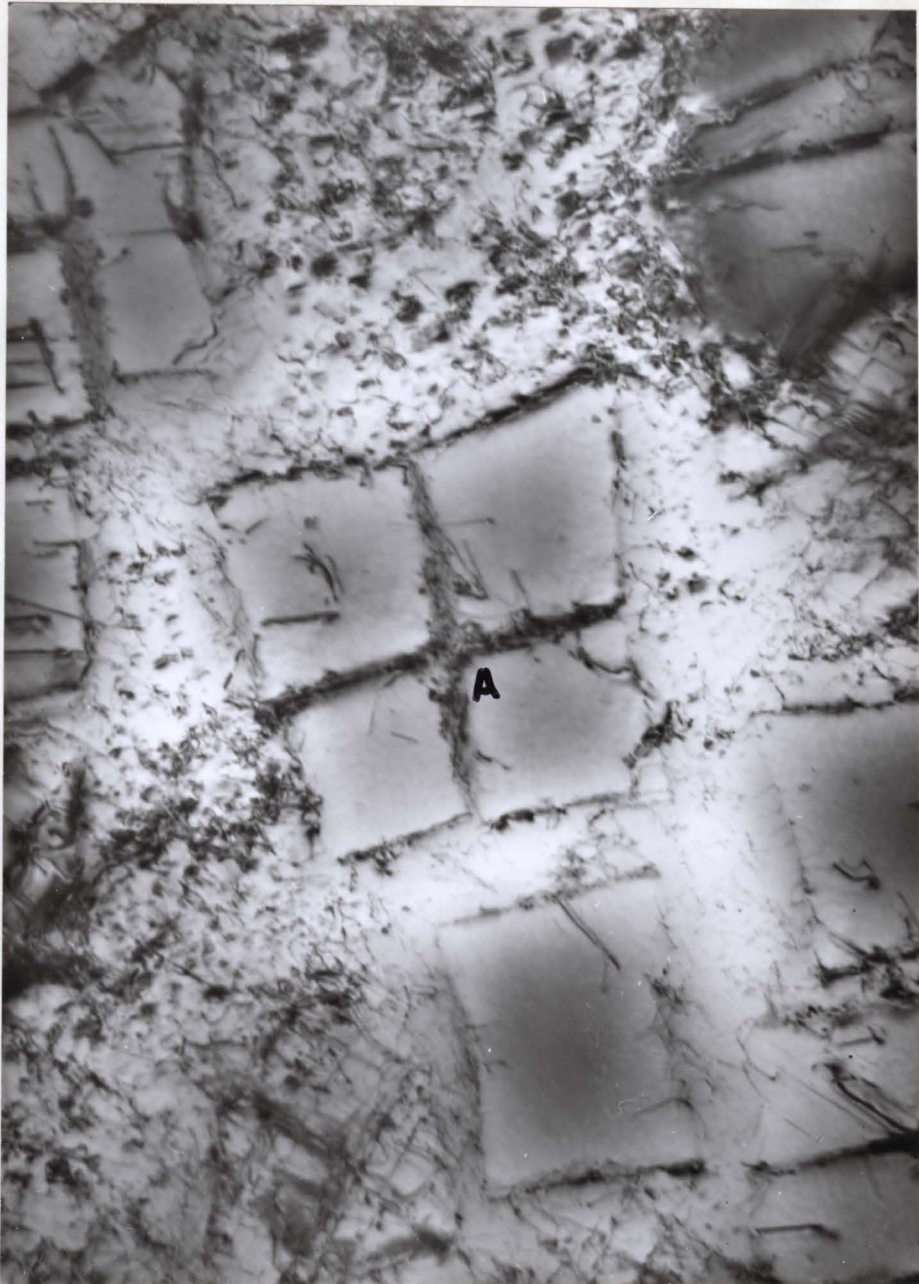
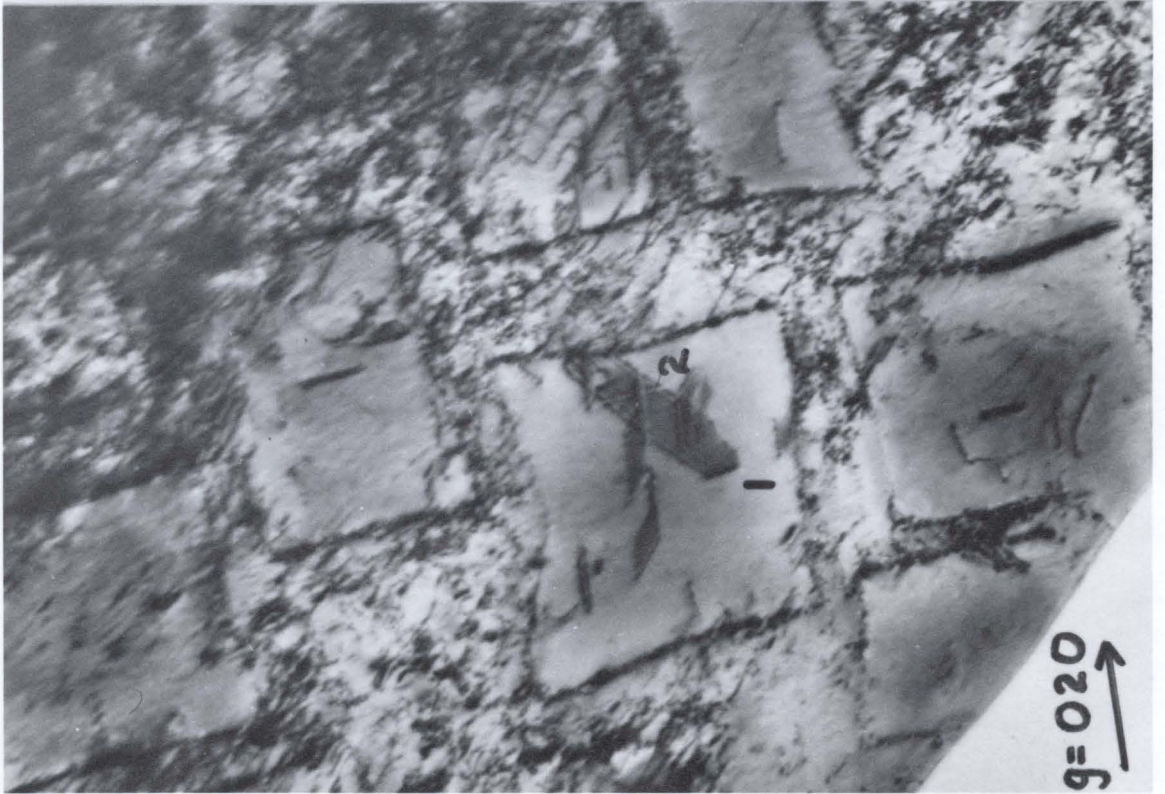
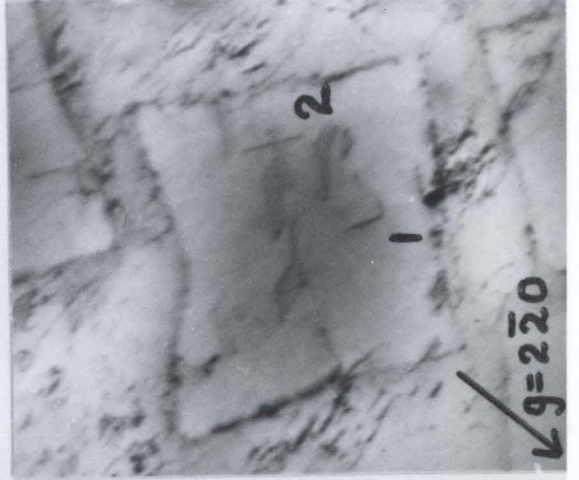
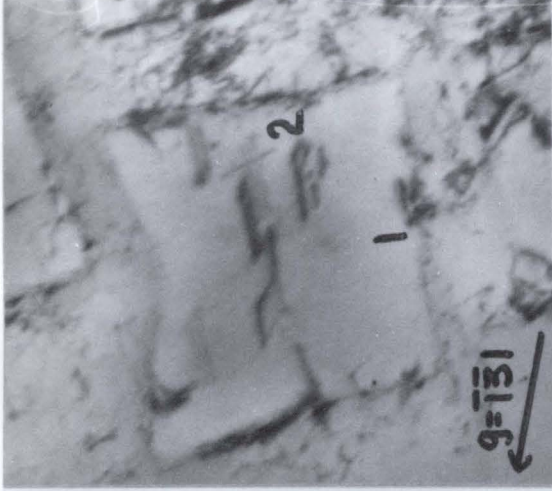


Fig. 40: Transmission electron micrograph of (100) section from 17<sup>a</sup>/o Al crystal, slow cooled 1300 to 700<sup>o</sup>C, cold rolled 3%. X35,000

A - dislocations in narrow channel between particles in a cluster.

Fig. 41: Transmission electron micrograph of (100) section from 17<sup>a</sup>/o Al single crystal slow cooled 1300 to 700°C in 3 hours, cold rolled 3%.  
Showing effect of 3 different reflection conditions on visibility stacking fault and boundary partial dislocations. X35,000



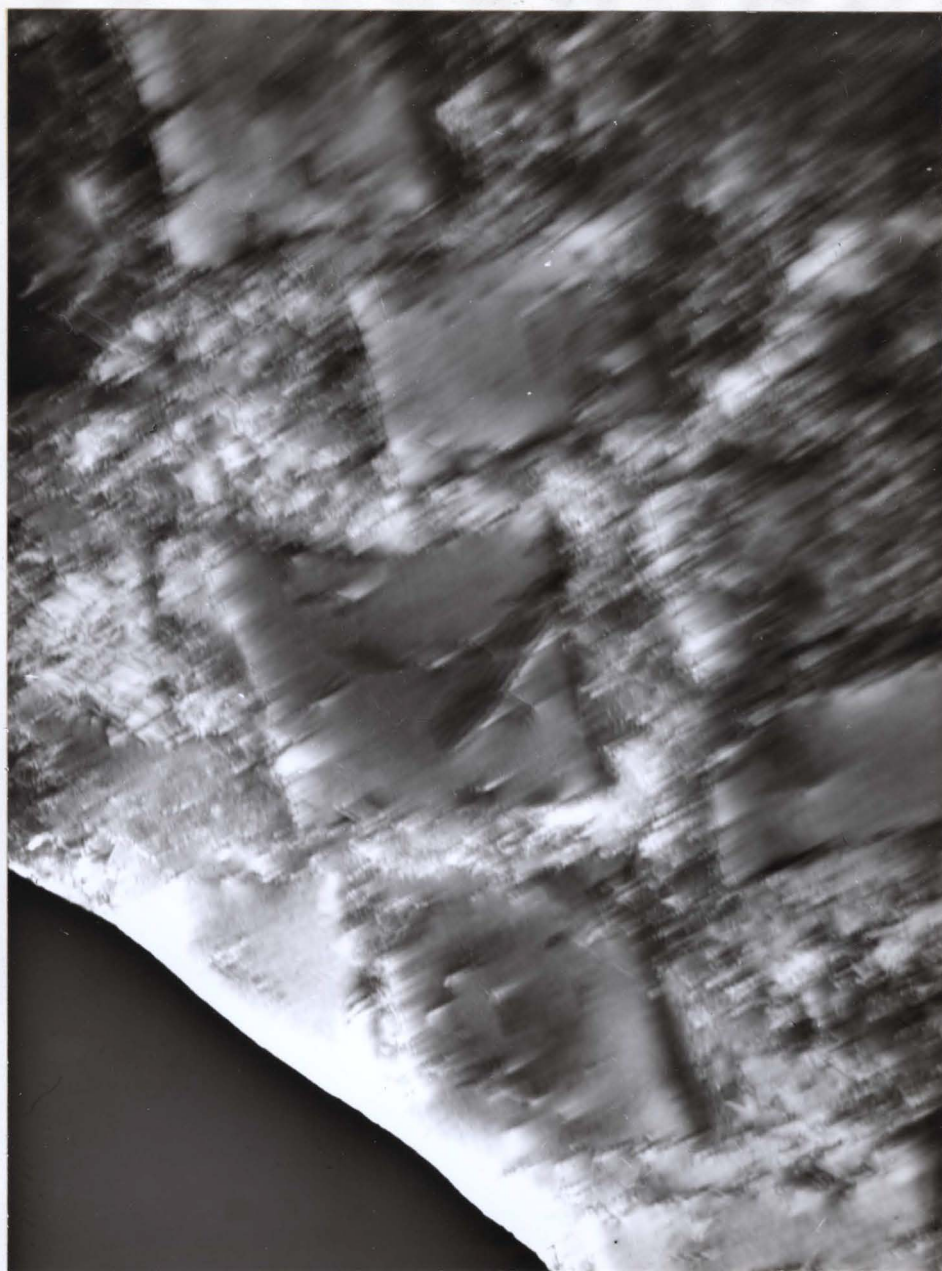


Fig. 42: Dark field electron micrograph from 020 reflection of (100) section of 17<sup>a</sup>/o Al single crystal, slow cooled 1300 to 700°C in 3 hours, cold rolled 3%. X35,000



Fig. 43: Transmission electron micrograph of (111) section from 17<sup>a</sup>/o Al single crystal slow cooled 1300 to 700°C in 3 hours, cold rolled 3%.

A - dislocation pile-up

B - constriction of 2 unit dislocations to give superdislocation in  $\gamma'$  particle.

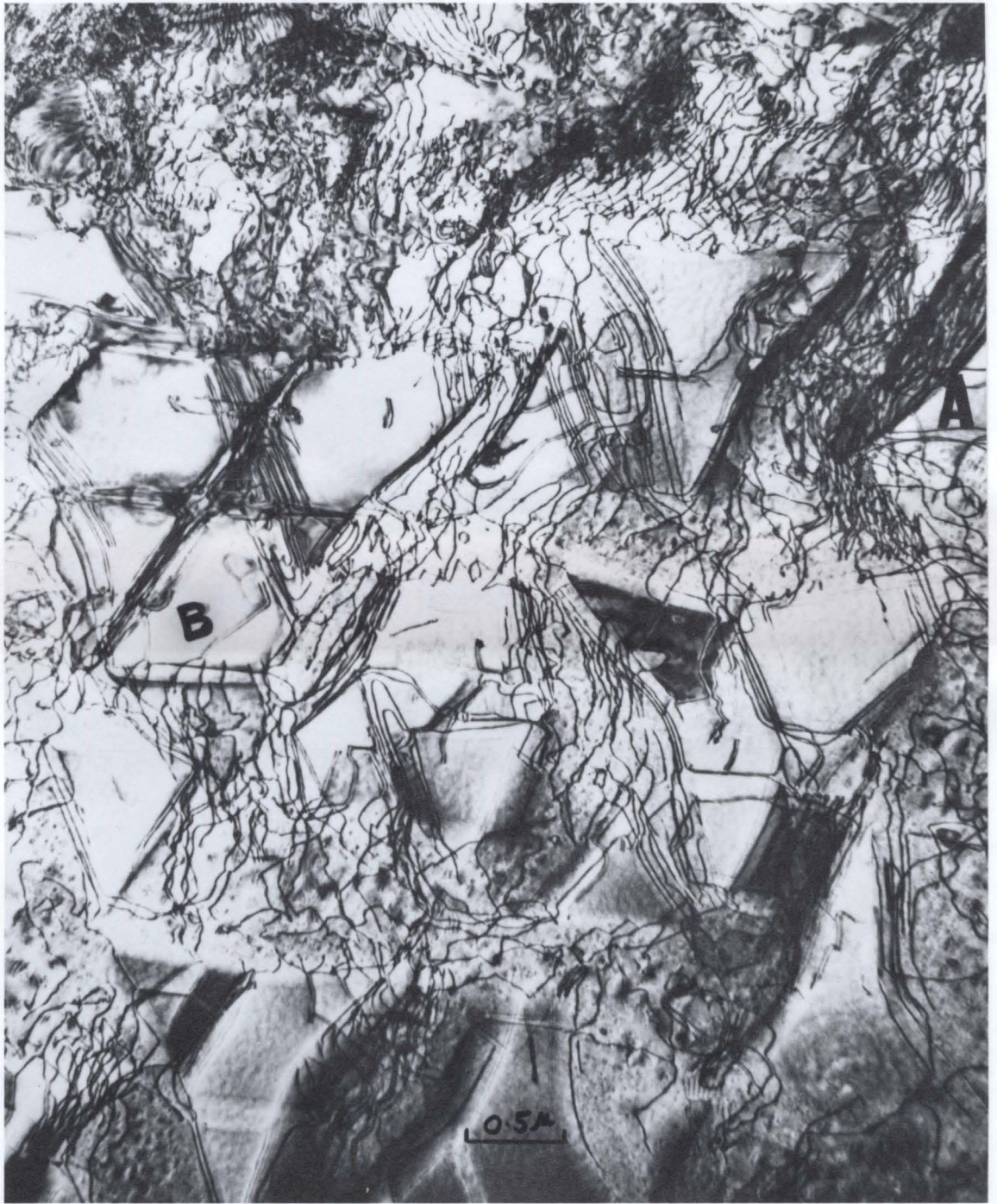




Fig. 44: As Fig. 43 showing shearing of particle by dislocations on slip plane.





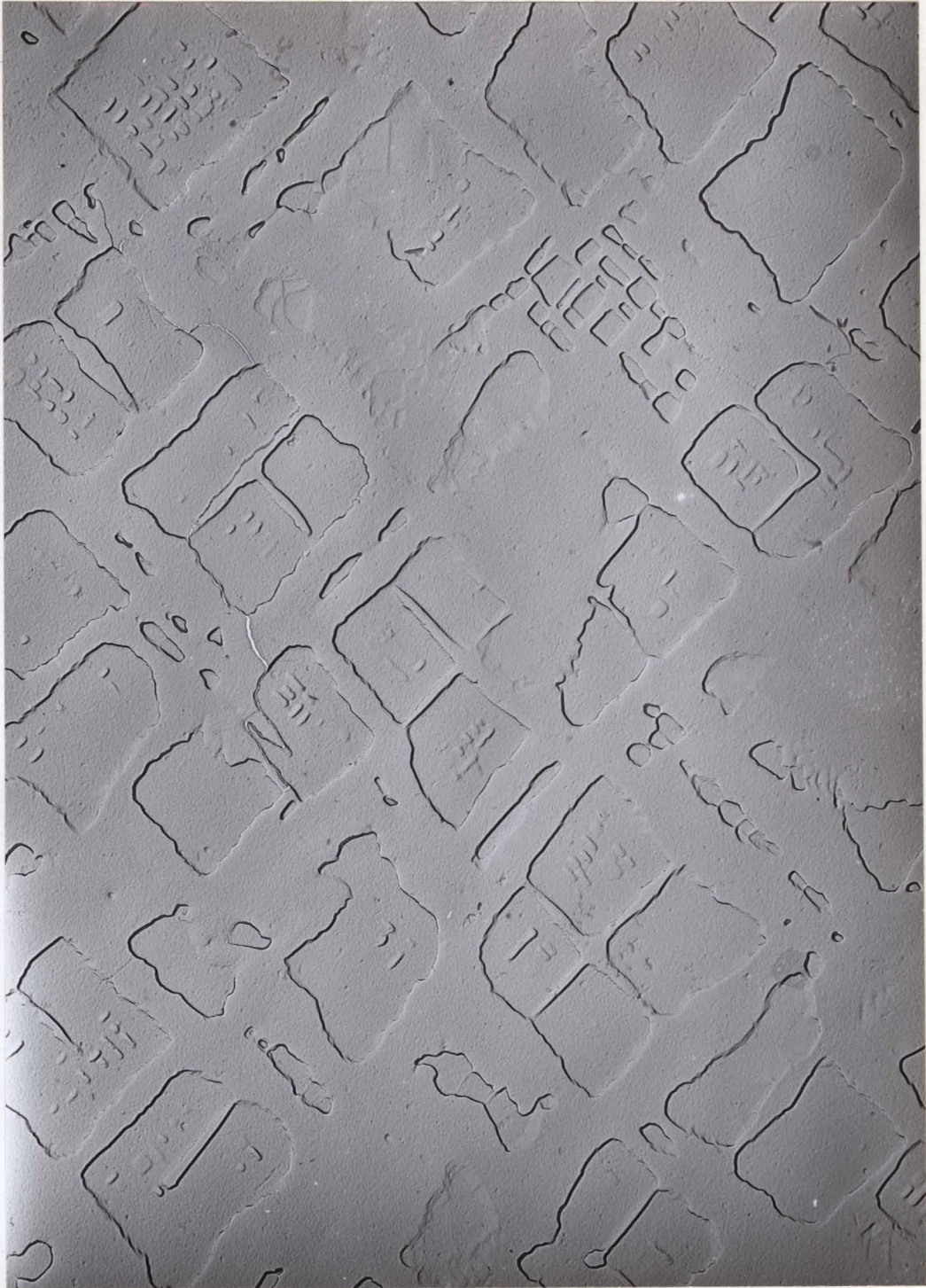


Fig. 45: Carbon replica of (100) section of 17<sup>a</sup>/o Al single crystal,  
slow cooled 1300 to 700<sup>o</sup>C in 3 hours and aged 4 weeks at 700<sup>o</sup>C.  
X25,000



Fig. 46: Transmission electron micrograph of (100) section from 17<sup>a</sup>/o Al single crystal slow cooled 1300 to 700<sup>o</sup>C in 3 hours and aged 4 weeks at 700<sup>o</sup>C. X20,000



Fig. 47: Optical micrograph of (100) section from 17<sup>a</sup>/o Al single crystal, step cooled 1300 to 700<sup>o</sup>C over 3 weeks. X750

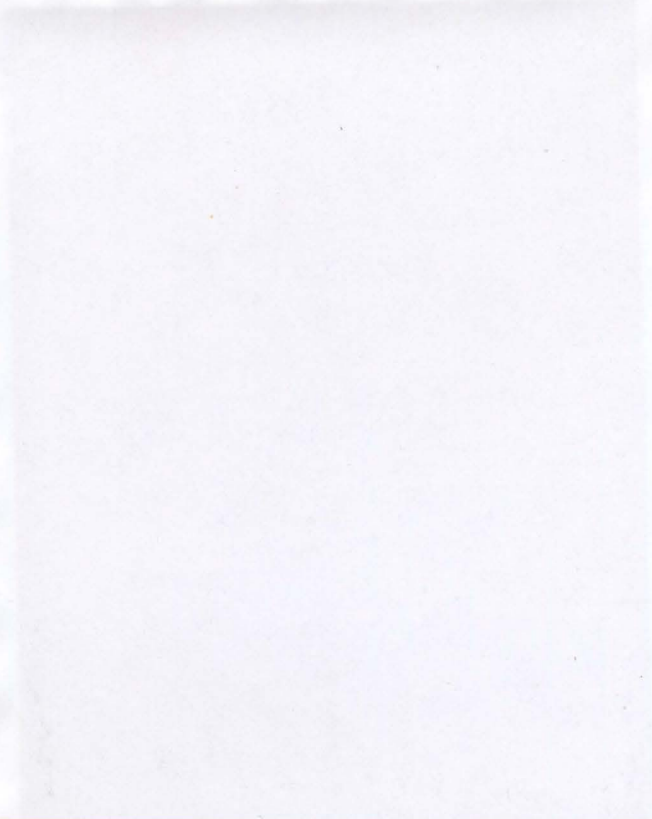
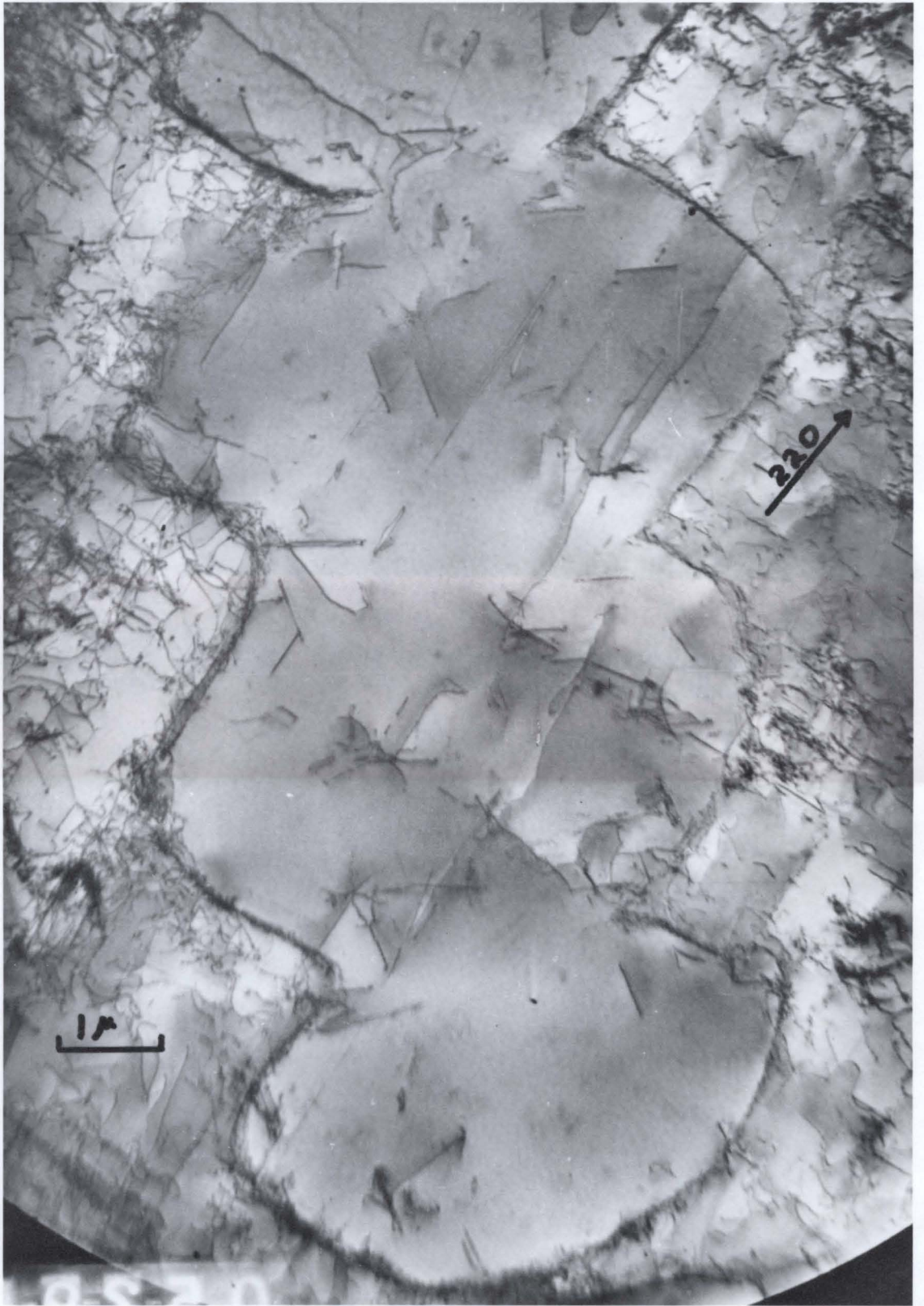


Fig. 48: Transmission electron micrograph of (100) section of 17<sup>a</sup>/o Al single crystal step cooled 1300 to 700°C over 3 weeks.



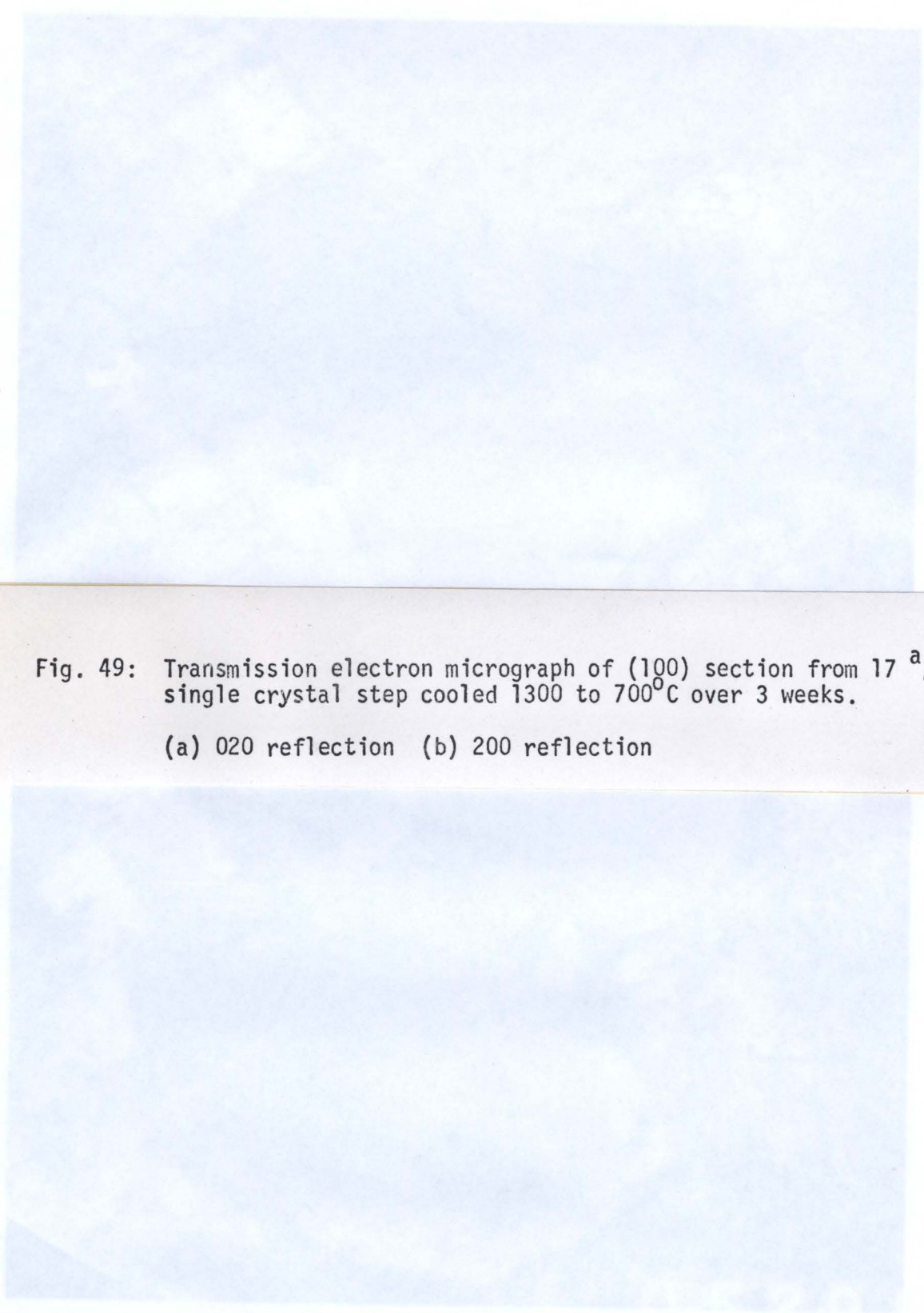
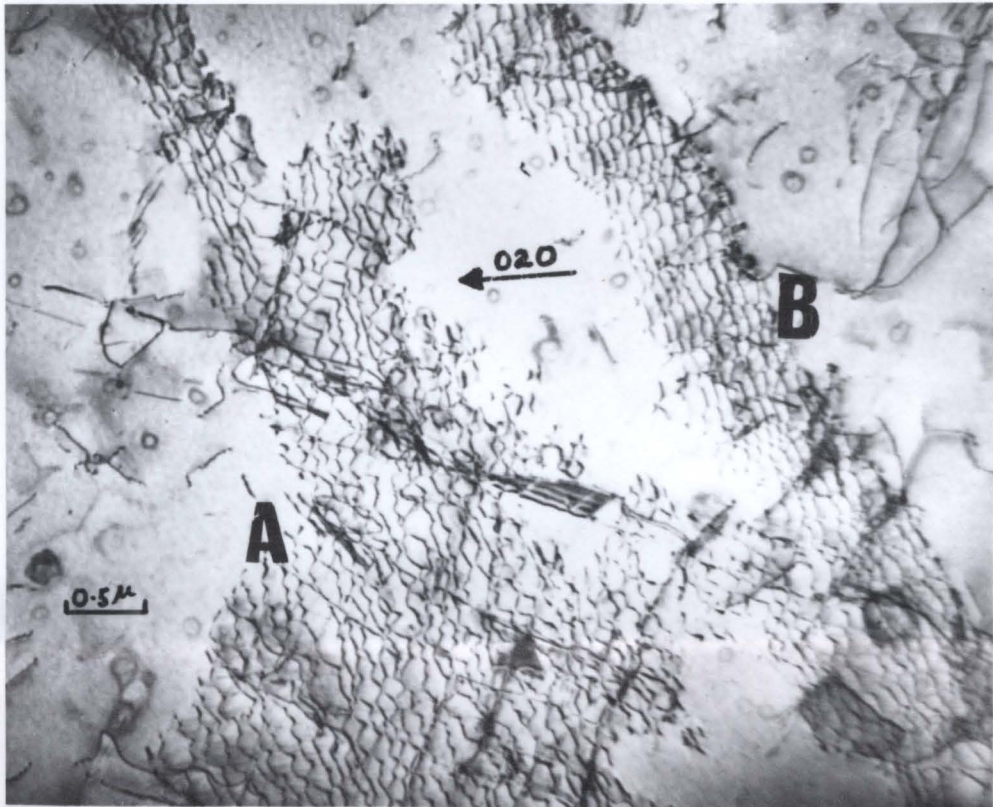
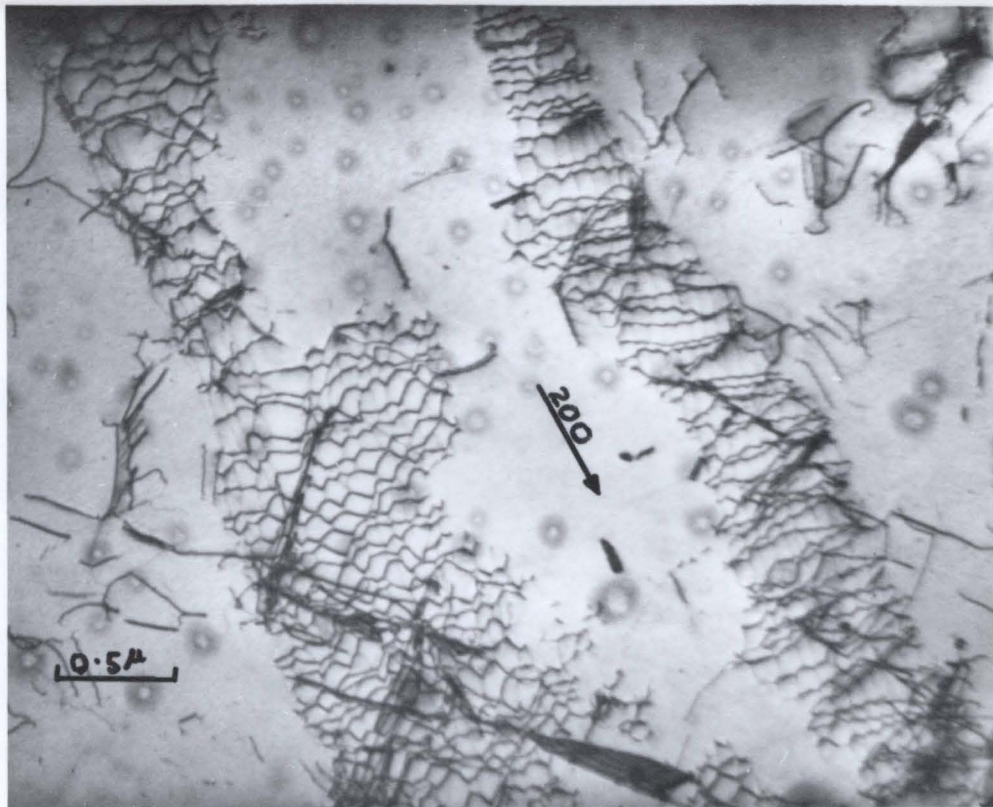


Fig. 49: Transmission electron micrograph of (100) section from 17<sup>a</sup>/o Al single crystal step cooled 1300 to 700°C over 3 weeks.

(a) 020 reflection (b) 200 reflection



(a)



(b)

(b)



Fig. 50: Transmission electron micrograph of (100) section from 17<sup>a</sup>/o Al single crystal step cooled 1300 to 700°C over 3 weeks.

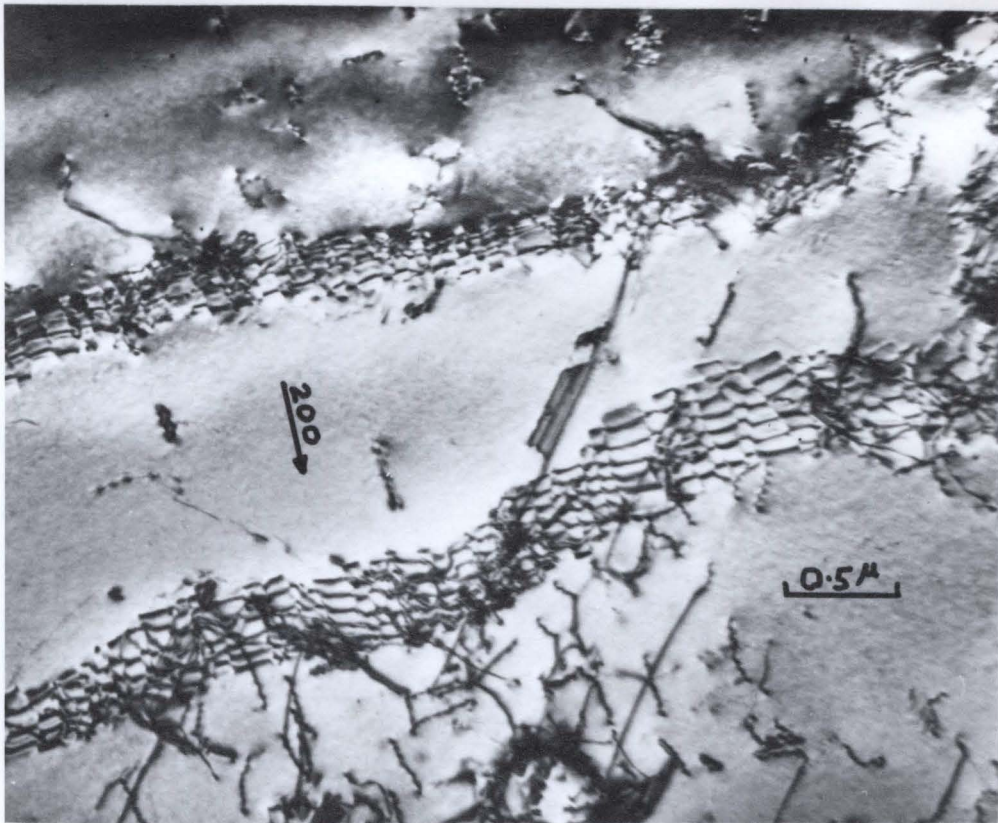
(a) 020 reflection (b) 200 reflection

(d)





(a)



(b)

(a)

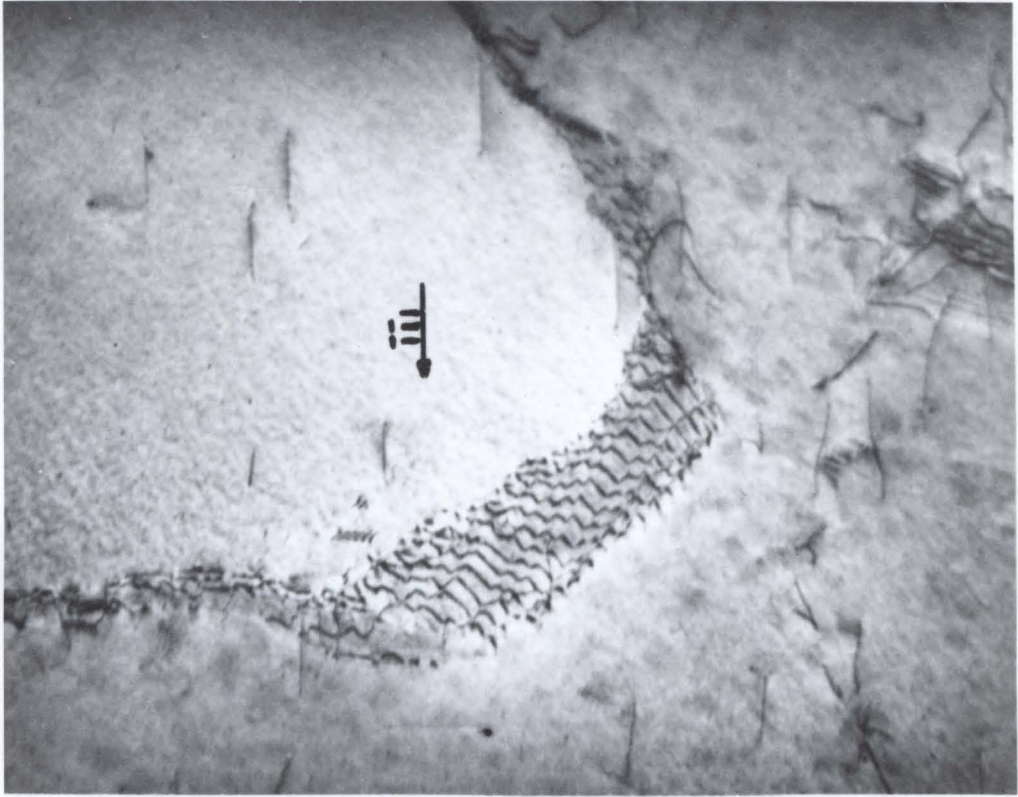


Fig. 51: Transmission electron micrograph of (112) section from 17<sup>a</sup>/o Al single crystal step cooled 1300<sup>o</sup> to 700<sup>o</sup>C over 3 weeks.

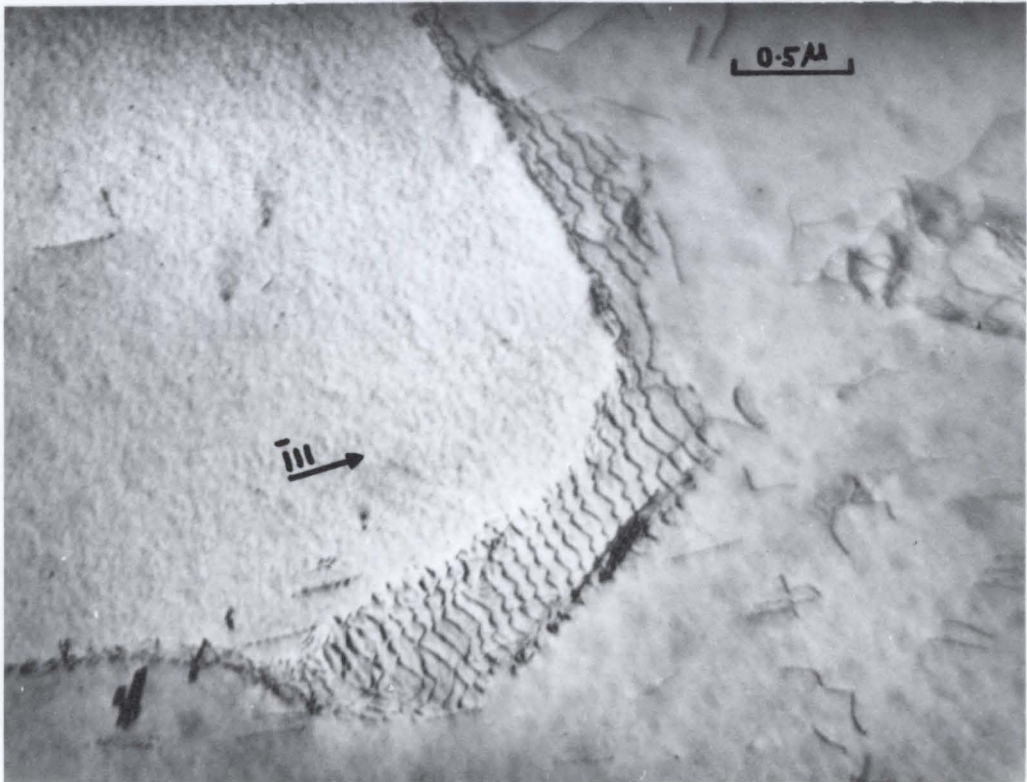
(a)  $\bar{1}\bar{1}1$  reflection (b)  $\bar{1}\bar{1}1$  reflection

(d)





(a)



(b)

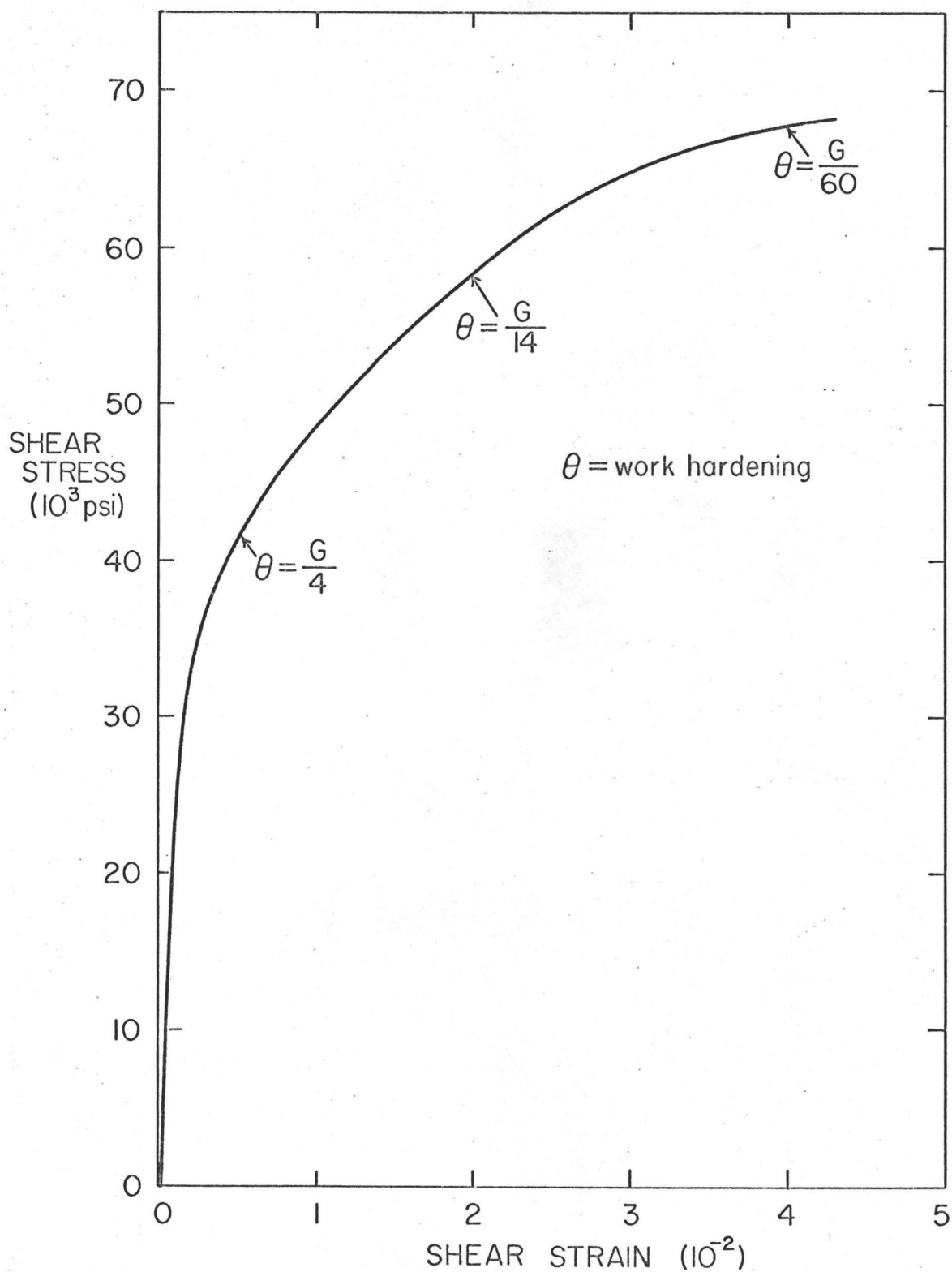


FIG. 52: Shear stress-shear strain for 18 % Al single crystal. Slow cooled  $1300^{\circ}-700^{\circ}\text{C}$ . in 3 hours.



Fig. 53: Optical micrograph of surface of 18<sup>a</sup>/o Al single crystal  
slow cooled 1300 to 700<sup>o</sup>C in 3 hours. X400



Fig. 54: Transmission electron micrograph of 18<sup>a</sup>/o Al single crystal slow cooled 1300 to 700<sup>o</sup>C in 3 hours. X32,000



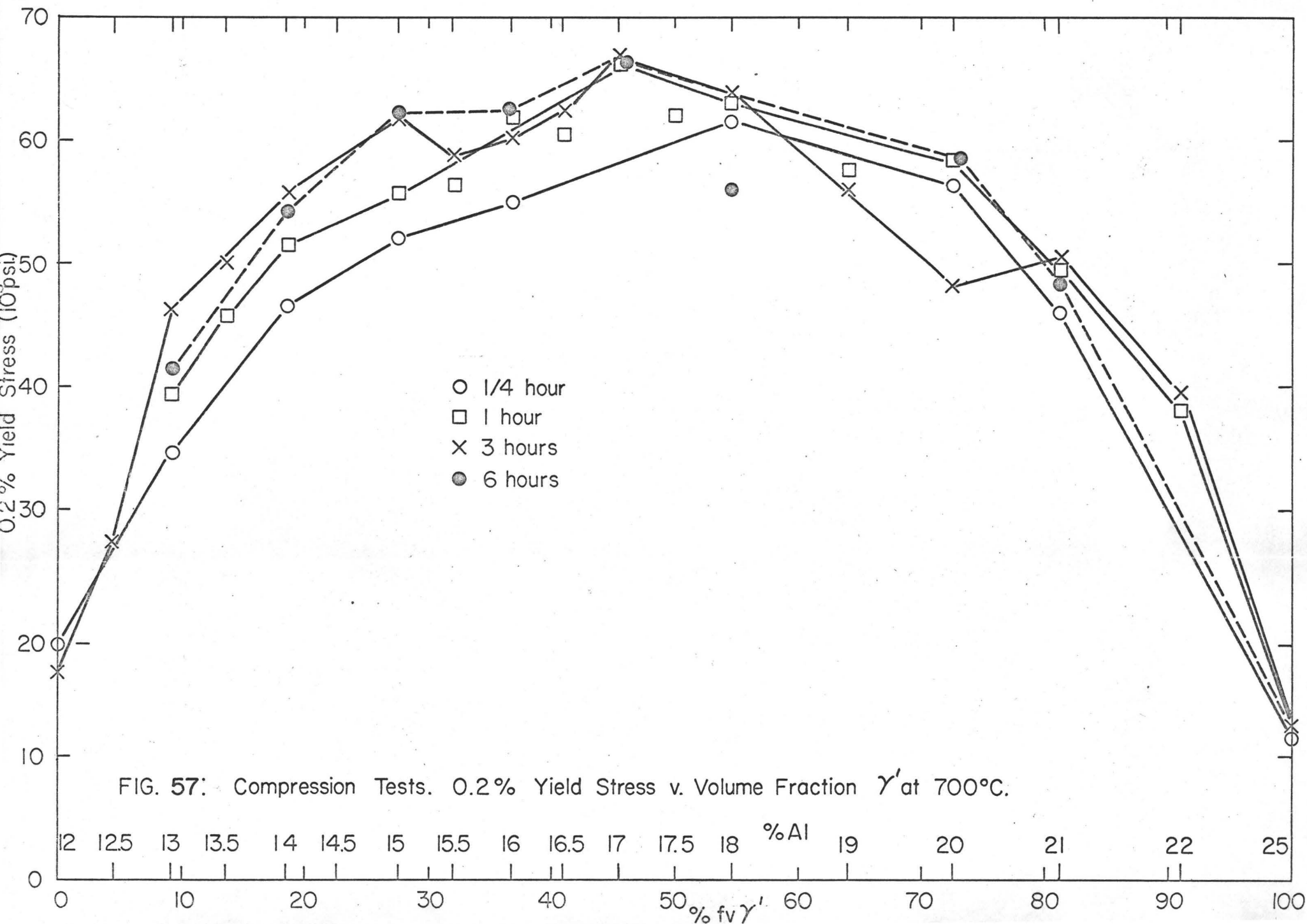
Fig. 55: Transmission electron micrograph of (100) section from  
17<sup>a</sup>/o Al single crystal step cooled 1300 to 700°C over  
3 weeks. X35,000

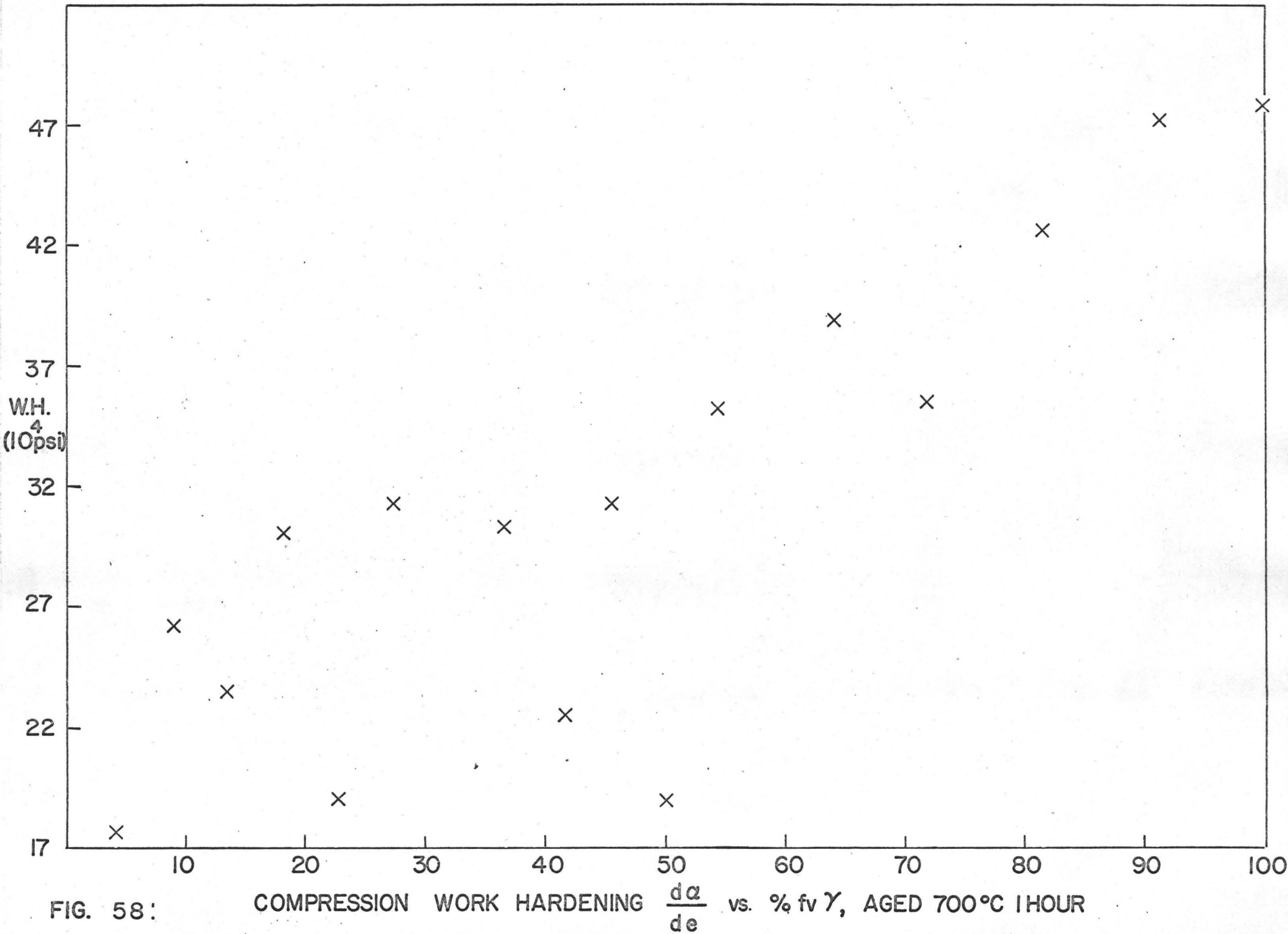
A - coherent particle

B - incoherent particle



Fig. 56: Transmission electron micrograph of 13<sup>a</sup>/o Al single crystal  
step cooled 1300 to 700<sup>o</sup>C over 3 weeks. X35,000





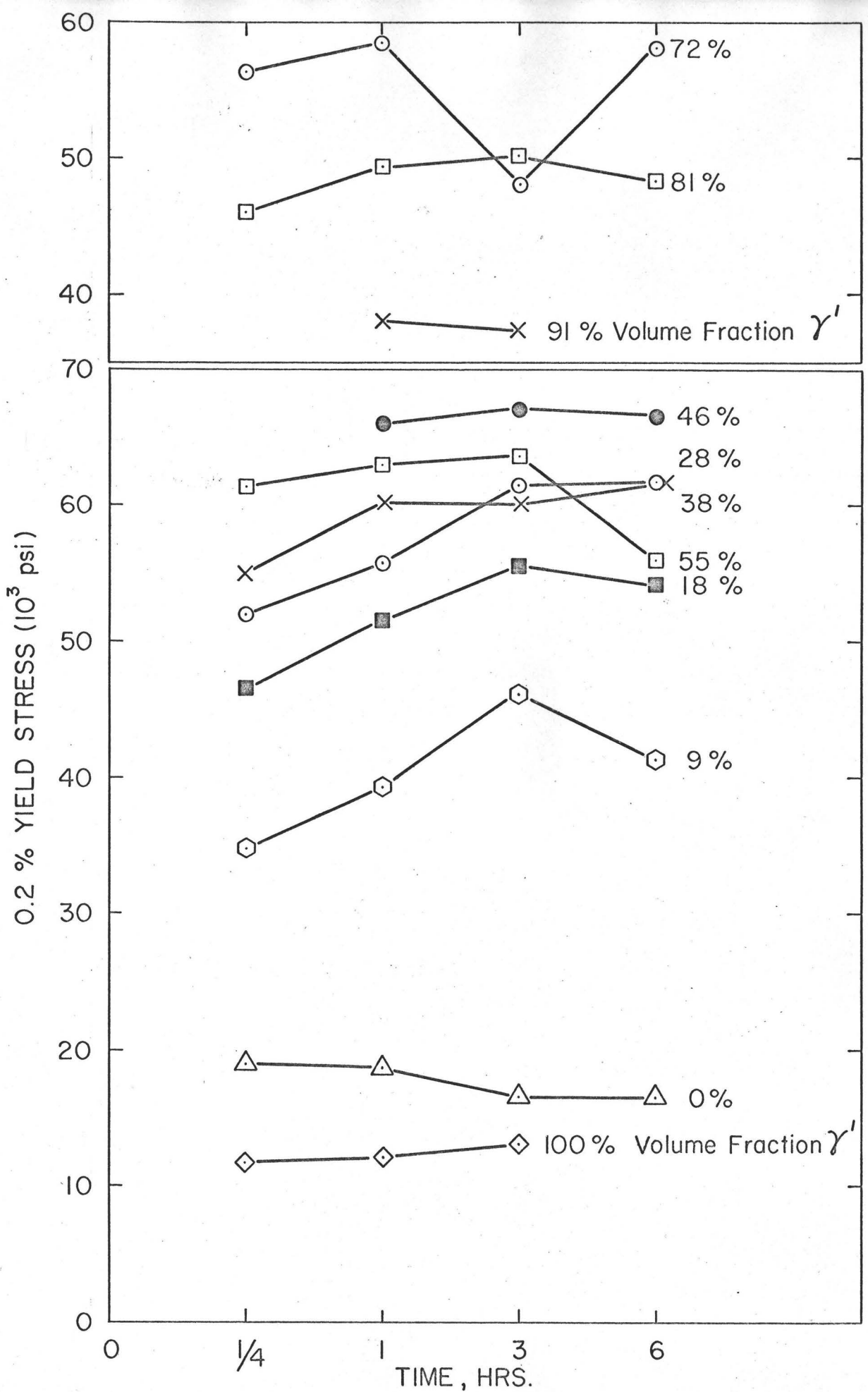


FIG. 59: Compression: Aging time at 700°C. vs. 0.2 % Yield Stress.

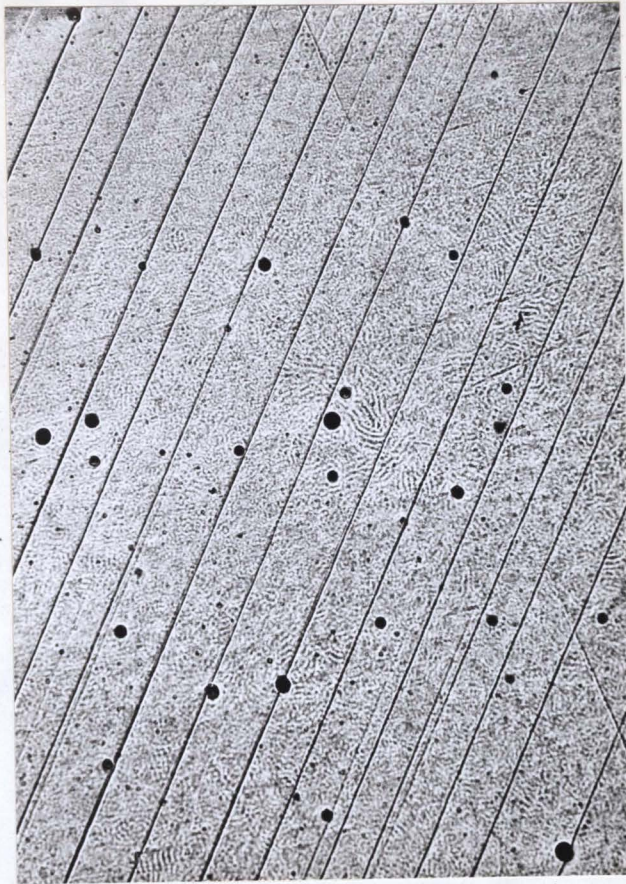


Fig. 60: Optical micrograph of 13<sup>a</sup>% Al polycrystalline alloy aged 700°C  $\frac{1}{4}$  hour compressed 1%. X160



Fig. 61: Optical micrograph of pure Ni<sub>3</sub>Al polycrystalline alloy compressed 1%. X288



Fig. 62: Optical micrograph of 11<sup>a</sup>/o Al polycrystalline alloy  
compressed 1.3%.

X1000

Fine slip lines

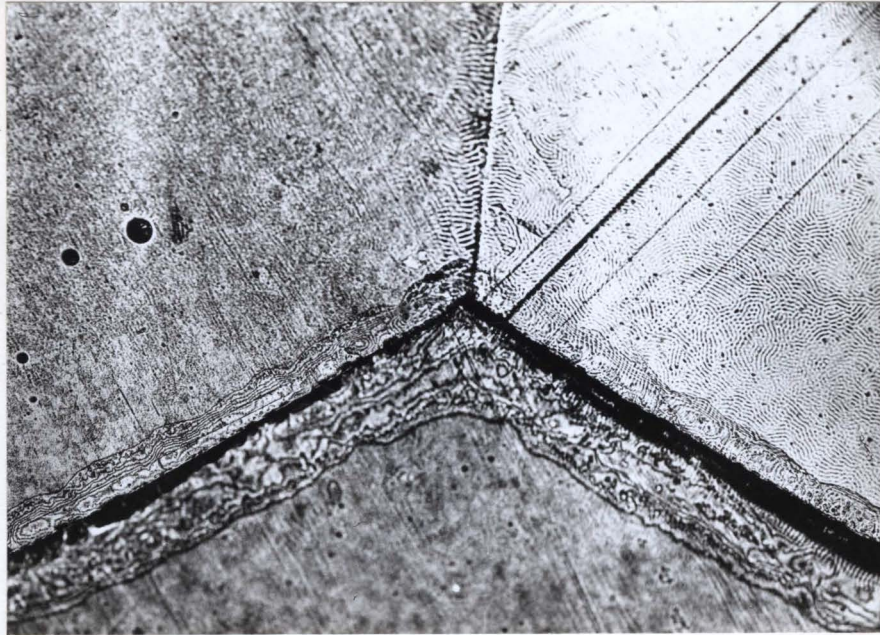


Fig. 63: Optical micrograph of 19<sup>a</sup>% Al polycrystalline alloy aged 700<sup>o</sup>C ¼ hour, compressed 1%. X160  
Grain boundary cracking



Fig. 64: Optical micrograph of 14<sup>a</sup>% Al polycrystalline alloy aged 700<sup>o</sup>C ¼ hour, compressed 1%. Deformation in grain boundary regions. X160

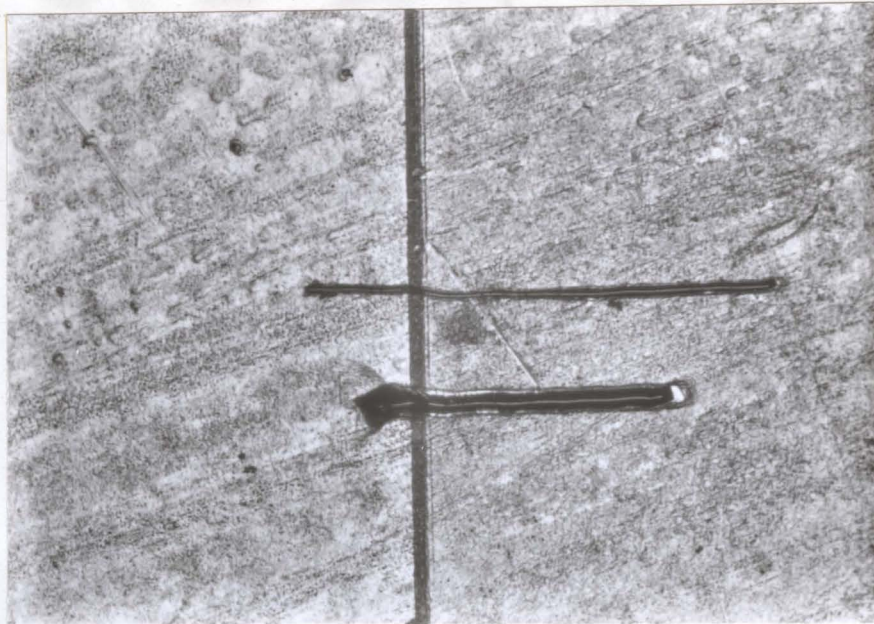


Fig. 65: Optical micrograph of 17<sup>a</sup>/o Al bicrystal aged 700<sup>o</sup>C 6 hours.  
Compressed 2%. Grain boundary sliding X23

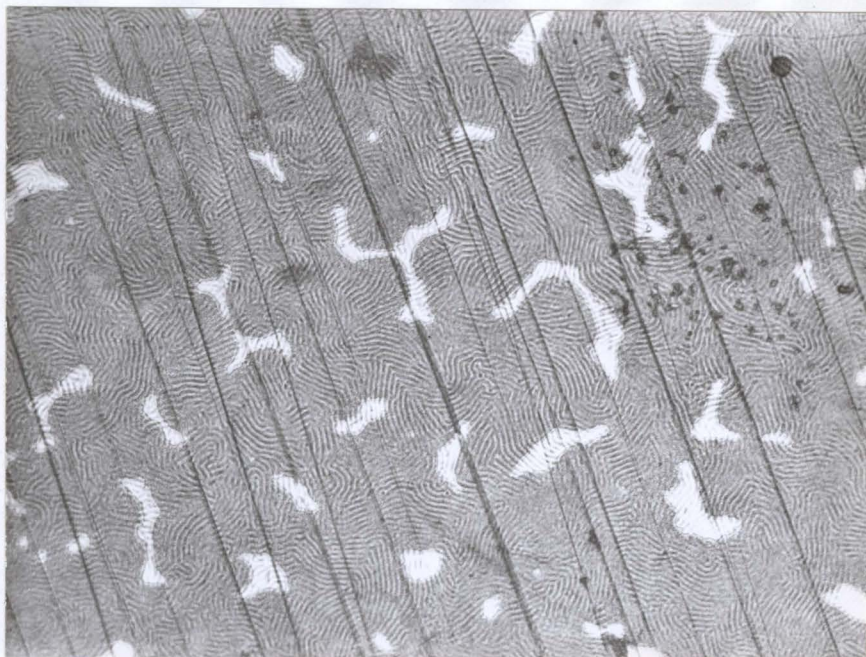


Fig. 66: Optical micrograph of 21<sup>a</sup>/o polycrystalline alloy aged 700<sup>o</sup>C  
 $\frac{1}{4}$  hour compressed 1.5%. X160

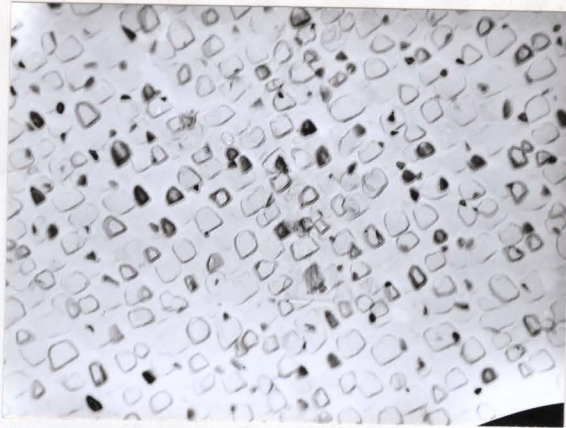


Fig. 67: Electron micrograph carbon replica of surface of 17<sup>a</sup>/o Al polycrystalline alloy aged 700<sup>o</sup>C 1 hour. X26,000

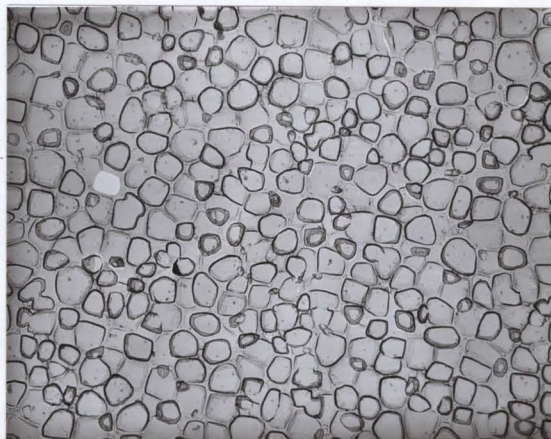


Fig. 68: Electron micrograph carbon replica of surface of 20<sup>a</sup>/o Al polycrystalline alloy aged 700<sup>o</sup>C 1 hour. X8000

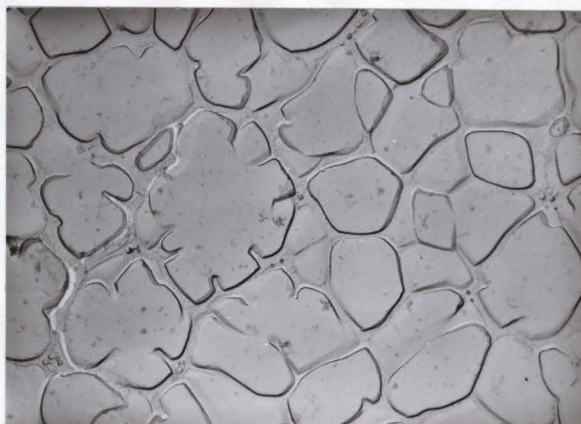


Fig. 69: Electron micrograph of carbon replica from surface of 21<sup>a</sup>/o Al polycrystalline alloy aged 700<sup>o</sup>C for 1 hour. X8000

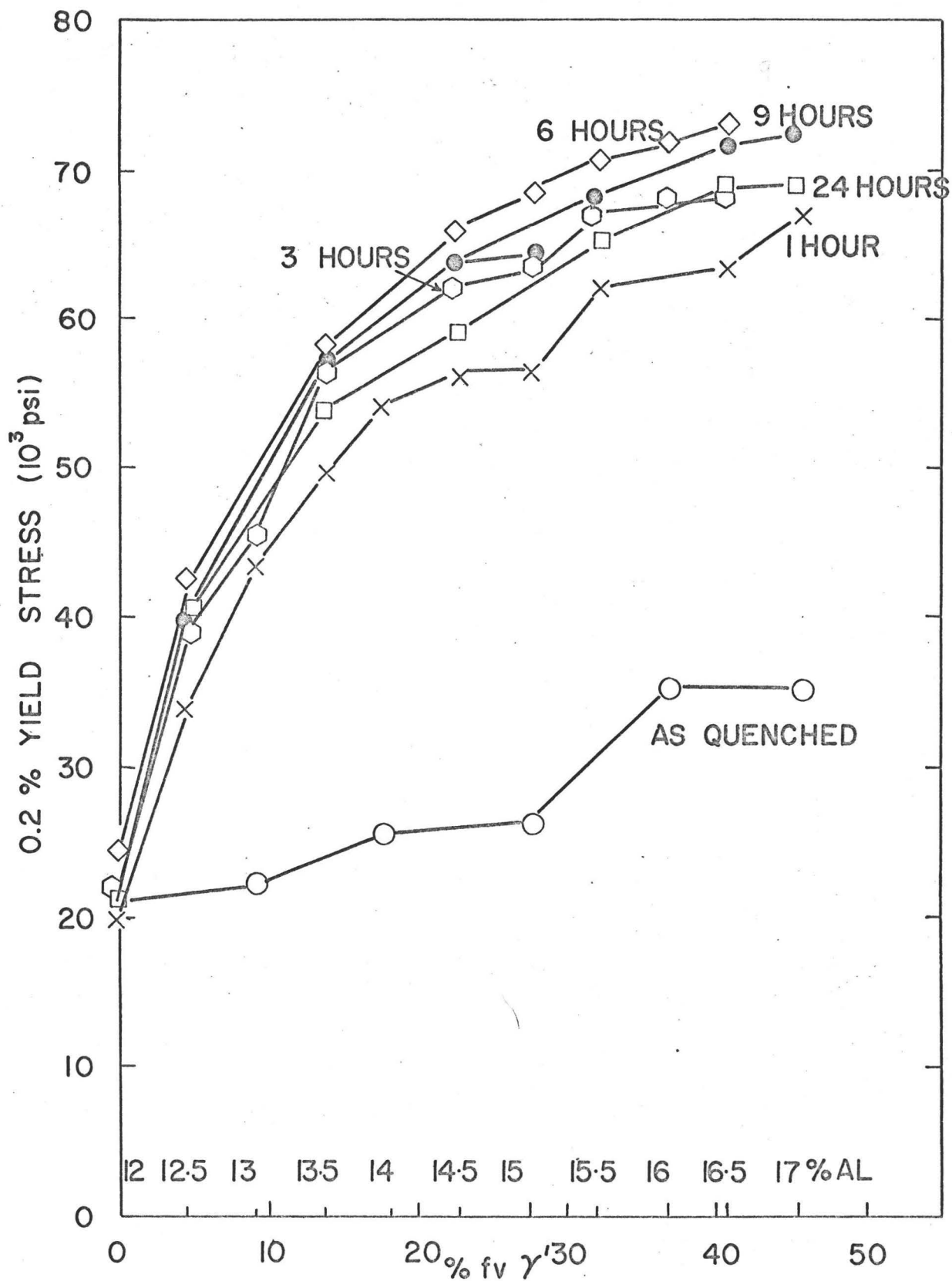


FIG. 70: TENSILE : VOLUME FRACTION  $\gamma'$  vs. 0.2% YIELD STRENGTH AGED 700°C

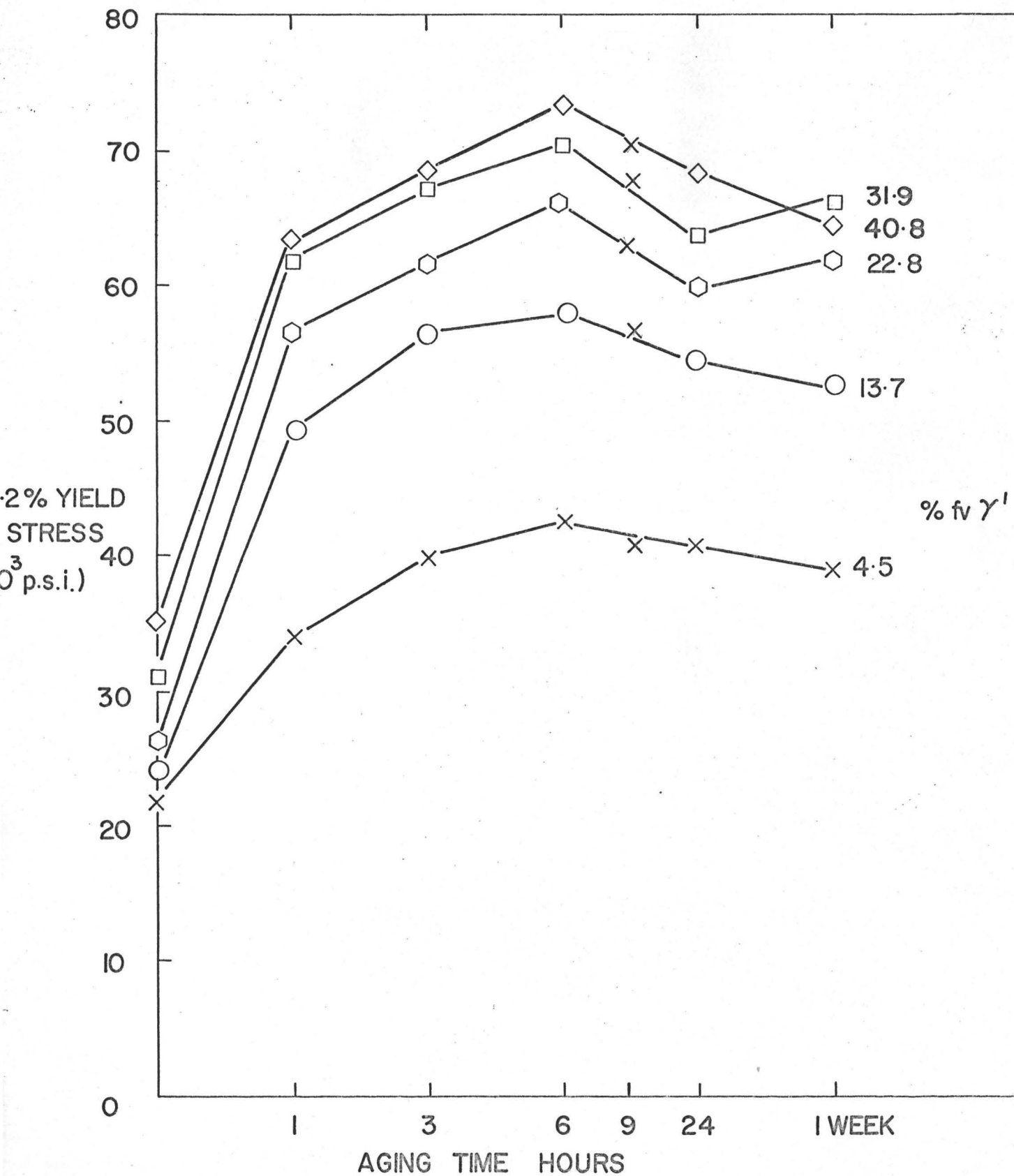


FIG. 71: TENSILE: AGING TIME AT 700°C vs. 0.2% YIELD STRESS

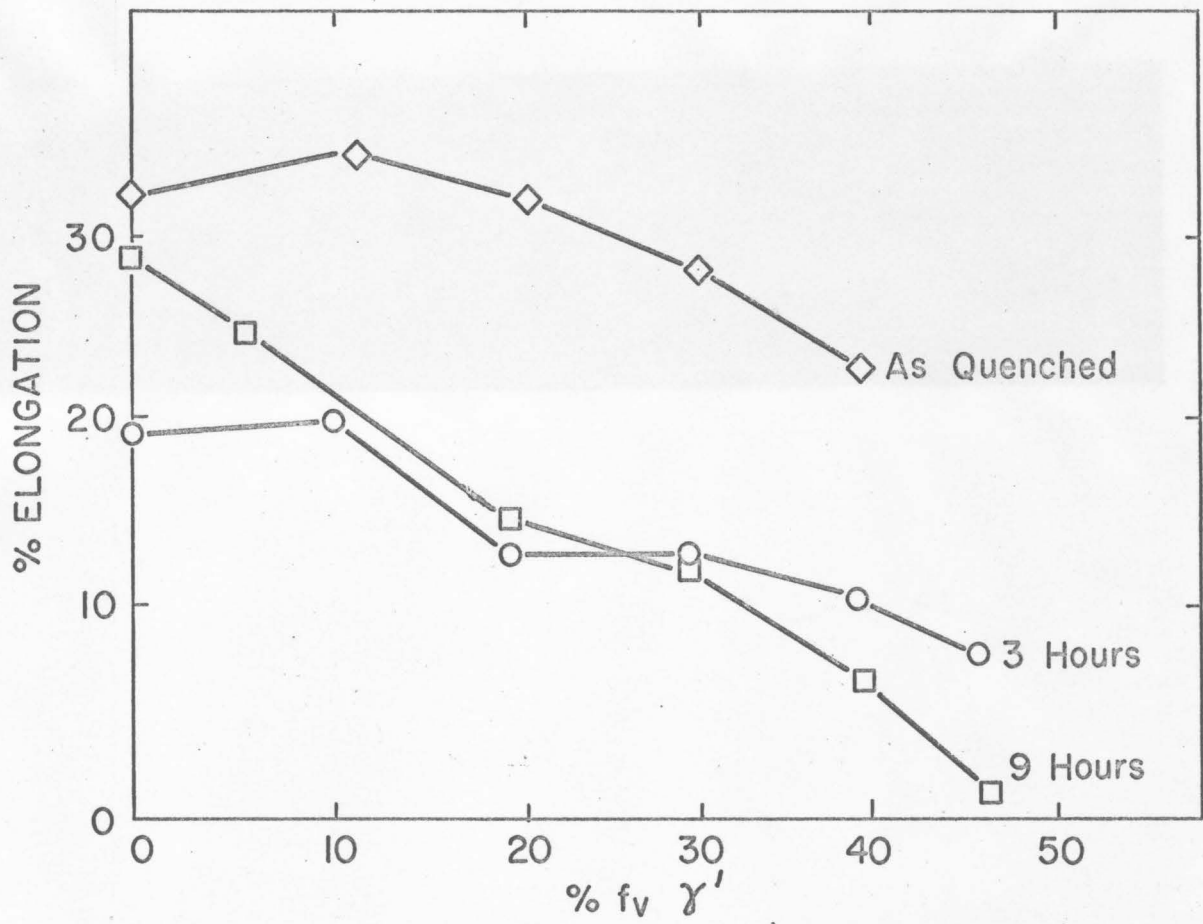


FIG. 72: Tensile elongation vs. %  $f_v \gamma'$ , aged 700°C.

Fig. 73: Transmission electron micrograph of 16<sup>a</sup>/o Al polycrystalline alloy. Dark field from superlattice line.

(a) Aged 700<sup>o</sup>C 1 week X50,000

(b) Aged 700<sup>o</sup>C 3 weeks X26,000

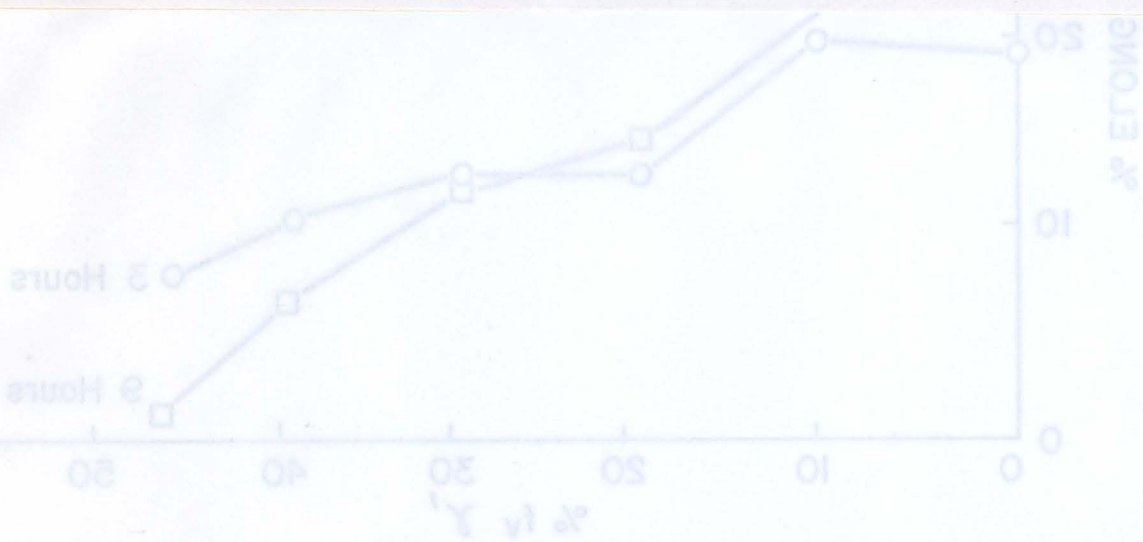
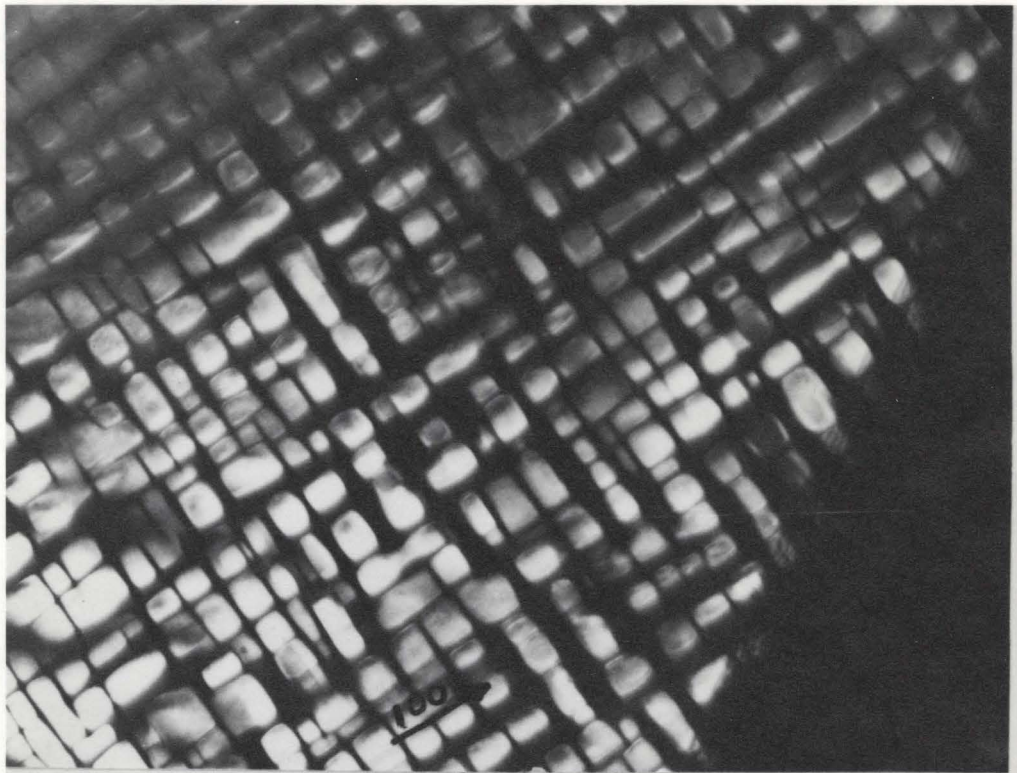
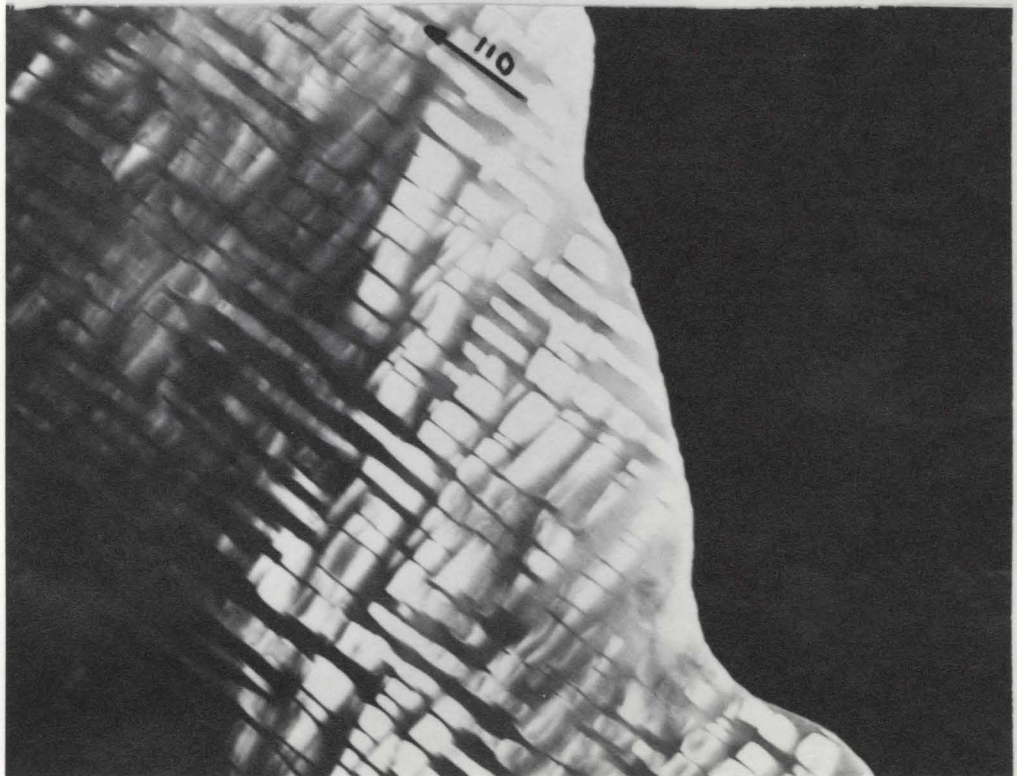


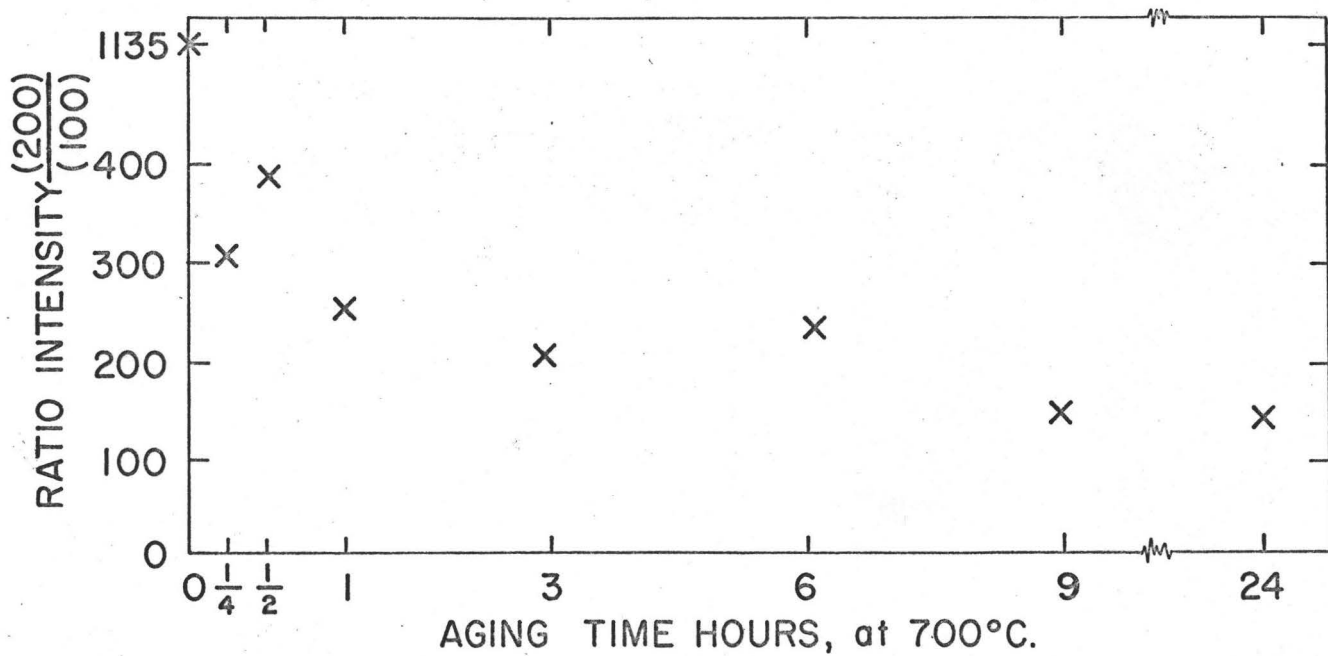
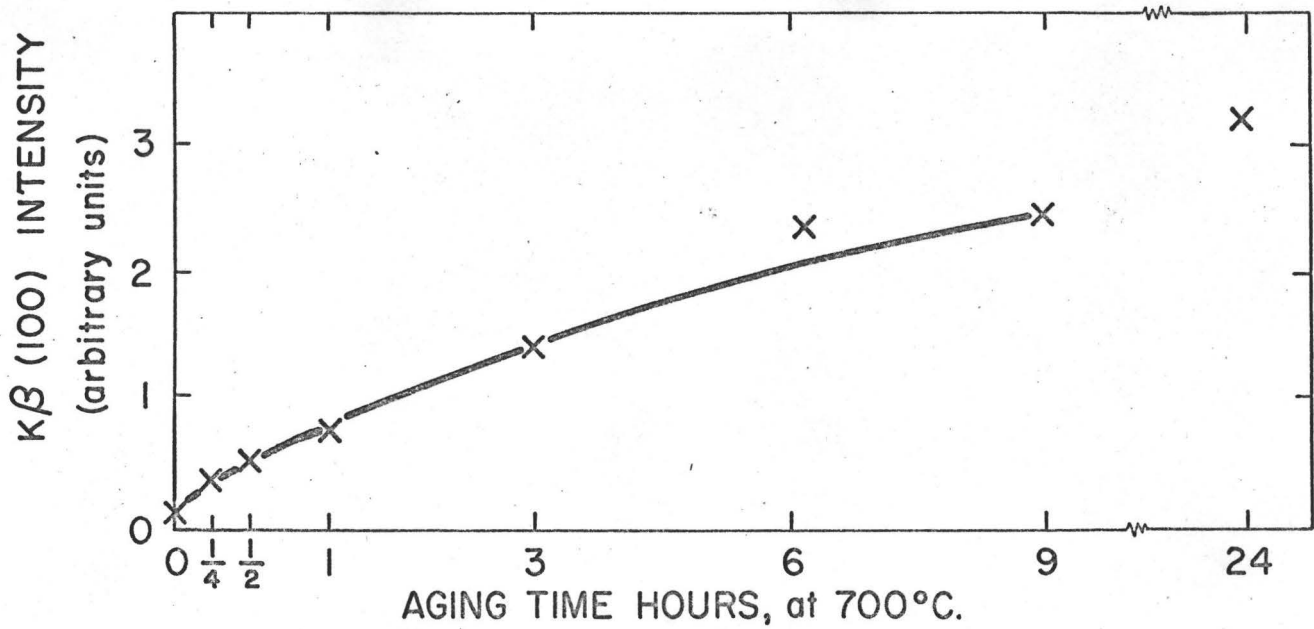
FIG. 72: Tensile elongation vs. aging time at 700°C.



(a)



(b)



$\frac{1}{2}$  PEAK WIDTH  $^{\circ}\theta$

Aging time hours	0	$\frac{1}{4}$	$\frac{1}{2}$	1	3	6	9	24
100	.5	.37	.3	.27	.2	.19	.17	.15
200	.06	.05	.044	.06	.075	.175	.125	.16

FIG. 74: Long range order measurements on (100) section from 16 % Al single crystal.

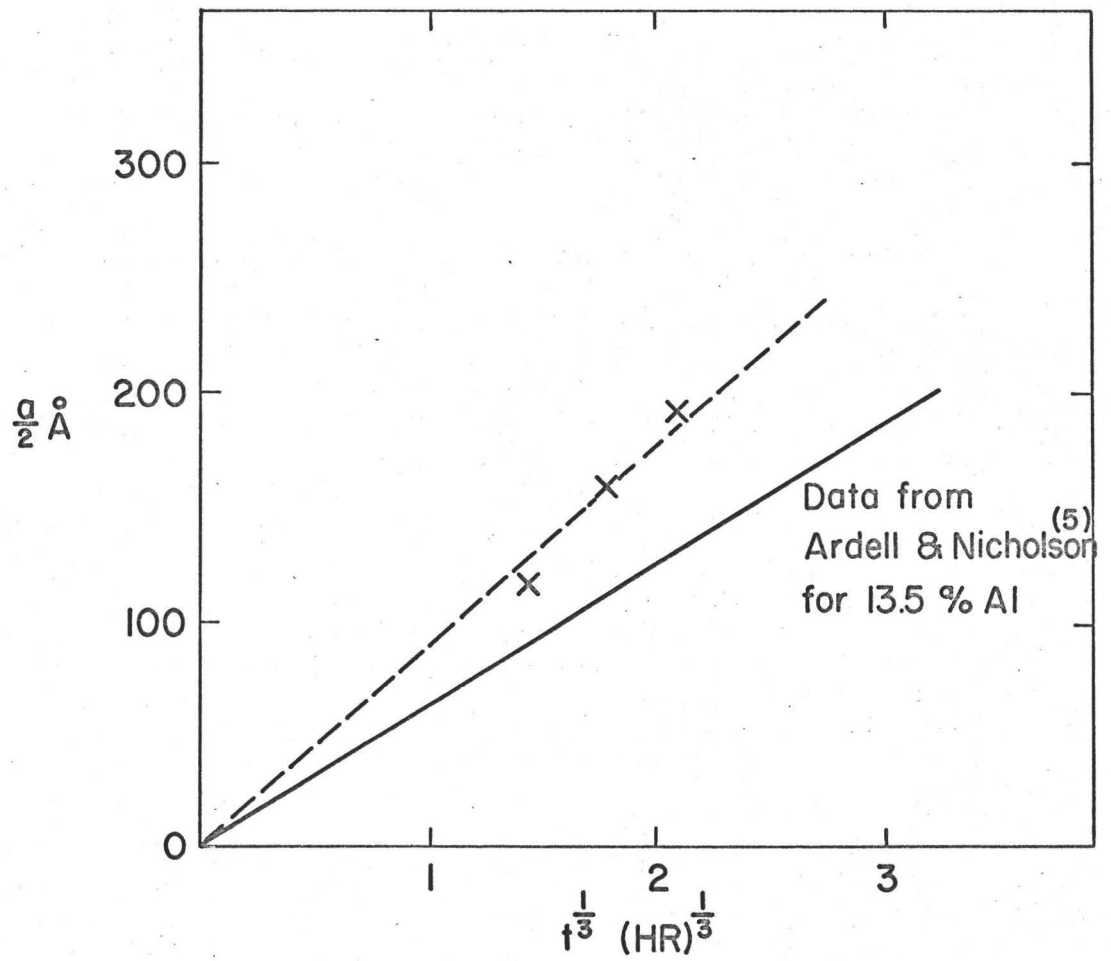
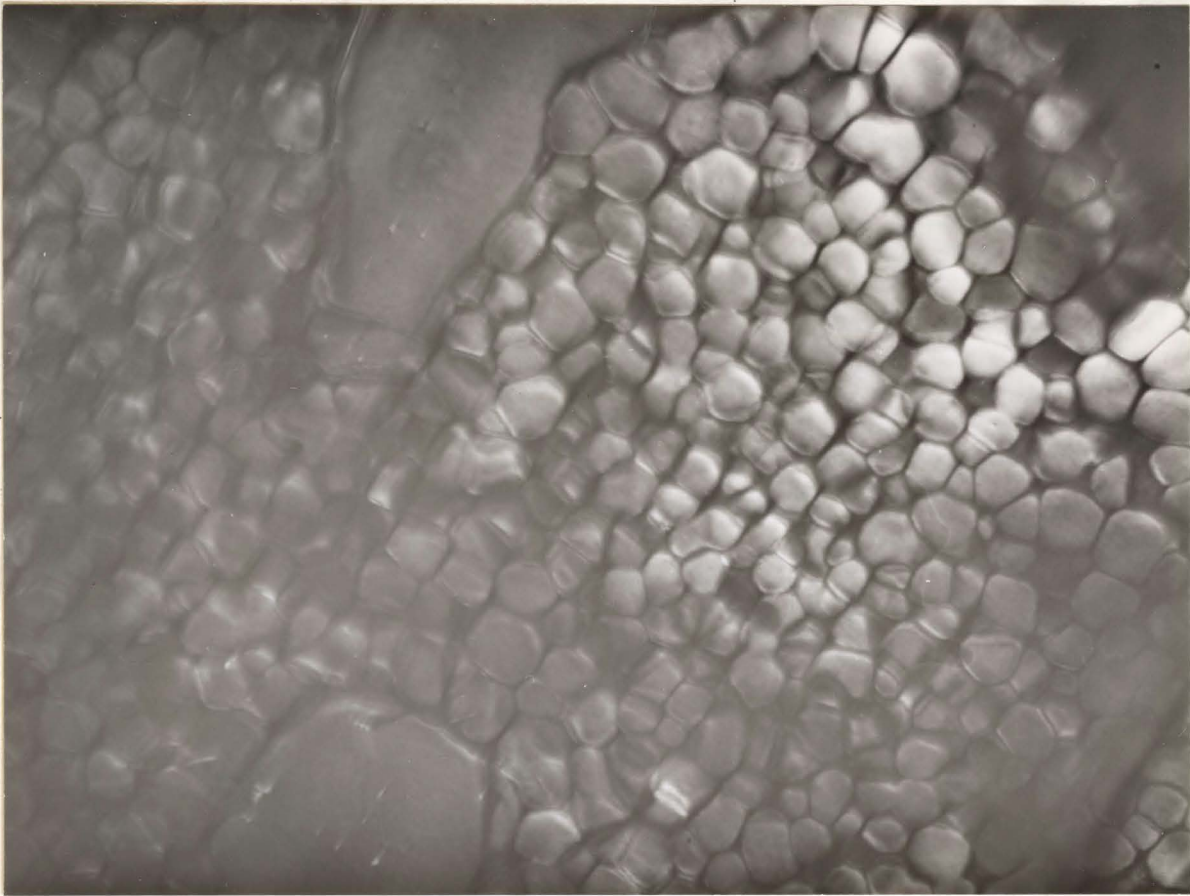
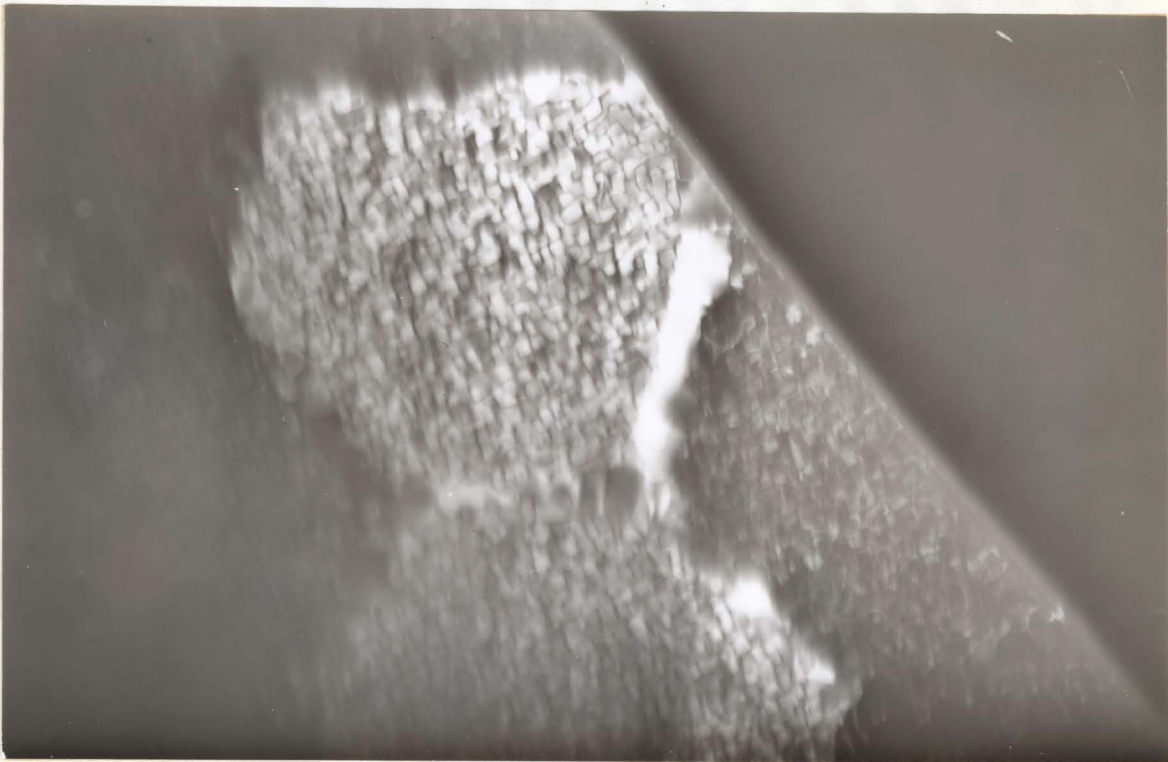


FIG. 75:  $\gamma'$  particle sizes for 16.5 % aged at 700°C.



(a)



(b)

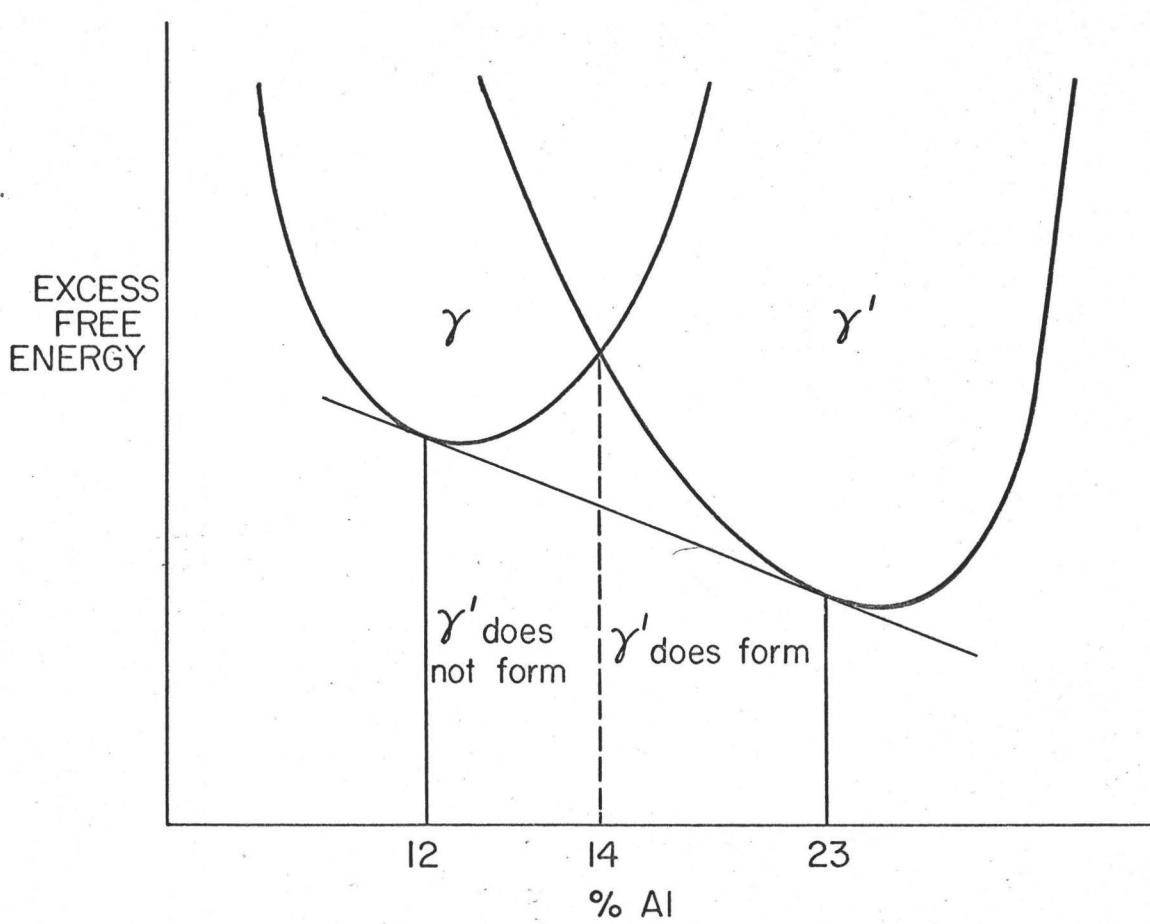
Fig. 76: Transmission electron micrographs of 21% Al alloy sputter cooled. Dark field superlattice reflection.

(a) Sputter cooled X55000

(b) Sputter cooled and aged 700°C 3 hours X35000



Fig. 77: Electron micrograph of 16<sup>a</sup>/o Al water quenched. X40,000



8  
 FIG. 78: Free energy versus composition diagram for Ni-Al alloys showing compositions where  $\gamma'$  forms on quenching (schematic).

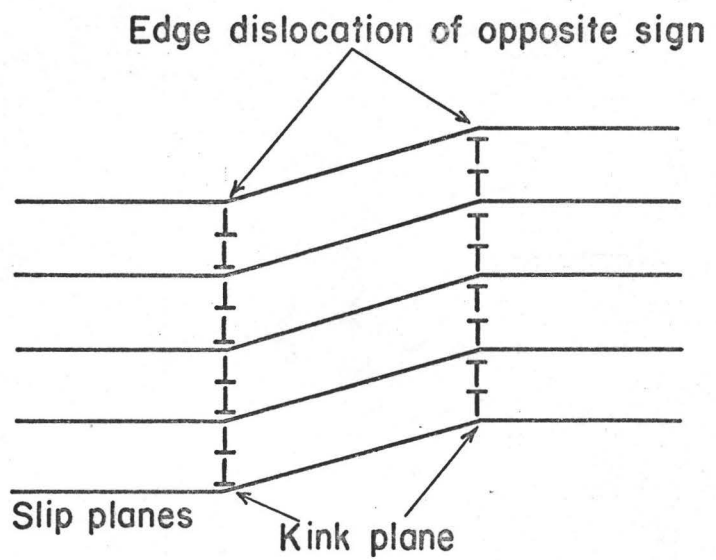


FIG. 79: Dislocation structure of Kink bands.

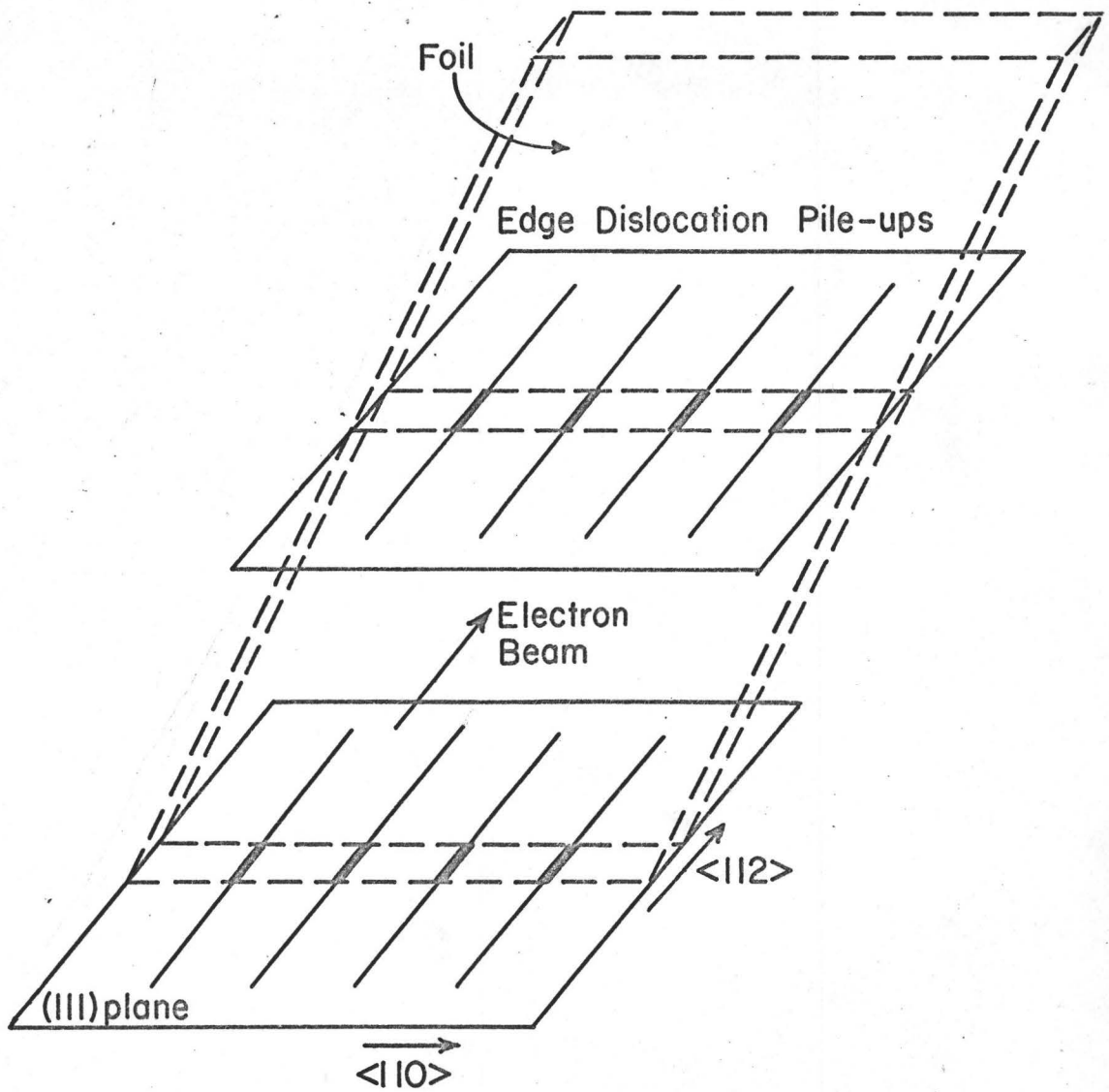
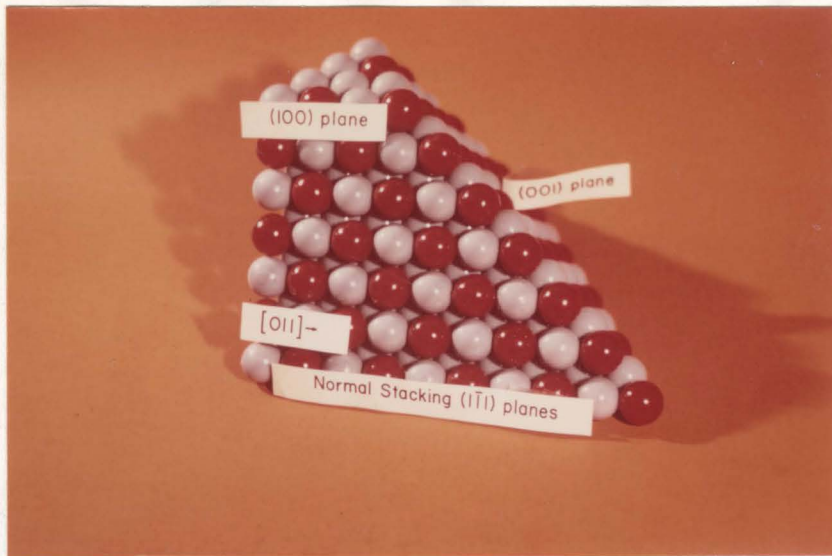
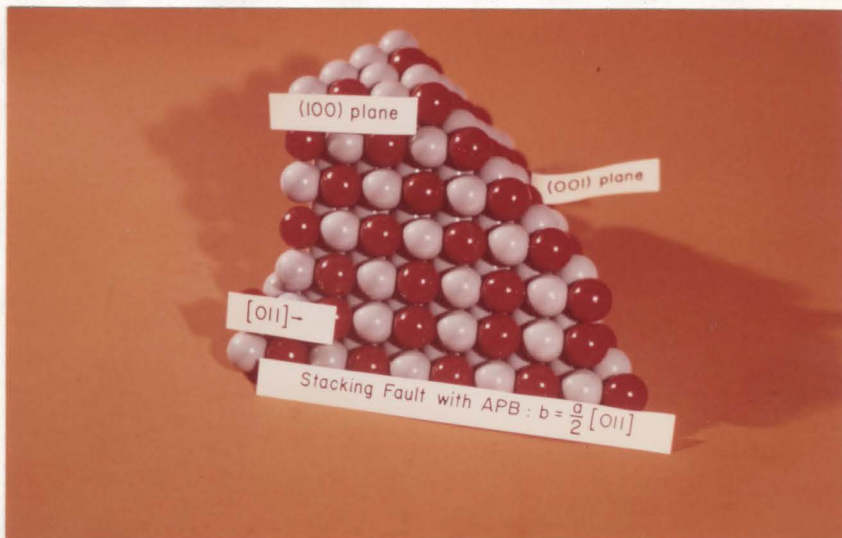


FIG. 80: Model of Kink band structure explaining electron micrographs (FIG. 16).

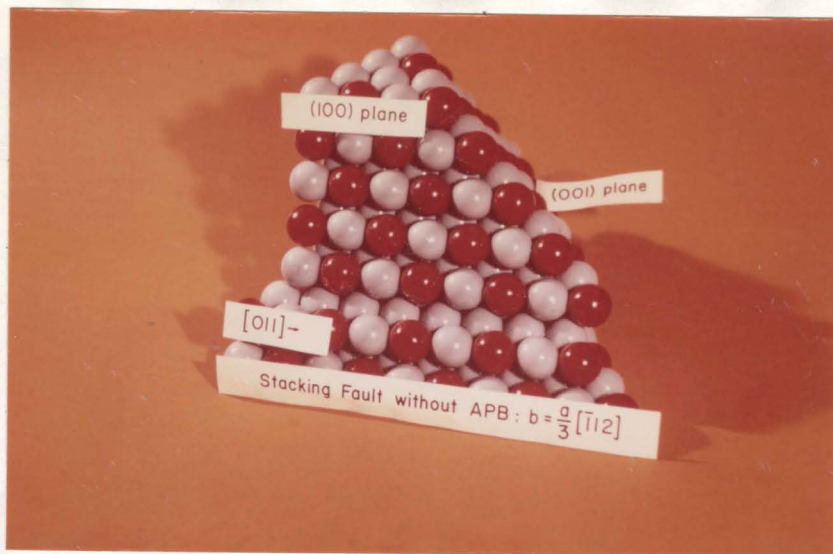


(a)

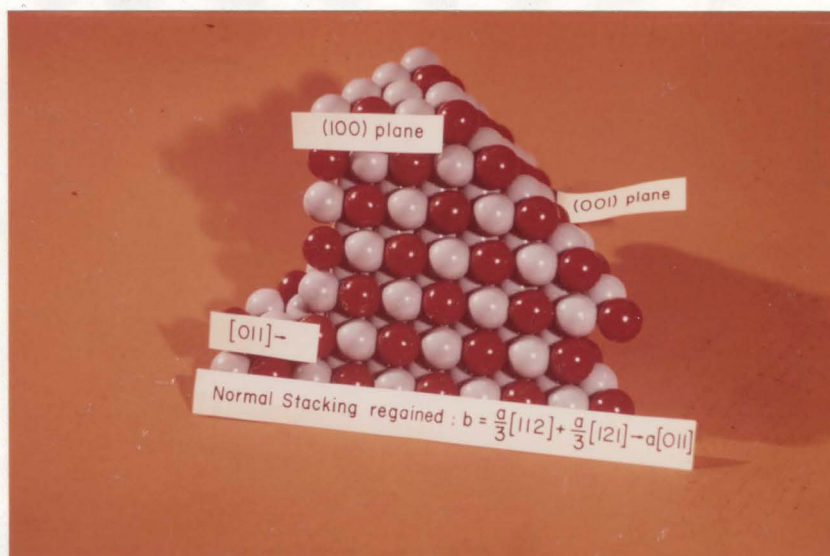


(b)

Fig. 81: Ball model to illustrate formation of stacking faults in  $\text{Ni}_3\text{Al}$  without APB. Red-aluminum, blue-nickel.



(a)



(b)

Fig. 82: Ball model to illustrate formation of stacking faults in  $\text{Ni}_3\text{Al}$  without APB. Red-aluminum, blue-nickel.

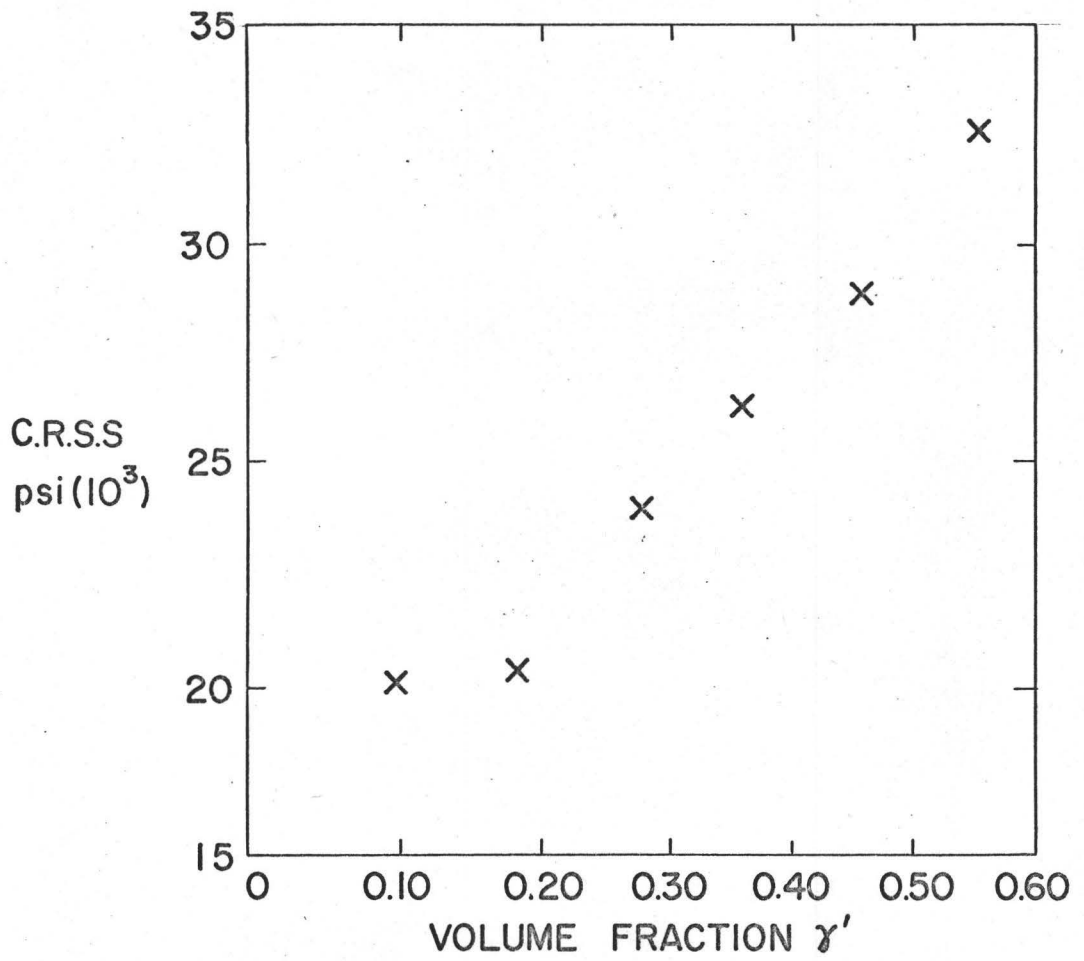


FIG. 83: C.R.S.S. for single crystals aged 700°C, 6 hours vs. volume fraction  $\gamma'$ .